

Discrete modeling of capillary ring structures during drying of particle aggregates

Dissertation

zur Erlangung des akademischen Grades

Doktoringenieur

Dr.-Ing.

von **MSc. Hafiz Tariq Mahmood**

geb. am 25.04.1988 in Bhakkar, Pakistan

genehmigt durch die Fakultät für Verfahrens- und Systemtechnik
der Otto-von-Guericke-Universität Magdeburg

Promotionskommission: Prof. Gabor Janiga (Vorsitz)
PD Dr. Ing. habil. Abdolreza Kharaghani (Gutachter)
Prof. Dr. Ing. habil. Evangelos Tsotsas (Gutachter)
Prof. Andrew Bayly (Gutachter)

eingereicht am: April 01, 2022

Promotionskolloquium am: June 21, 2022

Declaration

I hereby declare that the dissertation with the title:

Discrete modeling of capillary ring structures during drying of particle aggregates

was prepared without inadmissible assistance and without the use of any aids other than those indicated. Facts or ideas taken from other sources, either directly or indirectly have been marked as such. In particular, I did not use the services of a commercial graduation consultation. Further I have not made payments to third parties either directly or indirectly for any work connected with the contents of the submitted dissertation.

The work has not been submitted as a dissertation either in Germany or abroad in the same or similar form and has also not been published as a whole.

Magdeburg, April 01, 2022

MSc. Hafiz Tariq Mahmood

Abstract

Despite the useful insights gained from previous experimental and theoretical investigations, quantitative characterization of pore-scale liquid continuity dynamics during evaporation from capillary porous media is uncommon due to observational limitations posed by pore space complexity. The motivation of this thesis is to resolve details of liquid flow and phase distribution during drying of capillary porous media and to assess the role of capillary films in supplying evaporative liquid. Experimental and numerical pore network simulation studies on convective drying of capillary porous media under slow isothermal conditions are presented in this thesis.

As a physical model of a real capillary porous medium, two dense packings of particles filled with monodisperse spherical glass beads (mean diameter 0.8 mm) and initially saturated either with distilled water or with a salt solution are prepared. Two controlled drying experiments with these packings are carried out using a custom-made setup installed in a lab-scale X-ray microtomograph. Based on in-situ tomograms (voxel size 16.4 μm) the time evolution of three-dimensional (3D) structures of liquid and salt deposit in the packings during drying are characterized. The respective results clearly demonstrate the formation of capillary liquid rings at the wedge-shaped pores located near the particle-particle contacts. The rings remain connected over a long distance to the packing surface during a significant period of drying.

In addition to the experiments, a 3D discrete pore network model in the limiting condition of capillary dominated regime that explicitly accounts for the ring effect is developed. The regular 3D ring pore network approximates the void space in a bed cubically packed with a population of monodisperse spherical particles. The interstitial void space between particles is approximated by cylindrical throats. The concave cylinder-shaped ring approximates the void space around the contact point of two adjacent particles. Primary and secondary capillaries are referred to as throats and rings, respectively. The hydraulic connectivity in a liquid phase is defined over both primary and secondary capillary structures together.

Pore network simulations in the presence and absence of this effect are compared with measurements in terms of drying kinetics and saturation profiles. The pore network simulations performed with capillary rings show a noticeable delay in transition from the capillary-supported regime to the diffusion-controlled regime. These simulation results differ significantly from the predictions of classical pore network models without liquid films and they appear to be more consistent with the experiments conducted with real porous systems. It is found that liquid rings act as additional hydraulic pathways for moisture transport from the interior of the pore/particle network to the surface and thus notably accelerate the drying process, and they lead to a spatially homogeneous distribution of the liquid down to low saturation. The developed ring pore network model is also used to examine the influence of variation of the size of throats and rings, the throat radius distribution and the boundary layer thickness on the drying kinetics in a systematic way.

Moreover, the mass transfer between the surface of a model capillary porous medium and the adjacent gas-side boundary layer is studied. In order to quantify the role and significance of liquid films in the mass transfer process, three-dimensional pore network Monte Carlo simulations are carried out systematically in the presence and absence of discrete capillary rings. As compared to classical pore network models, the pore network model with rings seem to predict favorably the spatiotemporal evolution of wet and dry

patches at the medium surface as well as of their relative contributions to the net mass exchange rate. This is apparent when the analytical solutions of the commonly used Schlünder's model are examined against the numerical simulations conducted using classical and ring pore network models. This study can be considered as a step forward in discrete modeling of drying of capillary porous media with 3D secondary capillary structures and should be of interest for various applications in the field of complex multiphase flow phenomena in porous media.

Kurzzusammenfassung

Trotz der nützlichen Erkenntnisse, die aus früheren experimentellen und theoretischen Untersuchungen gewonnen wurden, ist eine quantitative Charakterisierung der Flüssigkeitsdynamik auf Porenebene während der Verdunstung aus kapillarporöser Medien, aufgrund der Komplexität des Porenraums, nur selten möglich. Die Motivation dieser Arbeit ist es, die Details des Flüssigkeitsflusses und der Phasenverteilung während der Trocknung kapillarporöser Medien zu klären und die Rolle von Kapillarfilmen bei der Zufuhr von verdunsteter Flüssigkeit zu bewerten. In dieser Arbeit werden experimentelle und numerische Porennetzwerk-Simulationsstudien zur konvektiven Trocknung kapillarporöser Medien unter langsamen isothermen Bedingungen vorgestellt.

Als physikalisches Modell eines realen kapillarporösen Mediums werden zwei dichte Partikelpackungen hergestellt, die mit monodispersen Kugeln aus Glas (mittlerer Durchmesser 0,8 mm) gefüllt und zunächst entweder mit destilliertem Wasser oder mit einer Salzlösung gesättigt sind. Zwei kontrollierte Trocknungsexperimente mit diesen Packungen werden mit einem speziell angefertigten Aufbau in einem Röntgenmikrotomographen im Labormaßstab durchgeführt. Auf der Grundlage von in-situ-Tomogrammen (Voxelgröße 16,4 μm) wird die zeitliche Entwicklung der dreidimensionalen (3D) Strukturen der Flüssigkeits- und Salzablagerungen in den Packungen während der Trocknung charakterisiert. Die entsprechenden Ergebnisse zeigen deutlich die Bildung von kapillaren Flüssigkeitsringen an den keilförmigen Poren

in der Nähe der Partikel-Partikel-Kontakte. Die Ringe bleiben über eine lange Strecke mit der Packungsoberfläche verbunden, und zwar über einen langen Zeitraum der Trocknung.

Zusätzlich zu den Experimenten wird ein diskretes 3D-Porennetzwerkmodell für den Grenzfall des kapillardominierten Regimes entwickelt, das den Ringeffekt ausdrücklich berücksichtigt. Das regelmäßige 3D-Ringporennetzwerk approximiert den Hohlraum in einem Bett, das mit einer Population monodisperser kugelförmiger Teilchen kubisch gepackt ist. Der interstitielle Hohlraum zwischen den Partikeln wird durch zylindrische Verengungen approximiert. Der konkave zylinderförmige Ring approximiert den Leerraum um den Kontaktpunkt zweier benachbarter Teilchen. Primäre und sekundäre Kapillaren werden als Häse bzw. Ringe bezeichnet. Die hydraulische Konnektivität in einer flüssigen Phase wird über die primären und sekundären Kapillarstrukturen zusammen definiert.

Porennetzwerksimulationen mit und ohne diesen Effekt werden mit Messungen hinsichtlich der Trocknungskinetik und der Sättigungsprofile verglichen. Die mit Kapillarringen durchgeführten Porennetzwerksimulationen zeigen eine deutliche Verzögerung beim Übergang vom kapillargestützten Regime zum diffusionsgesteuerten Regime. Diese Simulationsergebnisse unterscheiden sich deutlich von den Vorhersagen klassischer Porennetzwerkmodelle ohne Flüssigkeitsfilme und scheinen besser mit den Experimenten übereinzustimmen, die mit realen porösen Systemen durchgeführt wurden. Es zeigt sich, dass Flüssigkeitsringe als zusätzliche hydraulische Pfade für den Feuchtigkeitstransport aus dem Inneren des Poren-/Partikel-Netzwerks an die Oberfläche dienen und somit den Trocknungsprozess deutlich beschleunigen, und sie führen zu einer räumlich homogenen Verteilung der Flüssigkeit bis hin zu niedriger Sättigung. Mit dem entwickelten Ringporennetzmodell wird auch der Einfluss der Variation der Größe von Häsen und Ringen, der Halsradienverteilung und der Grenzschichtdicke auf die Trocknungskinetik systematisch untersucht.

Außerdem wird der Stoffübergang zwischen der Oberfläche eines kapillarporösen Modellmediums und der angrenzenden gasseitigen Grenzschicht untersucht. Um die Rolle und Bedeutung von Flüssigkeitsfilmen im Stoffübergangsprozess zu quantifizieren, werden systematisch dreidimensionale Porennetzwerk-Monte-Carlo-Simulationen in Anwesenheit und Abwesenheit von diskreten Kapillarringen durchgeführt. Im Vergleich zu klassischen Porennetzwerkmodellen scheint das Porennetzwerkmodell mit Ringen die räumlich-zeitliche Entwicklung von feuchten und trockenen Bereichen an der Oberfläche des Mediums sowie deren relative Beiträge zur Nettomassenaustauschrate besser vorherzusagen. Dies wird deutlich, wenn man die analytischen Lösungen des allgemein verwendeten Schlüenderschen Modells mit den numerischen Simulationen vergleicht, die mit dem klassischen und dem Ringporennetzmodell durchgeführt wurden. Diese Studie kann als ein Schritt vorwärts in der diskreten Modellierung der Trocknung kapillarer poröser Medien mit 3D-Sekundärkapillarstrukturen betrachtet werden und dürfte für verschiedene Anwendungen im Bereich komplexer Mehrphasenströmungsphänomene in porösen Medien von Interesse sein.

Nomenclature

Latin symbols

A_l	area of liquid phase	m^2
A_s	area of solid phase	m^2
A_c	cross-section area of the container	m^2
A_k	evaporating area of throat	m^2
A_r	evaporating area of ring	m^2
A_{total}	total evaporating area	m^2
Bo	Bond number	-
d_p	particle diameter	m
g	gravitational acceleration	m/s^2
h	ring thickness	m
J	evaporation rate	kg/s
J_{max}	initial evaporation rate	kg/s
L	throat length	m
L_g	gravity length	m
\tilde{M}	molar mass	kg/kmol
\dot{M}	mass flow rate	kg/s

P	atmospheric pressure	Pa
P_v	vapor pressure	Pa
P^*	saturated vapor pressure	Pa
R	particle radius	m
\tilde{R}	universal gas constant	J/kmol . K
r_t	throat radius	m
r	ring radius	m
r_m	mean throat radius	m
S_p	liquid saturation in the packing	-
S_s	liquid saturation of slice	-
S_n	network saturation	-
S_{ij}	throat saturation	-
S_r	ring saturation	-
S_i	pore saturation	-
S_{net}	network saturation	-
S_{dry}	network saturation when network surface dries	-
T	air temperature	K
V_r	volume of ring	m^3
V_l	liquid phase volume	m^3
V_s	solid phase volume	m^3
V_c	volume of the container	m^3
V_{ij}	volume of throat	m^3
Z	coordination number	-

Greek symbols

α	half filling angle	°
β	mass transfer coefficient	m/s
δ	vapor diffusion coefficient	m ² /s
ε_0	boundary layer thickness	-
θ	surface wetness	-
ρ	density	kg/m ³
σ_0	standard deviation of throat radius	m
σ	liquid surface tension	N/m

Abbreviations

BT	bottom-top
CRP	constant rate period
CM	continuum model
μ -CT	micro computed tomography
CPNM	classical pore network model
DIABT	diagonal bottom-top
DIAFB	diagonal front-back
DIALR	diagonal left right
FRP	falling rate period
FB	front-back
IR	isolated ring
ITP	initial transition period
LR	left-right
MCD	main cluster disconnection
NLE	non-local equilibrium
PNM	pore network model

PSD	pore size distribution
PN	pore network
PNP	pore neighbor pores
PNR	pore neighbor rings
PNT	pore neighbor throats
RFP	receding front period
RPNM	ring pore network model
RNP	ring neighbor pores
RNT	ring neighbor throat
SD	standard deviation
SMT	single menisci throat
TNP	throat neighbor pores
TNT	throat neighbor throats
TNR	throat neighbor ring
TPNM	triangulation pore network model

Contents

Declaration	i
Abstract.....	ii
Kurzzusammenfassung.....	v
Nomenclature	viii
Contents.....	xii
1 Introduction and overview.....	1
1.1 Background	1
1.2 Secondary capillary structures	5
1.3 Motivation and goal.....	10
1.4 Outline of the thesis	11
2 Pore-scale drying experiments.....	13
2.1 Sample preparation.....	14
2.2 Experimental procedure.....	15
2.3 Image processing and data analysis	16
2.4 Experimental observations.....	17
2.4.1 Drying kinetics and evolution of liquid phase	17

2.4.2	Liquid structure and connectivity at low saturation	23
3	Development of 3D ring pore network model	30
3.1	Pore network geometry	30
3.1.1	Construction of pore network	30
3.1.2	Data structures	33
3.2	Drying algorithm.....	37
3.2.1	Saturation states of throats, rings and pores.....	37
3.2.2	Cluster labeling	39
3.2.3	Evaporation from throats and rings.....	42
3.2.4	Network saturation.....	44
4	Evaluation of the ring pore network model.....	46
4.1	Model parameters	46
4.2	Drying periods.....	47
4.3	Evolution of fluid transport zones.....	50
4.4	Drying time	51
4.5	Saturation profiles.....	53
4.6	Comparison with triangulation pore network model	54
5	Parametric study	60
5.1	Variation of size of throats and rings	60

5.2	Variation of throat radius distribution.....	68
5.3	Effect of boundary layer thickness.....	74
6	Role of rings in mass transfer from the surface of a drying porous medium.....	80
6.1	Background	80
6.2	Model parameters	82
6.3	Drying kinetics.....	82
6.4	Evolution of liquid structure	87
6.5	Pressure field.....	94
6.6	Comparison with classical and Schlünder's model.....	97
7	Conclusions and outlook	100
7.1	Conclusions	100
7.2	Outlook	103
	Bibliography	105
	Student work	114
	Publications list	115

Chapter 1

1 Introduction and overview

1.1 Background

A porous medium contains matrix and voids (Bear et al., 1987; Su et al., 2011; Sahimi, 2011). Matrix is usually a solid and voids (pores) are typically filled with a fluid. Porous media are very common in our life in the form of natural materials like rocks and soil, zeolites, bones, wood, cork and synthetic materials like cements, textiles and paper. Replacing a fluid in the void space or pores by another fluid has many applications such as oil recovery, infiltration of instant products and drying of porous materials. The removal of liquid from a material by means of drying can add and preserve product quality, minimize investment and operating cost, maximize process safety and minimize environmental impact.

Drying is a mass transfer process that involves successive removal of a volatile liquid by evaporation from a moist porous medium. Accurate prediction of drying kinetics of capillary (or non-hygroscopic) porous materials is technically important and scientifically challenging. As reported in many previous works (Brakel, 1980; Faure et al., 2010), the drying kinetics (that is, the relationship between mass loss and time) of a non-deformable capillary porous medium initially filled with a liquid and exposed to typical room conditions is characterized by three periods: The constant rate period (CRP), the falling

rate period (FRP) and the receding front period (RFP). The CRP corresponds to an "apparent" constant drying rate and is controlled by the external (gas-side) conditions, that is, by the relative humidity, temperature and velocity of the surrounding air. The FRP is a crossover period in-between the CRP and RFP, which is characterized by a significant drop in the drying rate. The last period, the RFP, is characterized by an internal evaporation front retreating into the porous medium during drying. The CRP/FRP transition is a vital aspect in the drying process. Actually, based on this transition point, Lehmann et al. (2008) simplified these three periods into two stages: Stage 1 consists of the CRP and stage 2 encompasses both the FRP and RFP.

Predicting the duration of CRP is of paramount importance in technical applications, since this is the period with the highest evaporation rate. A longer CRP results in a shorter drying time which, in turn, leads to a higher throughput. Traditional approach treats a partially saturated porous medium as a spurious continuum for which effective transport parameters are expressed as a function of average liquid content. Though several models have been developed within the framework of this approach (Philip et al., 1957; Luikov, 1966; Whitaker, 1998), they all have limited predictive capacity in relation to transition from the capillary-supported regime to the diffusion-controlled regime. The macroscopic continuum models (CMs), which require in-situ estimates of medium hydraulic and equilibrium properties, fail to reliably predict the CRP/FRP transition (Philip et al., 1957; Stewart, 1967). This represents a major drawback, even in sophisticated CMs (Whitaker, 1998), for a review, see Geoffroy et al. (2014). To overcome this drawback and provide a truly predictive drying model that can accurately represent the physics at the pore level, researchers have developed pore network models (PNMs) as an alternative.

A pore network model represents the void space of a porous medium by a network of interconnected capillaries with similar geometry but different radii. It uses fundamental physical laws to describe transport phenomena at the pore level. This description ensures that no geometrical and/or physical effect is lost or masked at the pore-network scale – a problem associated with the CMs.

Originally, pore network models have been used in hydrogeology (Sahimi et al., 1986) and petroleum engineering (Lenormand et al., 1988; Dillard and Blunt, 2000) to study groundwater flow and secondary oil recovery. In the early nineties, Daian and Saliba (1991) and Nowicki et al. (1992) coined the idea of discrete modeling of capillary porous materials drying. Later on, Prat (1993) proposed a first pore network drying model by using concepts of invasion percolation (Wilkinson and Willemsen, 1983) and calculation of diffusive vapor transport. Since this pioneering work, various researchers have incorporated pore-scale physical effects, either individually or combined, into this model and studied their impact on the drying characteristics of capillary porous media. Examples include gravity (Laurindo et al., 1996; Yiotis et al., 2012), liquid viscosity (Metzger et al., 2007a), gas-side boundary layer (Yiotis et al., 2007), heat transfer (Surasani et al., 2008), capillary valve effect (Wu et al., 2016; 2017) and mechanical damage caused by capillary forces (Kharaghani et al., 2011; 2012; Pham, 2021).

Many research articles based on PNMs have exploited the role that individual transport phenomena play during the drying of capillary porous media, though not fully (Prat, 1993; 2002; 2011; Metzger et al., 2007b; Segura et al., 2005; Kharaghani, 2020). These studies have primarily been conducted with pore networks of regular structure. However, structurally more refined PNMs have also been developed to better represent porous media. These are referred to as irregular (or unstructured) PNMs. For instance, the Voronoi algorithm (Voronoi, 1908) has been used to generate a three-dimensional (3D) irregular pore network to map the void space of randomly packed monodisperse particles, which are either generated numerically (Kharaghani et al., 2012) or obtained from the X-ray images of real glass beads (Wang et al., 2012a). Pham, 2021 has used regular Delaunay triangulation and its dual Voronoi tessellation to generate triangulation pore network model that can simulate the drying behavior of capillary porous aggregates made of spherical primary particles with different size distributions. The results of pore network drying simulations with irregular structures have been compared to the data obtained from X-ray drying experiments under comparable conditions (Wang et al.,

2012a). The discrepancy between the experimental and simulation results was argued to arise from an inadequate description of the mass transfer in 3D drying PNMs. This argument was based on earlier works of other groups such as the study conducted by Scheel et al. on the characterization of liquid morphology in random packings of glass beads (Scheel et al., 2008). From highly resolved images obtained using synchrotron X-ray tomography, the authors were able to visualize the structure of the liquid phase at different liquid contents (see Figs. 1.1 and 1.2). They observed that the liquid structures formed around particle-particle contact points during drainage essentially resemble capillary ring chains. Generally known similarities between the drainage and drying processes raised the questions as to whether such secondary capillary structures are relevant to drying capillary porous media and whether they can be approximated by a simple geometrical element which could be incorporated into a 3D PNM.

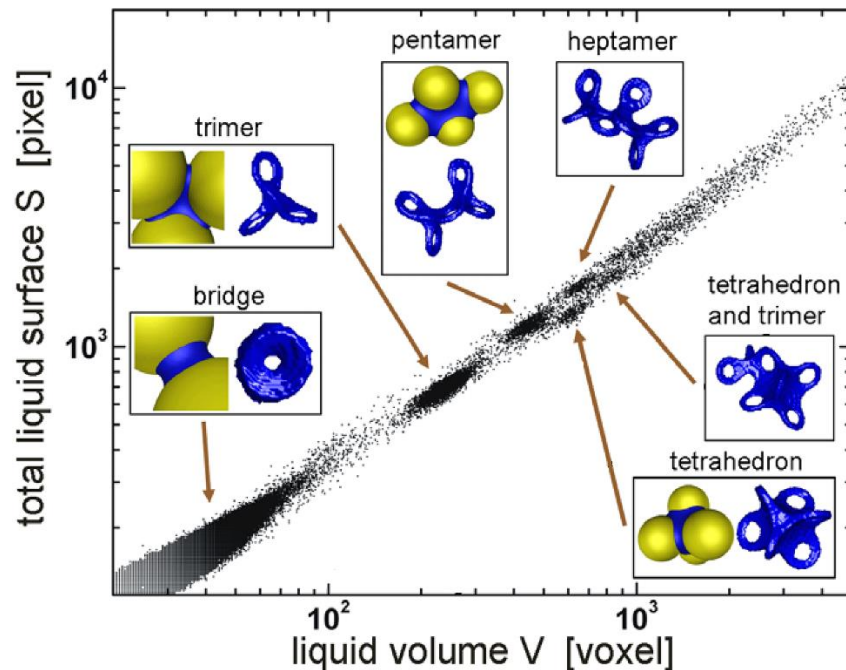


Fig. 1.1. Liquid clusters observed in 3D X-ray microtomography data. Insets show comparison of morphologies of X-ray microtomography images and numerically obtained liquid shapes (Scheel et al., 2008).

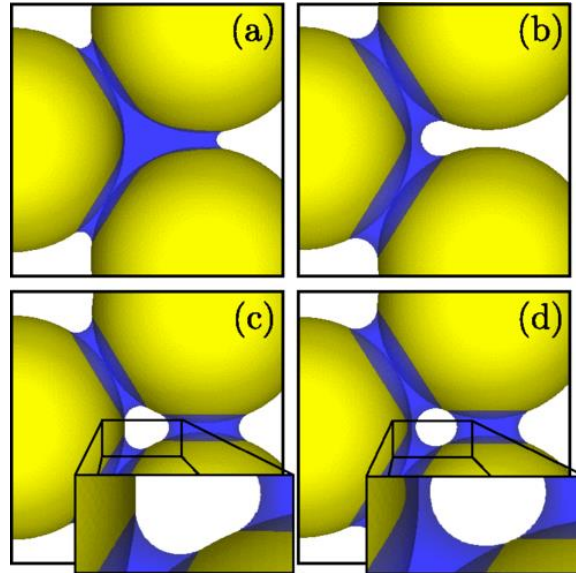


Fig. 1.2. Liquid morphologies around contact point of three spherical beads of equal radius showing (a) trimer, (b) dimer, (c) three pendular bridges, and (d) a dimer coexisting with a single pendular bridge (Semperebon et al., 2016).

1.2 Secondary capillary structures

The fact that secondary capillary structures can develop in geometrical singularities of drying capillary porous media is well known from other literature. Many experiments and numerical studies carried out in this context primarily deal with model capillary porous media, ranging from the simplest possible situation, that is, a single capillary tube of square cross-section (Bhaskaran et al., 2021; Chauvet et al., 2009; 2010), to two-dimensional micromodels (Laurindo et al., 1998; Vorhauer et al., 2015; Wu et al., 2020), a Hele-Shaw cell filled with glass beads (Yiotis et al., 2012), and to microfluidic structures (Chen et al., 2017; 2018). The secondary capillary structure can exist in gas invaded areas, the central part of which is occupied by the gas phase and liquid is trapped in corners.

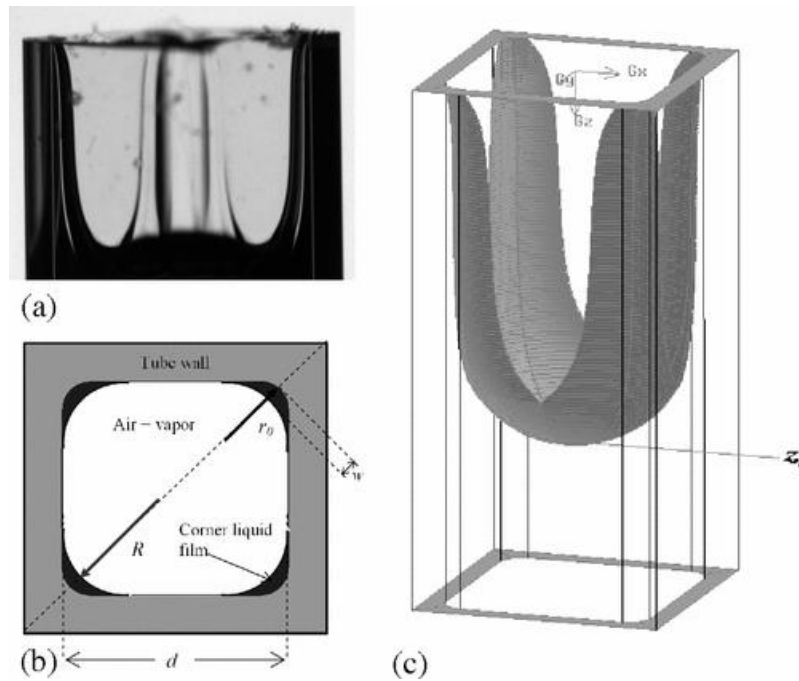


Fig. 1.3. (a) Visualization of corner liquid films in tube entrance; (b) Sketch of tube cross section in corner film region; (c) Computed shape of gas-liquid interface in the tube (Chauvet et al., 2009).

Experiments with single capillary tubes on evaporation provide information on the importance of corner films. Similar to porous media, the kinetics of evaporation in a square capillary tube with constant cross-sectional area can be divided into three stages as CRP, FRP and RFP. The evaporation rate is influenced by the geometry of the corner film at the capillary tube's entry. Nevertheless, the void space in a real porous medium is much complicated in number of pores and their shapes. The evaporation of a single capillary tube with a fixed cross-sectional area may not adequately depict the transport phenomena in porous media from this perspective. Laurindo et al., 1998, conducted drying experiments in two-dimensional etched-glass micromodels and compared their findings to predictions from a pore-network simulation without films. The experimental rates were approximately six times greater than the numerical rates. Wetting liquid films were attributed by these researchers for the improved flow. During evaporation experiments in 2D square pore networks (Vorhauer et al., 2015; Wu et al., 2020), two types

of corner films: continuous (connected to the bulk liquid) and discontinuous (not connected to any bulk liquid) are distinguished. The corner films at the pore network's margins are critical for linking the liquid-filled zones in the pore network. The geometrical structure of capillary films in random particle packings, such as those studied by Yiotis et al., 2012, is more complicated. Similar strong capillary film effects have been reported in sphere packings contained between two plates. However, the situation with traditional 3D particle packings, which are closer to genuine porous media and are not restricted between two plates (Yiotis et al., 2012), remains still somewhat unclear. Visualizations of such secondary capillary structures are shown in Figs. 1.3 to 1.6.

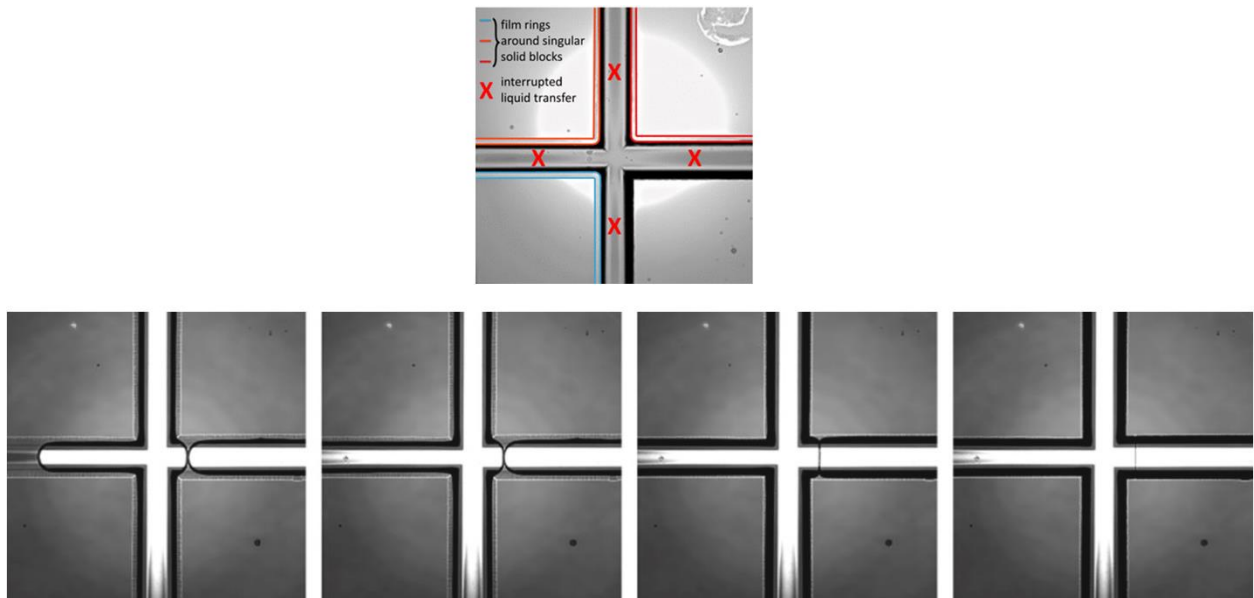


Fig. 1.4. Film forming around different neighbouring solid blocks of the pore junction. The existence of disconnected liquid film rings inside channel margins is demonstrated by CLSM images during experiments in 2D square pore networks. Throats are joined by liquid bridges in the vicinity (as seen in the eastern throat), causing all rings to shrink simultaneously (Vorhauer et al., 2015).

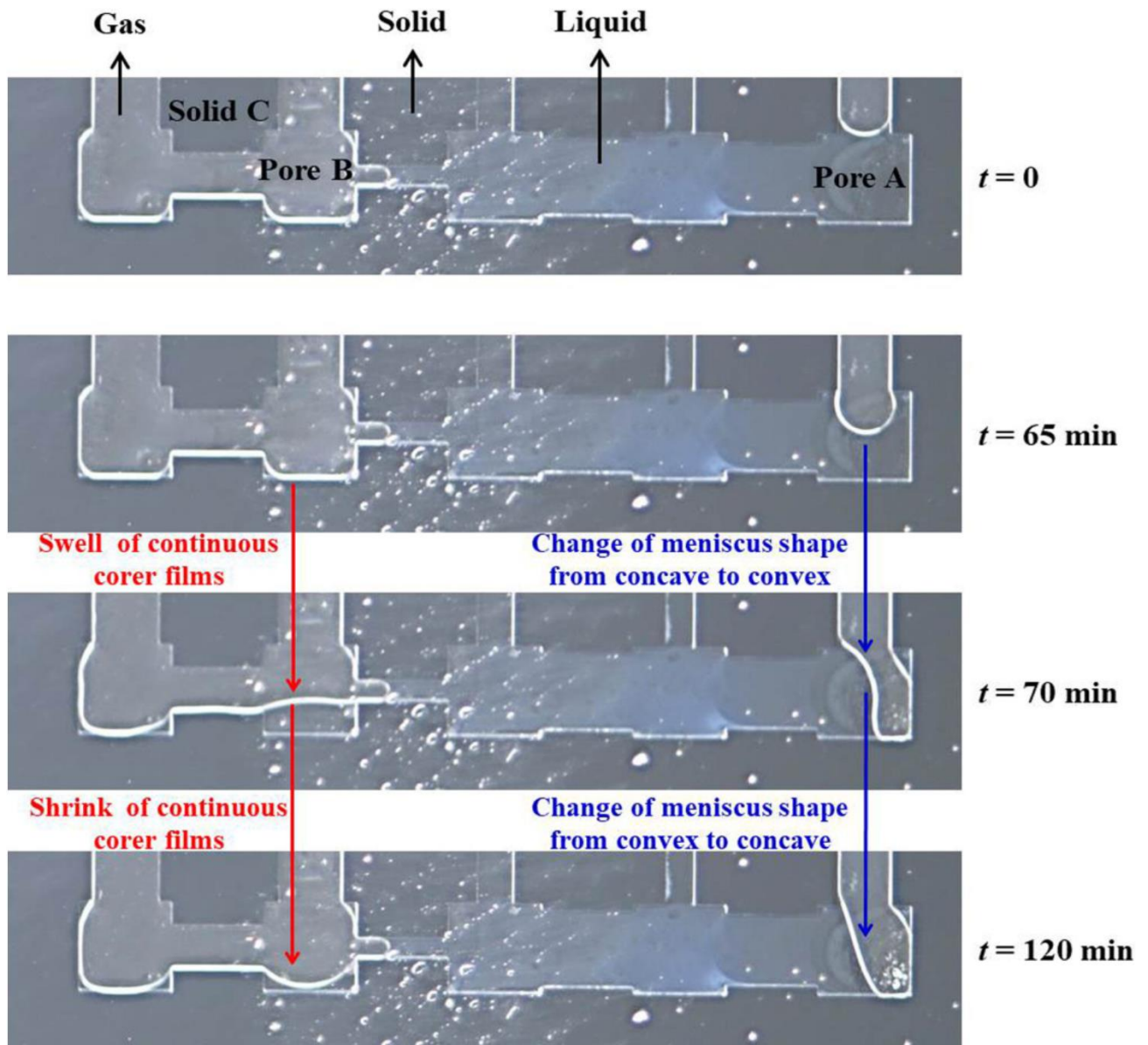


Fig. 1.5. Continuous corner films and shrinkage of liquid during evaporation experiment in the microfluidic pore network (Wu et al., 2020).

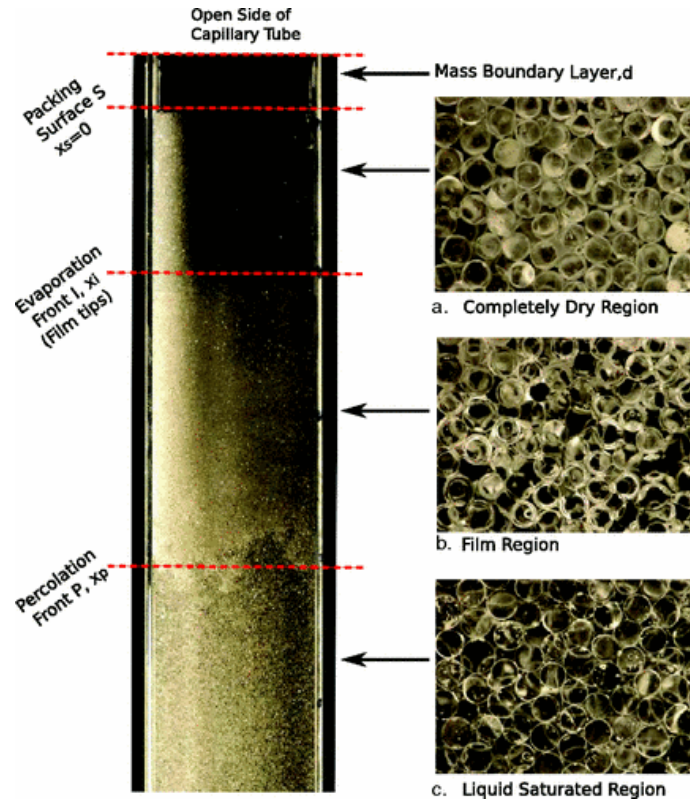


Fig. 1.6. Phase distribution patterns showing different drying regions during the drying experiments (Yiotis et al., 2012).

Many experiments, however, are limited to quasi-2D configurations which are not representative for complex geometries found in real porous media. Studies with 3D systems have been performed, notably, using model systems such as packed beds of glass beads, which are yet much more complex than 2D microfluidic porous media. Besides laboratory-based X-ray tomography (see, e.g., Haide et al., 2021 and references therein), synchrotron-based X-ray tomography (Shokri et al., 2010), neutron imaging (Derluyn et al., 2014) and magnetic resonance imaging (Donkers et al., 2017; Pel et al., 2002; Keita et al., 2013; Keita et al., 2016) are the most used techniques for imaging of liquid distribution during drying of 3D systems.

In most of these experiments and previous relevant studies, two main situations are distinguished as regards the formation of secondary capillary structures. They can either develop as long liquid capillaries trapped in corners or grooves of pores with noncircular

cross-section (referred to as continuous corner films) or as liquid chains of capillary bridges formed between particles or located around solid blocks (referred to as discrete liquid rings). The impact and dynamics of corner films have been studied using the continuous film pore network model. This model highly overestimates the extent of the corner film region and thus the predicted overall phase distribution appears to be unrealistic. In contrast to the continuous film model, the ring model can lead to phase distributions strongly resembling measured distributions (e.g., see, Vorhauer et al., 2015; and references therein). Common to all these works has been that liquid films play a crucial role in intraparticle mass transport, that is mass transport within drying capillary porous media. Whether continuous or discrete, these secondary liquid structures are commonly referred to as "thick" films. As observed in previous studies (e.g. Prat, 2007; Panda et al., 2020; Vorhauer et al., 2015), they can notably impact the drying characteristics. In addition to thick films, adsorbed films (often called "thin" films) may also develop on the solid surface of the porous medium under study (Panda et al., 2020). The thin films of nanometer thickness however are too thin to be visible to the conventional imaging techniques (Haide et al., 2021), and even if they were conceivable, previous studies show that they have a negligible impact on drying, at least for capillary porous materials (Laurindo et al., 1998).

1.3 Motivation and goal

No matter whether continuous corner films or discrete liquid rings are concerned, they complement to the mass transport and link the receding invasion (or percolation) front to the evaporation front in order to supply moisture to the external air of relatively low absolute humidity. This mechanism maintains the medium surface partially saturated as menisci recede during drying until a very low saturation and, thus, extends the duration of the CRP. At a certain invasion front depth though, the capillary flow can no longer overcome the friction forces to support liquid transport through the distance which is necessary to reach the surface. This distance is quite long relative to the medium height in case of continuous corner films, whereas it is of much smaller spatial extension in the

case that discrete liquid rings form in the medium. An evaporation front then starts to invade as the film tips recede into the medium and a completely dry region appears. Diffusion within the dry region mainly controls the drying process and the drying rate decreases as the distance between evaporation front and the outer surface increases, which is typical for the FRP/RFP. This is the state-of-the-art of understanding of mass transport mechanisms in drying systems where liquid films are present and viewed either as continuous or discrete secondary liquid structures. Whether these two complementary views can be generalized to real porous media is still an open question.

Prior to studying the possible structure and role of liquid films in drying of a real porous medium, a natural next step is to consider a full 3D physical model of a real porous medium. As explained earlier, experiments in this respect have been conducted either with quasi-2D packings or with quasi-2D micromodels. On the modeling side, several research groups have developed 2D pore network models accounting for either the continuous liquid corner films (Prat, 2007; Yiotis et al., 2003; Yiotis et al., 2004) or the discrete liquid films (Vorhauer et al., 2015). There is however no 3D pore network model for drying that accounts for discrete liquid films, to our knowledge. The major objective of the present work is thus to start filling this research gap.

1.4 Outline of the thesis

The content of the thesis is organized as follows:

Chapter 2 describes in 3D the physical drying of a real porous medium. The experiments with glass bead packing saturated with pure liquid water are discussed. Dryer setup inside X-ray microtomography device is described. The liquid structures were determined from X-ray micro computed tomography (μ -CT) images. The drying kinetics were tracked down to low saturations. The observation of secondary capillary structures in a 3D drying particle packing during the evolution of the liquid phase over time is presented.

In Chapter 3, a 3D pore network drying model that accounts for liquid capillary rings is detailed. The pore space geometry of a drying capillary porous medium is conceptualized by a regular network of geometrical elements. The whole network is described by data structures. Saturation states, connectivity and evaporation of all elements are explained.

In Chapter 4, the pore network simulation results are set out and compared to the experimental observations. The role of secondary capillary structures as auxiliary hydraulic bridges, extension of the pathways for liquid transfer and impact on resistance for vapor transport are investigated. The evolution of transport zones in pore networks is characterized. The results are compared with classical model, triangulation pore network model and experimental measurements.

Chapter 5 investigates the influence of pore structures on drying kinetics, liquid phase distribution and connectivity of liquid. For this purpose, the size of secondary capillary structure, the standard deviation of the throat size distribution and boundary layer thickness are varied.

Chapter 6 focuses on the results in terms of drying kinetics, liquid phase distribution, and vapor pressure field at the medium surface. The role of capillary rings in support of liquid transport to the medium surface is discussed. The results of classical and ring pore network models are compared against each other and Schlünder's model.

Chapter 7 presents summary and conclusions about physical model of a real drying porous medium and novel 3D ring pore network drying model. This is followed by an outlook about future work.

Chapter 2

Part of this chapter has been published in “Kharaghani, A., Mahmood, H.T., Wang, Y.J., Tsotsas, E.: Three-dimensional visualization and modeling of liquid film rings observed during drying of random particle packings. *International Journal of Heat and Mass Transfer*, 177, 121505 (2021)”.

2 Pore-scale drying experiments

Two drying experiments were performed, with two glass bead packings which were wetted either with pure water or with an aqueous solution of potassium iodide (KI). The experiment with pure water was aimed at measuring drying kinetics and liquid distribution in order to assess the prediction quality of two pore network drying models presented herein. On the other hand, the intent of the experiment with dissolved KI was to demonstrate the structure and connectivity of the liquid phase in order to provide important insights into the role of secondary capillary structures during drying. In other words, the presence of KI as an information provider allowed us to delineate the existence of capillary rings which were not observable in the experiment with pure water. In both experiments, hydrophilic glass beads with same mean diameter and same cylindrical transparent plastic container for packings were used. This experimental work was performed by Y.J. Wang and initial findings are presented in Wang et al., 2012b, 2013, 2014. The improved version of this work with some important algorithmic corrections and enriched discussion and interpretation in context of literature is presented in

Kharaghani et al., 2021. In this chapter, the experimental work is presented in line with following chapters.

2.1 Sample preparation

Hydrophilic glass beads with a mean diameter of 0.8 mm were carefully selected one by one – for high sphericity and uniform size purpose – and closely packed in a cylindrical transparent plastic container with an inner diameter of 8 mm and a height of 10 mm. The packing was initially filled with liquid up to a height of 6.6 mm (see Fig. 2.1). Using these particle packings, we succeeded to achieve sufficient X-ray penetration through the packings at a spatial resolution sufficient to resolve individual phases and phase boundaries as well as formation sites for capillary rings. On the other hand, this choice, being more or less comparable to that in relevant literature (Shokri et al., 2010), made it impossible to avoid wall effects. The reason we made this choice is that, since incorporation of capillary rings in a drying pore network model was also intended in this work, we had to consider relatively small particle packings. This is simply due to the fact that simulations over much bigger pore networks are not yet feasible.

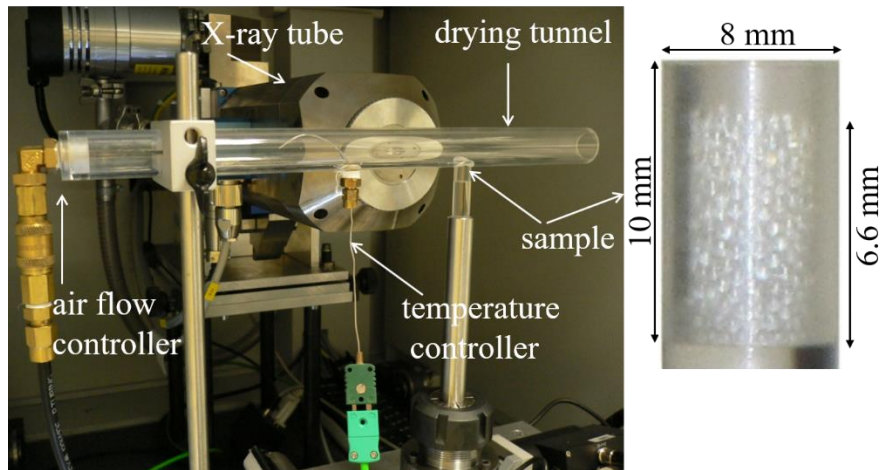


Fig. 2.1. Dryer setup inside X-ray microtomography device used for convective drying of glass bead packings.

2.2 Experimental procedure

The experimental setup employed was an improved version of a previously reported rig (Wang et al., 2012a). The major improvements were that drying measurements were conducted under well-controlled conditions and the particle packing remained firmly fixed when drying was switched to X-ray scanning or vice versa (Fig. 2.1). These improvements were achieved by introducing a cylindrical transparent plastic drying tunnel with an inner diameter of 16 mm. The tunnel was horizontally placed between the X-ray source and the detector in the micro computed tomography (μ -CT) device. The drying air was fed from the laboratory compressed air network via a mass flow controller to adjust its flow rate. The drying air was then heated to the desired temperature and directed to the drying tunnel. A circular hole with a diameter of 11.2 mm was drilled in the drying tunnel. The wet particle packing was vertically mounted on a stand and exposed through its top end to the drying air flowing with a velocity of 1 m/s and temperature of 26 °C.

μ -CT measurements were carried out with the cone beam X-ray tomography scanner CT-ALPHA (manufactured by ProCon, Germany). X-ray micro computed tomography is an imaging technique that uses projections obtained from various viewing angles to reconstruct a sample's internal structure. μ -CT is a non-invasive and non-destructive imaging technique that provides a high-resolution view of the scanned sample. The physical basis for the technique is the sample's absorption or attenuation of penetrating electromagnetic radiation. The attenuation depends on the density and the atomic components of the scanned sample. To reconstruct a map of attenuation coefficients versus position in the sample, the transmitted radiation is compared to the incident radiation. The X-ray cone beam source was generated at an acceleration voltage of 90 kV and a current of 120 μ A. For the image reconstruction in a full scan, 400 different projections, each of which with exposure time of 1 millisecond, were acquired by a flat panel detector (2300 \times 2300 pixel sensor with 16 bit gray-level resolution). The packing was

periodically exposed to drying and scanning with an average duration of around 30 min and 25 min, respectively, until it was not feasible to resolve changes in the saturation.

2.3 Image processing and data analysis

To quantify the geometrical configuration of the liquid phase during drying of the particle packings and to distinguish and identify remaining liquid, solid and gas phases in the image, several image processing steps were performed sequentially. First, the original reconstructed gray images were cropped to only consider the areas of interest, i.e. images of $501 \times 501 \times 402$ voxels with an edge length of $16.4 \mu\text{m}$ (approximately $8.2 \times 8.2 \times 6.6 \text{ mm}$), and then filtered to reduce noise. To ensure that this spatial resolution was appropriate, the following estimation was made prior to further analysis. We assumed that the monodisperse beads were regularly structured in the packings, then the geometric calculation of the complementary void space based on the diameter of the beads yielded cylindrical capillaries with an average diameter of $330 \mu\text{m}$ and capillary rings with a thickness of $100 \mu\text{m}$ (see Fig. 3.1). These values were well above the spatial resolution of the tomograms, suggesting that the quality of our microtomographic measurements was high enough. The gray images were segmented into the respective phases (solid, liquid and air) by choosing appropriate threshold values from gray-level histograms. For the packing wetted with pure water, the small X-ray attenuation coefficient of water produced a lack of contrast in the respective images. This problem was very significant at low saturation and especially in the pore spaces located near particle contact points where the amount of water or change in water volume was small. In order to sufficiently enhance the contrast of the image and separate clearly the liquid, gas and solid phase during drying, especially at low saturation, the KI solution with a concentration of 27 wt% was used in the second experiment. The iodide ion in the form of KI has been chosen as it has a higher linear X-ray attenuation coefficient than other solutes (such as NaCl), making it an effective contrast agent.

By adding tracer KI, the gray-level histogram represented the three phases as three sharp peaks separated by two valleys. In order to separate the solid, liquid and gas phases, two

threshold values of the attenuation coefficient were found in the two valleys, so as to binarize the gray-level images into black and white images for presenting the selected phase in white. Note that, contrary to the drying of a particle packing saturated with pure water, the peak presenting liquid phase moved during drying due to the salt crystals deposition. It was not possible to separate the salt deposit and salt solution directly in the gray-level histogram, because they had almost the same attenuation value. However, the morphologies of salt deposit and the remaining solution were remarkably different and thus distinguishable in 3D images rendered. This has allowed us to clearly identify the evaporation front. The spatial connectivity of a liquid structure (or a liquid cluster) was determined by an algorithm which is based on labeling of connected liquid voxels. Initially, the liquid phase is distinguished from other phases and from the background. The connectivity of the liquid voxels is given by the chosen neighborhood. A unique gray level value to liquid pixels belonging to the same connected region is assigned. In this algorithm, the continuous phase is considered as one label and each new separated liquid structure is assigned a new label.

2.4 Experimental observations

2.4.1 Drying kinetics and evolution of liquid phase

Results obtained from experiments conducted with the particle packing initially saturated with pure water are presented as drying kinetics curve and slice-averaged (or local) saturation profiles in Fig. 2.2. The overall liquid saturation in the packing, which is the volumetric fraction of the void space occupied by the liquid phase, is calculated at time t as

$$S_p(t) = \frac{V_l(t)}{V_c - V_s}, \quad (2.1)$$

and the averaged liquid saturation of horizontal slices at a given vertical coordinate z and time t as

$$S_s(z, t) = \frac{A_l(z, t)}{A_c - A_s(z)}, \quad (2.2)$$

where V_l , V_s and A_l , A_s denote the liquid and solid phase volumes and areas, respectively; V_c and A_c are the volume and cross-section area of the container, respectively. Saturation is unity when the packing (or slice) is full of liquid and null when it is full of air. These volumes and areas are calculated based on the voxel size ($16.4 \mu\text{m}$) and number of voxels ($501 \times 501 \times 402$) in the corresponding X-ray tomograms. Top 60 slices out of 402 slices collectively represent the packing surface (red dashed line in Fig. 2.2b) with a thickness which is equivalent to the particle diameter.

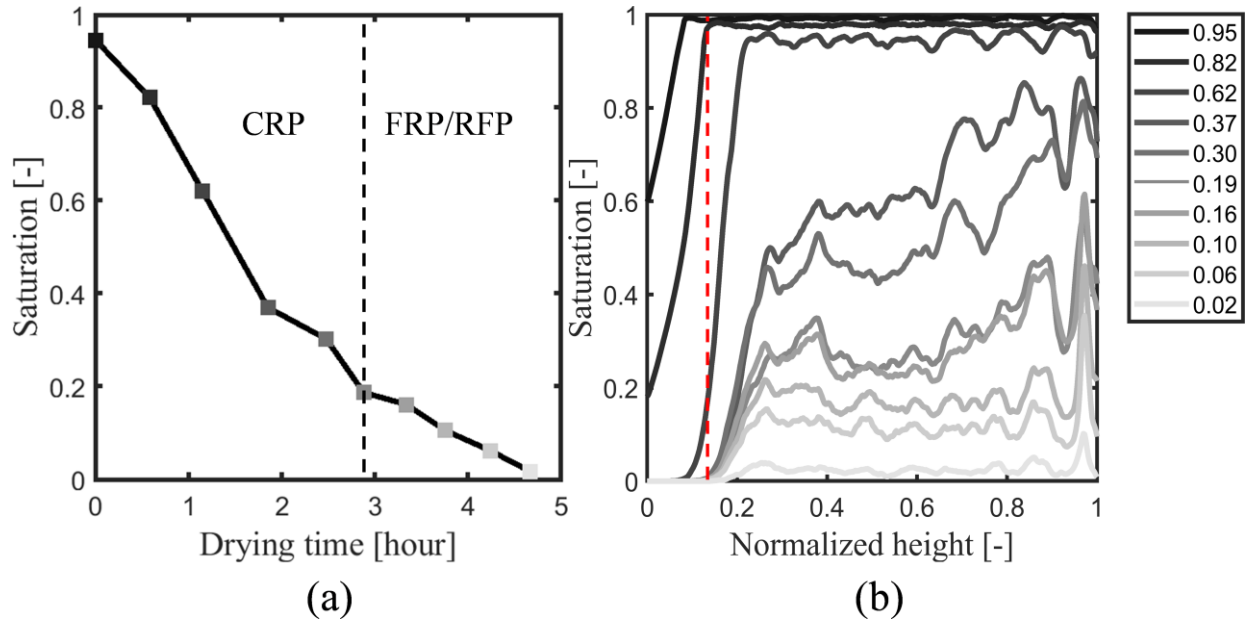


Fig. 2.2. (a) Overall saturation as a function of time for drying of particle packing initially saturated with pure water and (b) evolution of liquid phase profiles during drying (saturation are averaged horizontally and the packing evaporative surface is shown by red dashed line).

The overall drying curve of the particle packing is shown in Fig. 2.2a. Two drying periods are discerned. In the CRP the total liquid saturation decreases with a nearly constant slope for a long time. During this period the evaporation front remains pinned on the packing surface where the evaporation of liquid occurs (see Fig. 2.2b). As can be deduced

from visualizations presented in Sec. 2.4.2, the connection between the front and surface is maintained by capillary ring chains with spatial extent that controls the duration of the CRP. The surface of the packing is saturated by the capillary rings. Diffusion inside the gas phase in an empty container above the packing surface controls the CRP process. This is consistent with analysis reported in previous studies (e.g. Yiotis et al., 2004; Lehmann et al., 2008; Chauvet et al., 2010) and explored in Sec. 2.4.2. Then, there is the FRP/RFP during which the overall saturation continues decreasing, but with a smaller slope. In this period, a dry region tends to develop between the evaporation front and surface. Thus, mass transport to the surrounding bulk air is driven by vapor diffusion within the packing (see Fig. 2.2b). An increase in the thickness of the dry region gives rise to a lower rate of decrease in the saturation, simply because the diffusion rate is inversely proportional to this thickness.

One-dimensional profiles of the liquid saturation along the height of the packing are illustrated in Fig. 2.2b. The sharp decrease in saturation is apparent in a thin region adjacent to the packing surface referred to as the edge effect region (Lu et al., 2020; Moghaddam et al., 2017). This is due to preferential invasion of the gas phase from top side which is prominent down to $S_p = 0.62$. At global saturation about 0.82, the gas phase invades the bed bottom for the first time, which is commonly referred to as "breakthrough" (Moghaddam et al., 2017; Metzger et al., 2010; Le Bray et al., 1999). After this event, saturation of the bottom slice is lower than in neighboring slices, because large pores located near the bottom surface and lateral sides of the packing are invaded first by the gas phase while evaporation takes place at the packing surface. The preferential pore invasion occurs due to the porosity wall effect (the porosity of a random packing of primary particles is greater near a wall). This effect is generally expected to decay if the ratio of the bed dimension to the particle size is large enough; otherwise the effect translates throughout the bed (Winterberg et al., 2000). The wall effect is seemingly inevitable for the ratio of 10 in our case. Interestingly, in the work of Faure and Coussot 2010, where this ratio is even larger (11.3), the impact of the wall effect on the saturation

profiles measured by magnetic resonance imaging can be recognized (see Fig. 9 in this reference).

If we exclude the thin regions dominated by the top edge effect and the bottom wall effect from the profiles shown in Fig. 2.2b, two types of trends are distinguishable. In agreement with the results reported in previous studies (e.g. Faure et al., 2010; Gupta et al., 2014), the profiles are mostly uniform at high overall saturations, i.e. $S_p = 0.95, 0.82$ and 0.62 . This is attributed to capillary effects which lead to a homogenous redistribution of the liquid throughout the packing. The profiles however tend to become non-uniform at low saturations, i.e. $S_p = 0.37$ and 0.30 . The existence of this trend can be explained by the formation of liquid clusters which are mostly located in the upper half of the packing and thus evaporated preferentially over other clusters (see Sec. 2.4.2).

The gradient observed in saturation profiles could also be caused by gravity effects in the packing. The Bond number can be used to characterize the relative importance of gravity over capillary forces, which reads

$$Bo = \frac{(\rho_l - \rho_g)gd_p^2}{\sigma}, \quad (2.3)$$

where ρ_l and ρ_g denote the mass density of the liquid and gas phase, respectively; g is the gravitational acceleration, d_p is the particle diameter and σ is the liquid surface tension. To further explore the role of gravity, one may also estimate the gravity length L_g , which represents the distance over which interfacial pressure difference becomes equal to pressure difference due to gravity (Laurindo et al., 1996),

$$L_g = \frac{\sigma}{d_p g \rho_l}. \quad (2.4)$$

A small Bond number ($Bo = 0.09$) and the fact that the gravity length ($L_g = 9.3$ mm) is higher than the packing height (6.6 mm) imply that the overall impact of gravity on the drying process was very limited.

At lower network saturations, profiles are mostly uniform because a large number of very small liquid clusters span the entire packing.

Figure 2.3 shows three dimensional images of spatial liquid distribution over time at the overall saturation of particle packing and complements Fig. 2.2. The connectivity of liquid remains dominant until a very low saturation, i.e. 0.06. Large pores exist along the container's wall and preferentially empty during the course of drying (see Fig. 2.3).

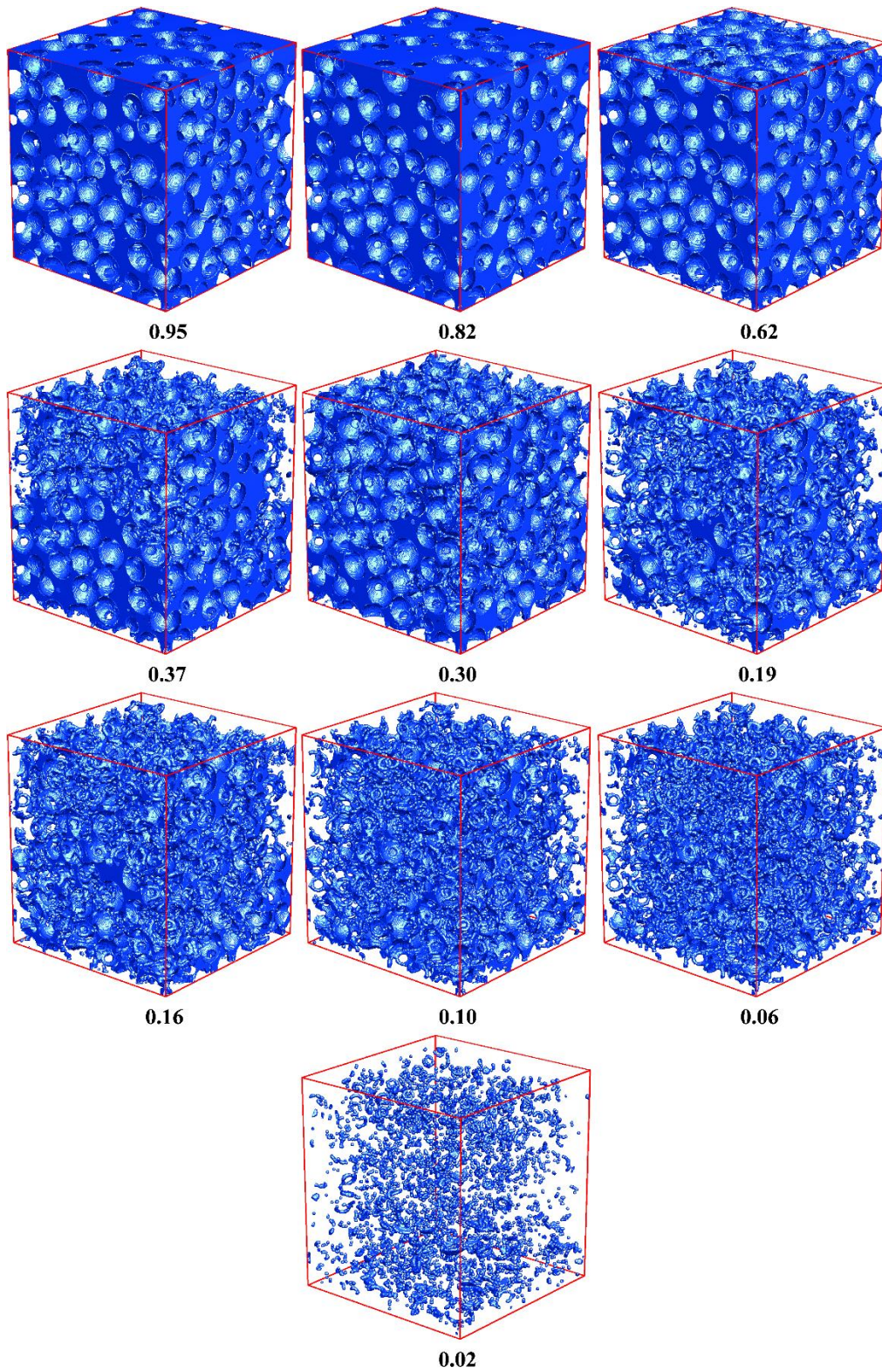


Fig. 2.3. Visualization of evolution of spatial liquid distribution during drying experiment at packing saturations of 0.95, 0.82, 0.62, 0.37, 0.30, 0.19, 0.16, 0.10, 0.06 and 0.02.

2.4.2 Liquid structure and connectivity at low saturation

Results of experiments performed with the particle packing moistened with KI solution are presented in this section with the purpose of providing insight into the geometrical structure and spatial connectivity of the liquid phase. Figure 2.4 shows the liquid and salt deposit formed at the packing surface as 3D rendering images obtained from the μ -CT tomograms. In order to make more noticeable large liquid clusters at very low saturations, we have refrained from visualization of isolated small liquid clusters (and solid deposit) at saturations below 0.048.

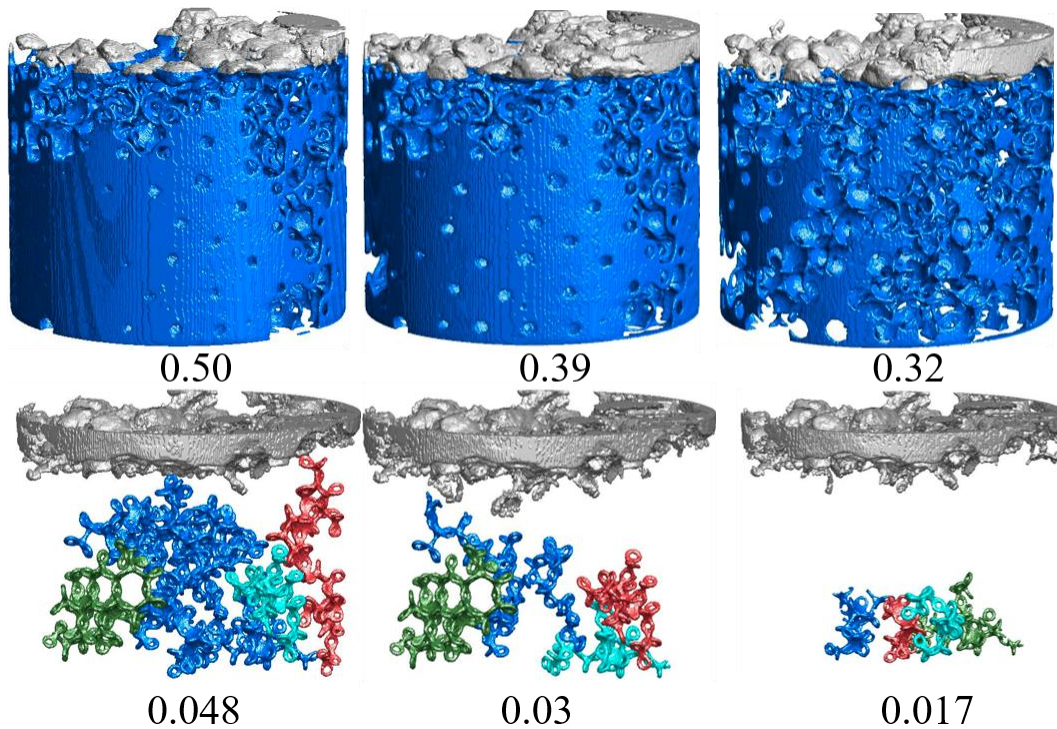


Fig. 2.4. Geometrical structure of liquid at six different values of overall liquid saturation during drying of particle packing. Only liquid and salt deposit are shown, and liquid clusters are labeled in blue, green, red and cyan by decreasing volume. Salt deposition at the surface of packing is shown in gray.

It is apparent that the structure of the liquid phase undergoes substantial changes during the drying process. The liquid appears to start fragmenting, i.e., the formation of clusters sets on, at saturation 0.50 while it remains connected to the evaporation surface. The

liquid fragmentation is attributed to consecutive invasion of the gas phase into large pores bounded by glass beads and located near the lateral walls of the packing container. These pores account for a large fraction of the entire pore space and they are defined as primary capillary structures. During gas invasion the interconnection between primary capillaries permits the flow of liquid from large capillaries to small ones. Such major physical effect of liquid pumping has already been reported in Wang et al. (2012a), but only down to a liquid saturation of 0.20.

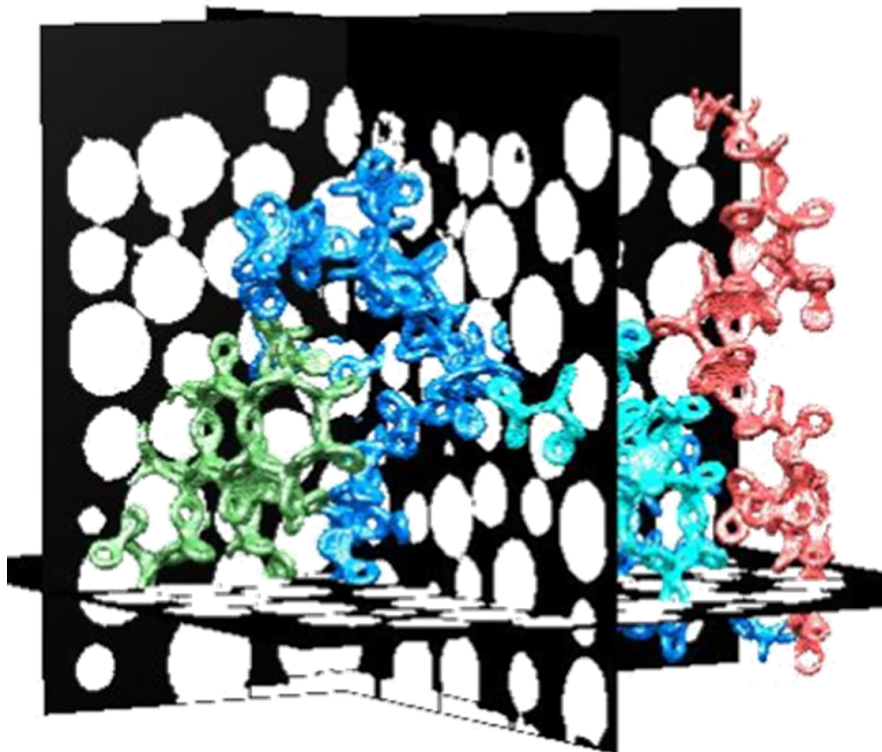


Fig. 2.5. Four liquid clusters are labeled in blue, green, red, and cyan by decreasing volume at saturation 0.048 showing position of capillary rings.

While the gas invasion progresses in primary capillaries (see Fig. 2.4 at saturation 0.32), liquid resides in the vicinity of the contact points between pairs of adjacent particles. This relatively small fraction of the pore space is defined as secondary capillary structures which resemble 3D capillary rings (or pendular bridges) (Scheel et al., 2008; Badetti et al., 2018). The capillary rings help maintain the packing surface partially wet by providing

hydraulic communication between bulk liquid regions that appear macroscopically isolated. At saturation 0.048 four large (in terms of volume) chains of liquid rings are identified across the entire packing. The largest chain (in blue) stays connected to the evaporation surface, which is still near the packing top surface, until the saturation reaches 0.03 (see Figs 2.4 and 2.5).

Geometrical structure and spatial extent of liquid clusters at saturation 0.048 are illustrated in Fig. 2.6. The liquid clusters are classified into six different groups according to their volume. As can be seen, the liquid has been split up into many clusters with large liquid-air interface that are distributed throughout the packing. The largest clusters are mainly formed in the packing center over a distance comparable to the packing height, while the isolated rings are favorably developed near the walls of the container. The presence of the wall and the different structure of the packing near the wall are the key attributes for the formation of isolated rings along the walls of the container. Total

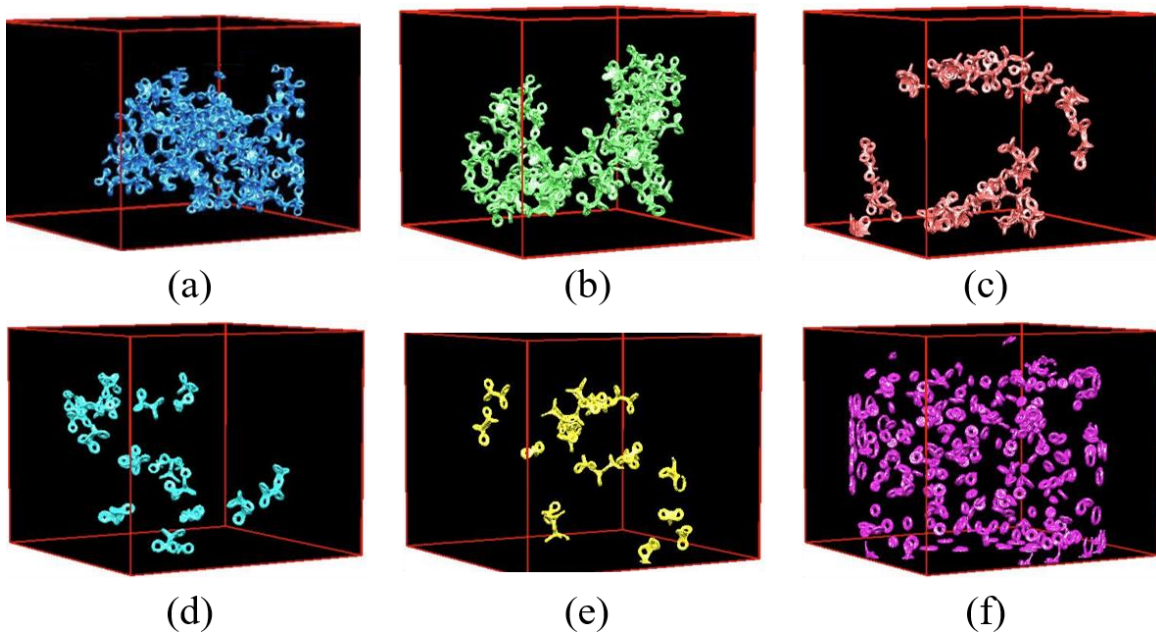


Fig. 2.6. Volume range and number of liquid clusters at an overall liquid saturation in the packing of 0.048: (a) larger than $2 \times 10^5 \mu\text{m}^3$, 6, (b) $0.8-2 \times 10^5 \mu\text{m}^3$, 12, (c) $0.4-0.8 \times 10^5 \mu\text{m}^3$, 19, (d) $0.2-0.4 \times 10^5 \mu\text{m}^3$, 14, (e) $0.12-0.2 \times 10^5 \mu\text{m}^3$, 22, and (f) $0.03-0.12 \times 10^5 \mu\text{m}^3$, 350.

number of clusters increases with decreasing saturation of the packing, which means role of rings becomes important for moisture transport towards the packing surface.

The main liquid cluster keeps the evaporation front close to the surface and maintains high evaporation rate while the region infiltrated by the gas phase grows due to long distance connection (Laurindo et al., 1998; Le Bray et al., 1999; Yiotis et al. 2006). It is therefore interesting to characterize the time evolution of the main liquid cluster volume during drying. Figure 2.7 shows the relative volume of the main liquid cluster with respect to the total liquid volume inside the packing. Based on liquid volume three regions are distinguished: The main liquid cluster occupies almost the entire liquid phase and the evaporative liquid is supplied mainly by liquid flow through the main cluster in region I. Due to fragmentation of the main cluster, liquid clusters of various sizes grow in region II. In region III, number of clusters is huge and all clusters are relatively small, as can be seen in Figs. 2.4 and 2.6.

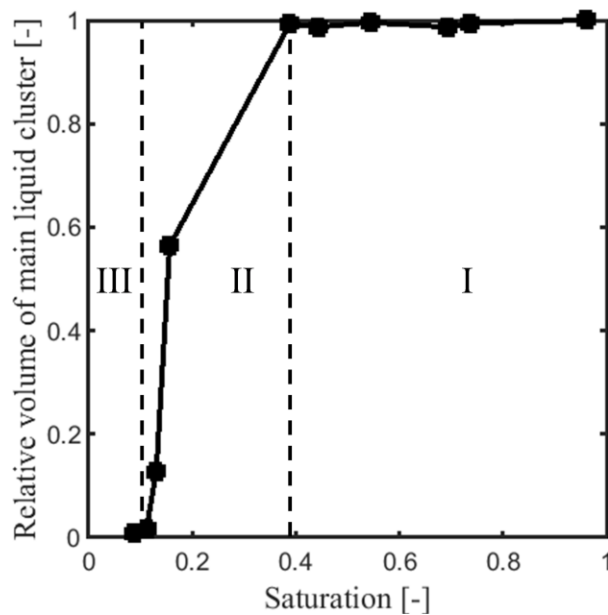


Fig. 2.7. Volume of the main liquid cluster relative to the total liquid volume as a function of overall liquid saturation in the packing wetted with KI solution.

During drying of the packing saturated with salt solution, the salt ions were transported with the liquid through the capillary flow towards the evaporation front, resulting in a salt concentration gradient. Crystallization occurs when the concentration of salt solution reaches the saturation concentration (Rad et al., 2013; Börnhorst et al., 2016). The crystal layer has a major impact on the drying process, even preventing or severely reducing it if the average size of the glass beads is small. The crystal layer, however, does not affect significantly the drying process when the average size of the glass beads is sufficiently large (Eloukabi et al., 2013). The two regimes correlate to two distinct forms of efflorescence (crystallization at the surface of the drying medium). Crusty efflorescence occurs when efflorescence gradually creates a compact crust that covers the whole surface of the porous medium at the end of drying. For the larger bead sizes, the efflorescence produces patches with a significant portion of the surface free of efflorescence which is referred as patchy efflorescence. The efflorescence appears initially on the periphery of the packing surface. The greater interstitial velocity in periphery induces the preferential onset of the efflorescence at the periphery. From the periphery of packing surface, the efflorescence gradually invades the rest of the surface similar to centripetal colonization process. When the efflorescence loses its hydraulic connection to the aqueous solution in the porous medium, it stops growing. According to the difference in 3D morphology between the salt deposit (irregular aggregates) and the liquid rings shown in Fig. 2.8, the evaporation front is tracked during drying. As can be seen, despite low saturation 0.048, the dissolved salt yet can be transported through highly complex liquid paths towards the packing surface to solidify where the evaporation occurs. Based on earlier studies conducted with ionic solutions (Rad et al., 2013), we conjecture that the salt deposits at the surface could be porous and thus feed the surface with liquid water as long as the liquid rings remain connected during drying. In applications such as the salt decay problem the development of continuous capillary rings is actually desirable, because they favor the formation of salt efflorescence, which is much less detrimental than subflorescence (crystallization within the drying porous medium) (Rodriguez-Navarro et al., 1999; Eloukabi et al., 2013).

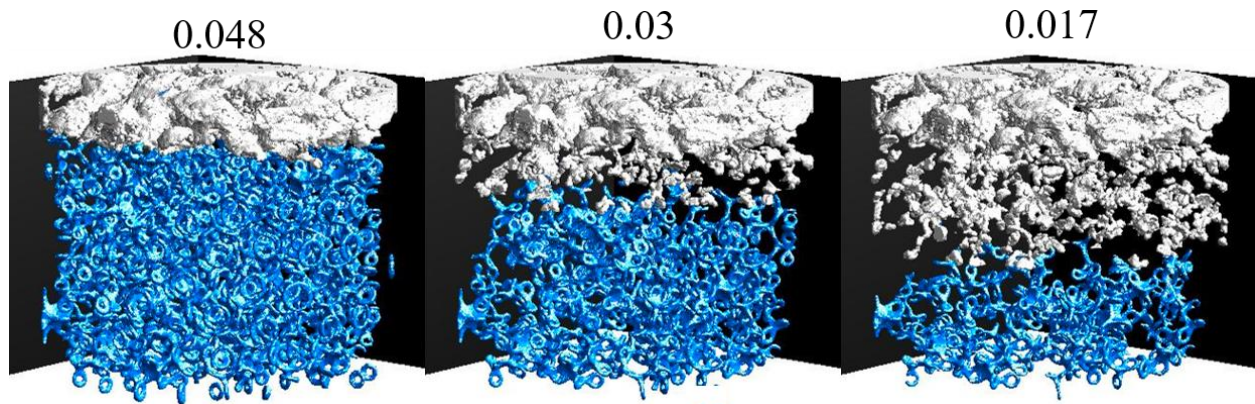


Fig. 2.8. Network of liquid capillary rings and salt deposit, as they gradually develop during the drying of a particle packing (salt deposit in gray and liquid phase in blue). Evaporation front, which can be identified at the interface between salt deposit and the rings, recedes towards the bottom of the packing during drying. The overall liquid saturation in the packing decreases from 0.048 to 0.017.

By further evaporation, the formation and propagation of salt deposit inside the packing demonstrates that the liquid can no longer be supported to balance the evaporation flux at the surface, because the large ring chains split into small disconnected networks of capillary rings (Fig. 2.8 at saturations 0.03 and 0.017). The evaporation front invades the distributed isolated liquid clusters and thus single capillary rings dry out progressively towards the bottom of the packing. The depinning of the capillary rings from the packing surface signals the FRP/RFP. Dry region develops under the evaporative packing surface and the drying period controlled by water vapor diffusion starts. The slowly receding evaporation front increases the diffusion path length and results in reduction of drying rate during FRP/RFP (Fig. 2.9). While some evaporation occurs at the packing surface during the FRP, evaporation occurs inside the packing during the RFP. During RFP, the formation of subflorescence starts. Number of isolated rings is huge and existing clusters are relatively small.

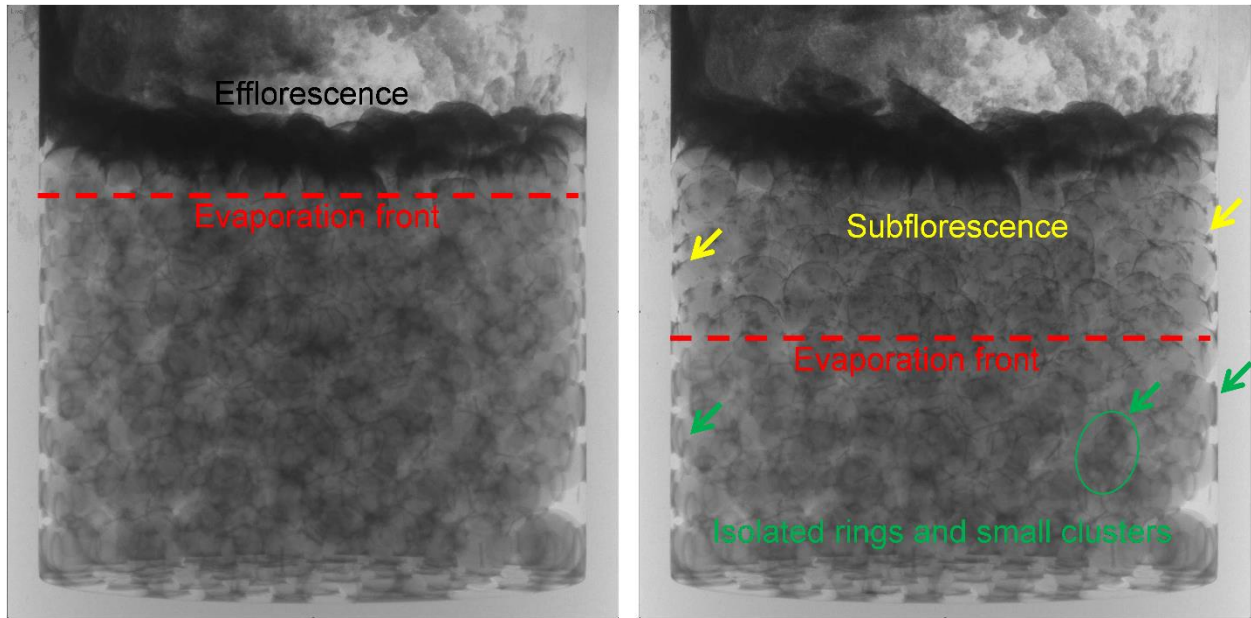


Fig. 2.9. Evaporation front is receding towards the bottom of the packing during FRP/RFP which can be seen at the intersection of the salt deposit and the rings.

The pertinent question now is whether the impact of film rings on drying can be studied by a pore network approximation of the pore space and the related drying algorithm. To address this question, a 3D pore network drying model that takes into account the capillary ring effect is developed in Chapter 3.

Chapter 3

Part of this chapter has been published in “Kharaghani, A., Mahmood, H.T., Wang, Y.J., Tsotsas, E.: Three-dimensional visualization and modeling of liquid film rings observed during drying of random particle packings. *International Journal of Heat and Mass Transfer*, 177, 121505 (2021)”.

3 Development of 3D ring pore network model

The skeleton of this ring pore network model was available at the beginning of this author's research work in October 2017, as presented in Wang et al. (2013, 2014), though with serious deficiencies and very limited description. As can be seen in Fig. 8 of Wang et al. (2014), slope of drying curve shows drying in RFP being faster than in CRP, which illustrates a fundamental problem with the drying algorithm. The concept of mass transport zone was not there at the start of this PhD work. In this chapter, 3D regular pore network drying model is described in two parts: Network geometry and drying algorithm.

3.1 Pore network geometry

3.1.1 Construction of pore network

The complex pore space geometry of a drying capillary porous medium is often conceptualized by a network of numerical pores interconnected by cylindrical throats (Laurindo et al., 1998; Metzger et al., 2007a), by a network of numerical throats

interconnecting spherical pores (Yiotis et al., 2001), or by a network of spherical pores interconnected by cylindrical throats (Lu et al., 2020; 2021). Contrary to these classical pore network models, but similar to a previous 2D pore network model by Vorhauer et al. (2015), the present regular 3D ring pore network model (RPNM) consists of three geometrical elements, i.e. throats, rings and numerical pores. This pore network may approximate the void space in a bed cubically packed with a population of monodisperse spherical particles. The interstitial void space between particles is approximated by throats, which are cylindrical tubes with uniform length equal to particle diameter and with radii generated randomly from a normal distribution function. As schematically shown in Fig. 3.1, the mean radius of throats is calculated from the particle radius R as

$$r_t = \sqrt{2R^2} - R. \quad (3.1)$$

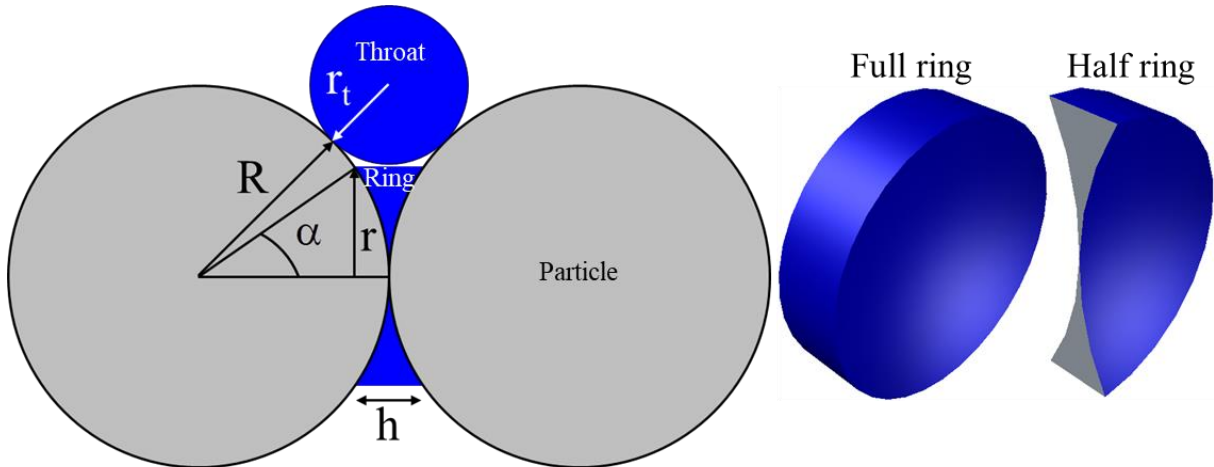


Fig. 3.1. Geometrical illustration of two particles, a throat and a ring.

The void space around the contact point of two adjacent particles is approximated by a ring with a shape of concave cylinder. Throats and rings are referred to as primary and secondary capillaries, respectively. The radius r and thickness h of rings are calculated from the particle radius R and from the half-filling angle α as

$$\alpha = \tan^{-1} \frac{R - r_t}{R}, \quad (3.2)$$

$$r = |R \sin \alpha|, \quad (3.3)$$

$$h = R - |R \cos \alpha|. \quad (3.4)$$

The volume of rings is calculated as

$$V_r = 2\left(\pi r^2 h - \frac{3}{\pi}(3R - |R \cos \alpha|)h^2\right). \quad (3.5)$$

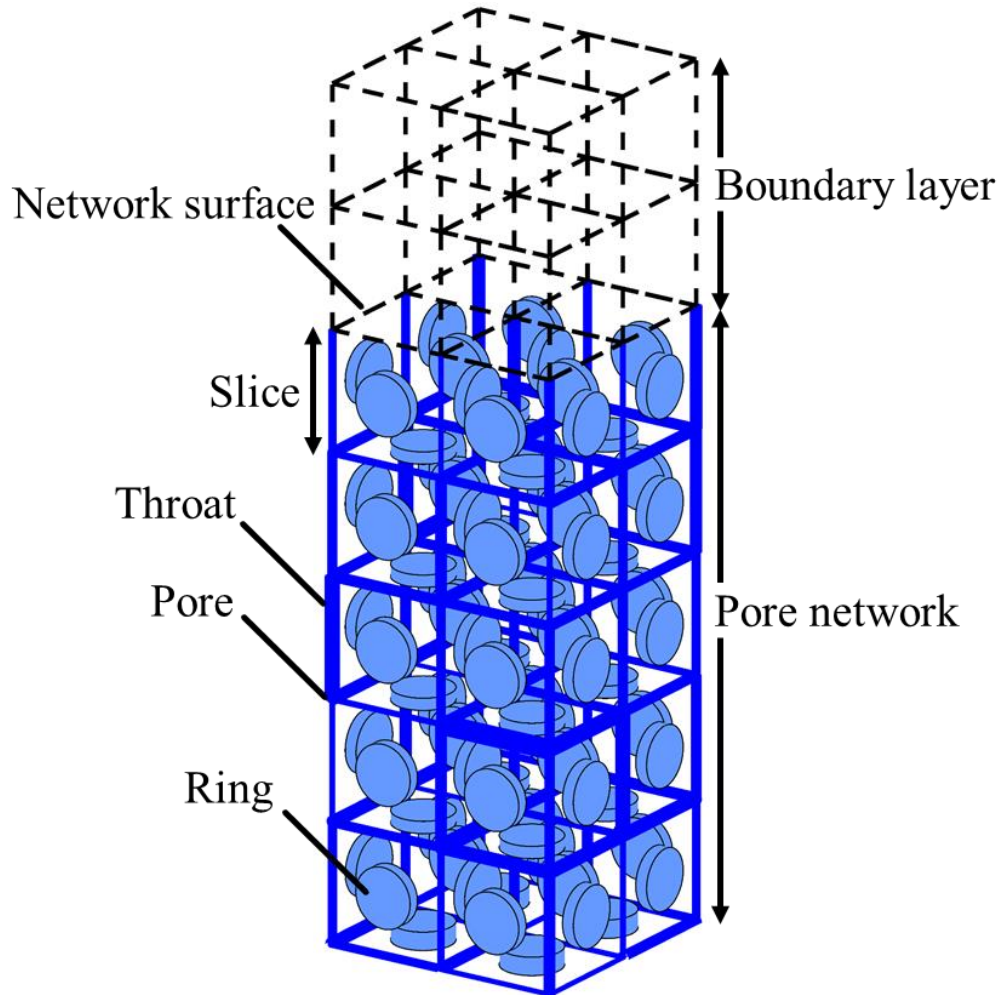


Fig. 3.2. Representation of a 3D ring pore network with the gas-side boundary layer attached to the network surface.

In addition to throats and rings, pores without volume exist, which act as numerical nodes between throats. The state variables, such as liquid or vapor pressure, are evaluated at the pores.

A small 3D cubic ring pore network is depicted in Fig. 3.2, where the gas-side boundary layer is shown in black dashed lines. Each cube in the network represents one solid particle. Contact points of these particles are located at the center of each face of the cube. Disks on each face of each cube illustrate rings. Edges and vertices of each cube illustrate throats and pores, respectively. The liquid evaporates from the top side of the network and periodic boundary conditions are imposed in lateral directions, which increases the connectivity of elements.

3.1.2 Data structures

The spatial positions of pores and rings, connectivity matrices for pores, throats and rings as well as pore, throat and ring labels are structured in several data matrices and used in the drying calculation. Data structures describe the whole network. Well described data structures are essential for efficient drying algorithm. An illustrative example with a small network as shown in Fig. 3.3 is used to describe the data structures. The periodic boundary condition is defined in the data structures as well.

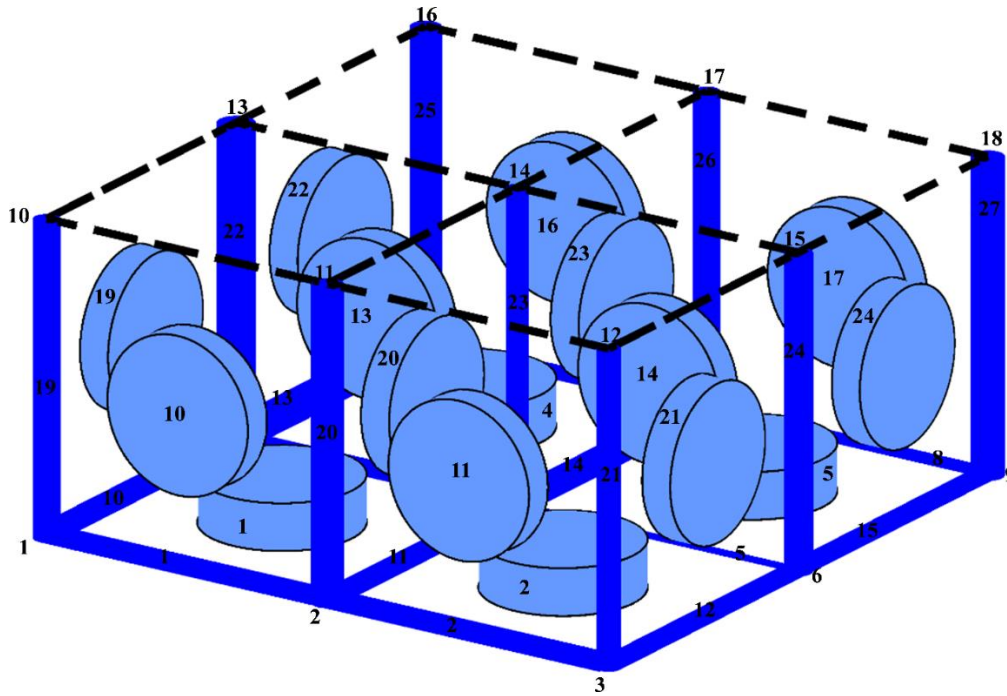


Fig. 3.3. Description of data structures with illustrative example of small 3D cubic ring pore network; (Dashed lines are boundary layer).

The construction of a regular 3D cubic network starts by calculating the total number of geometrical elements based on the number of pores in x, y and z directions, arranging their positions, and numbering. The pore positions are defined from distance between two pores in x, y and z directions. In this work, the distance between two pores is uniform and defined as throat length. First, each pore is numbered in sequence (see vertex numbering from 1 to 18 in Fig. 3.3) and pore positions are stored in an array. Then, the throats defined as connections between two neighbor pores are numbered indirectly by the TNP (throat neighbor pores) array:

$$\text{TNP} = \begin{bmatrix} 1 & 2 \\ 2 & 3 \\ 3 & 1 \\ \vdots & \vdots \end{bmatrix}.$$

Throats are numbered in sequence of x, y and z directions (see edge numbering from 1 to 27). In order to number the rings in a certain sequence and calculate the center position of the rings, the 3D cubic network is divided into three sections: Bottom-top (BT) faces, front-back (FB) faces and left-right (LR) faces. The data structures DIABT (Diagonal Bottom Top), DIAFB (Diagonal Front Back) and DIALR (Diagonal Left Right) store the diagonal pores (one diagonal out of two diagonals) of each face, respectively:

$$\text{DIABT} = \begin{bmatrix} 1 & 5 \\ 2 & 6 \\ 3 & 4 \\ \vdots & \vdots \end{bmatrix}, \text{DIAFB} = \begin{bmatrix} 1 & 11 \\ 2 & 12 \\ 3 & 10 \\ \vdots & \vdots \end{bmatrix}, \text{DIALR} = \begin{bmatrix} 4 & 10 \\ 5 & 11 \\ 6 & 12 \\ \vdots & \vdots \end{bmatrix}.$$

These data structures are used to calculate the center of each ring by using midpoint formula on two diagonal pores (x_1, y_1, z_1) and (x_2, y_2, z_2) of the same face

$$\left(\frac{x_1 + x_2}{2}, \frac{y_1 + y_2}{2}, \frac{z_1 + z_2}{2} \right),$$

and then position of the rings is stored in an array in sequence of BT, FB and LR (see numbering of cylinders on each face from 1 to 27). Thus, the rings are numbered indirectly by RNP (ring neighbor pores) array in the same sequence:

$$\text{RNP} = \begin{bmatrix} 1 & 2 & 4 & 5 \\ \vdots & \vdots & \vdots & \vdots \\ 2 & 3 & 11 & 12 \\ \vdots & \vdots & \vdots & \vdots \\ 1 & 4 & 10 & 13 \\ \vdots & \vdots & \vdots & \vdots \end{bmatrix}.$$

With this, the definition of the network geometry is complete. The additional arrays describing the neighboring relations are only defined for convenience in the drying algorithm. First, pore neighboring relation arrays: PNP (pore neighbor pores), PNT (pore neighbor throats) and PNR (pore neighbor rings). Maximum number of neighboring pores of a pore is 6, neighboring throats of a pore is 6 and neighboring rings of a pore is 12:

$$\text{PNP} = \begin{bmatrix} 10 & 7 & 4 & 3 & 2 & 0 \\ 11 & 8 & 5 & 3 & 1 & 0 \\ 12 & 9 & 6 & 2 & 1 & 0 \\ \vdots & \vdots & \vdots & \vdots & \vdots & \vdots \end{bmatrix}, \text{PNT} = \begin{bmatrix} 19 & 16 & 10 & 3 & 1 & 0 \\ 20 & 17 & 11 & 2 & 1 & 0 \\ 21 & 18 & 12 & 2 & 3 & 0 \\ \vdots & \vdots & \vdots & \vdots & \vdots & \vdots \end{bmatrix},$$

$$\text{PNR} = \begin{bmatrix} 1 & 3 & 7 & 9 & 10 & 12 & 19 & 25 & 0 & 0 & 0 & 0 \\ 1 & 2 & 7 & 8 & 10 & 11 & 20 & 26 & 0 & 0 & 0 & 0 \\ 2 & 3 & 8 & 9 & 11 & 12 & 21 & 27 & 0 & 0 & 0 & 0 \\ \vdots & \vdots & \vdots & \vdots & \vdots & \vdots & \vdots & \vdots & \vdots & \vdots & \vdots & \vdots \end{bmatrix}.$$

Second, throat neighboring relation arrays: TNP defined before, throat neighbor throats are stored in TNT, the pores by which they are associated are stored in TNP2 and throat neighbor rings are stored in TNR. The maximum number of neighboring throats of a throat is 10 and maximum number of neighboring rings of a throat is 4:

$$\text{TNT} = \begin{bmatrix} 19 & 16 & 10 & 3 & 20 & 17 & 11 & 2 & 0 & 0 \\ 20 & 17 & 11 & 1 & 21 & 18 & 12 & 3 & 0 & 0 \\ 21 & 18 & 12 & 2 & 19 & 16 & 10 & 1 & 0 & 0 \\ \vdots & \vdots & \vdots & \vdots & \vdots & \vdots & \vdots & \vdots & \vdots & \vdots \end{bmatrix},$$

$$\text{TNP2} = \begin{bmatrix} 1 & 1 & 1 & 1 & 2 & 2 & 2 & 2 & 0 & 0 \\ 2 & 2 & 2 & 2 & 3 & 3 & 3 & 3 & 0 & 0 \\ 3 & 3 & 3 & 3 & 1 & 1 & 1 & 1 & 0 & 0 \\ \vdots & \vdots & \vdots & \vdots & \vdots & \vdots & \vdots & \vdots & \vdots & \vdots \end{bmatrix},$$

$$\text{TNR} = \begin{bmatrix} 1 & 7 & 10 & 0 \\ 2 & 8 & 11 & 0 \\ 3 & 9 & 12 & 0 \\ \vdots & \vdots & \vdots & \vdots \end{bmatrix}$$

Last, ring neighboring relation arrays: RNP defined before, ring neighbor throats are stored in RNT and maximum number of neighboring throats of one ring is 4:

$$\text{RNT} = \begin{bmatrix} 1 & 4 & 10 & 11 \\ \vdots & \vdots & \vdots & \vdots \\ 2 & 20 & 21 & 0 \\ \vdots & \vdots & \vdots & \vdots \\ 10 & 19 & 22 & 0 \\ \vdots & \vdots & \vdots & \vdots \end{bmatrix}$$

The ring data structures of the model can be generated by using the correlations between them. The algorithm to generate the ring data structures for 3D cubic network geometry is as follows:

- Generate diagonal pores matrix.
- Generate ring positions in the network.
- Generate the “ring neighbor pores” matrix (“RNP”) by scanning diagonal pores of the face.
- Generate the “ring neighbor throats” matrix (“RNT”) by scanning duplicate throats from all connected throats of each neighboring pore of ring.
- Generate the “pore neighbor rings” matrix (“PNR”) by scanning “RNP” matrix for each pore.
- Generate the “throat neighbor rings” matrix (“TNR”) by scanning “RNT” matrix for each throat.

3.2 Drying algorithm

The drying algorithm is essentially an extension of previous works (Prat, 1993; Metzger et al., 2007a; Vorhauer et al., 2015); however, it is limited to the capillary dominated regime. This means any physical effect caused by viscous or gravitational forces is neglected (Sahimi, 2011). The drying process is isothermal, and the drying air with zero moisture content is at room temperature and atmospheric pressure. Liquid exists only as "free" capillary water. The liquid evaporates from the top side by convective drying. Periodic boundary conditions are applied in horizontal directions to eliminate the border effect. In order to facilitate the understanding of this section, salient algorithm components are described in individual subsections.

3.2.1 Saturation states of throats, rings and pores

Initially, all throats and rings in the network are fully saturated with liquid water. Due to evaporation, throat saturation S_{ij} varies among three states: Full containing one or two menisci ($S_{ij} = 1$), partially filled containing one or two menisci ($0 < S_{ij} < 1$) and empty ($S_{ij} = 0$), as shown in Fig. 3.4. Full throats are additionally categorized into surface and inner throats. The surface throats are directly in contact with the gas-side boundary layer via menisci, whereas the menisci in inner throats develop when the gas phase penetrates into one of their neighboring pores. The pressure at the liquid sides of the menisci drops according to respective capillary pressure. In the wake of capillary pressure difference liquid flows and the menisci relocate. The displacement of the menisci can also be caused by liquid evaporation. At some stage during drying, full or partially-filled throats become empty throats (also called gas throats), which are classified into three types according to the saturation state of neighboring gas pores: With both pores at the equilibrium vapor pressure, with one pore at the equilibrium vapor pressure and the other one at unknown vapor pressure, with both pores at unknown vapor pressure. In first type of gas throats, referred to as non-diffusive gas throats, vapor transfer does not occur. Number of non-diffusive gas throats during drying is one of the crucial parameters to estimate the impact of rings on moisture transfer. By contrast, in second and third types of gas throats,

referred to as diffusive gas throats, vapor is transported by diffusion due to the difference in vapor pressure between two neighboring pores.

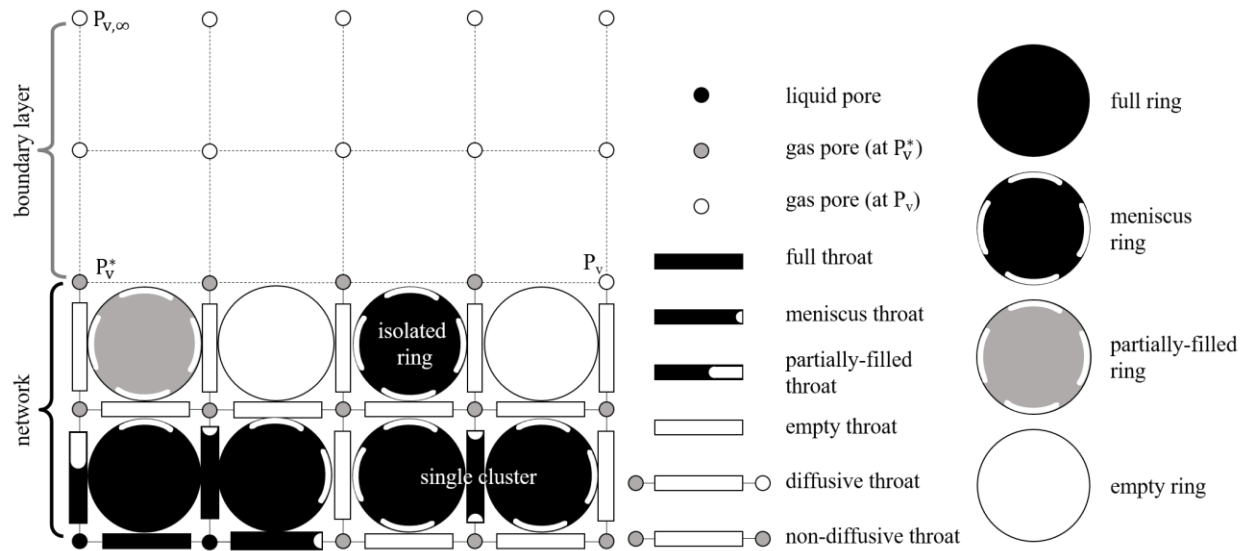


Fig. 3.4. Pictorial representation of a partially saturated pore network with gas-side boundary layer. Different saturation states of pores, throats and rings are shown. Drying is from the top.

Similar to throats, ring saturation S_r exists in one of three states: Full ($S_r = 1$), partially filled ($0 < S_r < 1$) or empty ($S_r = 0$) (see Fig. 3.4). Full or partially-filled rings can have menisci when their neighboring throats are invaded by the gas phase. Maximum four menisci (which are represented by white arcs in Fig. 3.4) can form in these types of rings if all neighboring throats are emptied throats. Though menisci are assigned to full or partially-filled rings, they do not cause any pressure drop in the liquid phase. In other terms, rings provide extra path for liquid and vapor transport but, they do not take part in capillary pumping. This means only the presence of menisci in full or partially-filled throats can lead to pressure drop and eventually capillary pumping. Defining menisci in full or partially-filled rings is, though, important for cluster labeling and calculation of the local evaporation rate (see Secs. 3.3.2 and 3.3.3).

Throats and rings are conductors between pores. The state of a pore depends upon the state of its neighboring throats and rings. A pore is considered as liquid pore ($S_i = 1$) if all neighboring throats and rings are full, or at least partially filled. When a throat in the network empties, it leads to emptying of a pore. The pore becomes a gas pore ($S_i = 0$) and thus new menisci are generated in neighboring throats. A gas pore is either at the equilibrium vapor pressure (at least one of its neighboring elements is liquid) or at unknown vapor pressure (all neighboring elements are empty). All possible states of pore saturation are pictorially illustrated in Fig. 3.4.

On the basis of the saturation states of throats and rings, four mass transport zones are distinguished in the ring pore network. A liquid zone which consists of full, partially-filled throats and full rings. A film zone which is comprised of meniscus rings (which can be fully or partially filled) and empty rings neighboring non-diffusive throats. A dry zone which includes diffusive throats and their neighboring empty rings. A non-diffusive gas zone which is made of non-diffusive throats. The cumulative volume fraction of these zones remains constant and equal to one at any point in time during drying. Each zonal volume fraction is calculated by the volume of throats and rings in this zone divided by the total volume of throats and rings in the network. The liquid, non-diffusive gas, and dry zones are defined in the same way in the classical pore network model (CPNM), except that the saturation and volume of only throats are considered. The film zone is not defined, because the CPNM does not account for the ring effect. PNM simulations in relation with these zones are discussed in Chapter 4.

3.2.2 Cluster labeling

Liquid phase is initially considered as one cluster. As drying onsets menisci can develop in throats and rings and thus the liquid phase may split into clusters with different sizes. The identification of the meniscus throats and rings is important, because they are the candidates that can empty. To this purpose, all liquid throats and rings are given labels assigning them to one or the other cluster. Data structures of geometry and the saturation of throats and rings provide information required for cluster labeling.

The basic principle of classical cluster labeling is, if two throats are connected by a liquid pore, they belong to the same cluster (Metzger et al., 2007). The new principle of cluster labeling however is, if two throats are connected by a (full or partially filled) liquid ring, they belong to the same cluster. This means that the hydraulic connectivity in a liquid cluster is defined over both throats and rings together, thereby separate pumping networks of rings cannot exist in this algorithm. When cluster size is reduced to one meniscus throat and its neighboring rings, they are collectively termed as single cluster (Fig. 3.4). When all neighboring throats of a ring are emptied, the ring is called isolated/single ring (Fig. 3.4). Isolated rings act similarly to classical single throats, so they do not contribute to liquid connectivity and have potential to dry.

During each drying time step, typically one throat or isolated ring empties. Hence, variation in cluster labeling happens around this emptied element within the corresponding cluster. This cluster can break up into many clusters including single clusters. Therefore, the labeling procedure is confined to one corresponding cluster. The relabeling process begins from emptied throats.

As shown schematically in Fig. 3.5, key elements of the labeling algorithm are an empty throat E (white), children of this throat (blue) and children neighbors (gray). Terms such as children are used for the sake of consistency between the classical and new cluster labeling algorithms. The cluster labeling algorithm checks if the neighboring liquid throats of an emptied throat still belong to the same cluster. First, the old neighbor throats of neighbor rings of the emptied throat are labeled. These throats are called children. The children are labeled with the help of children neighbors by using a modified Hoshen-Kopelman algorithm (Metzger et al., 2006). Children neighbors are defined as liquid throats connected to children through their neighboring rings. When already labeled throats do not exist in the surroundings of a throat (in case of children labeling), a new cluster number is given to the throat. If already labels exist in the neighborhood (neighbor children), the throat gets minimum label (see Fig. 3.5). Based on this principle, two children throats get label 1 and the other two get label 2. The next generation of children

or children neighbors (gray) gets minimum label from the neighborhood instead of getting a new cluster label. They get label 1. These intermediate labels are revised based on the availability of minimum label in surrounding. After revision, all liquid throats get label 1. The labeling process will stop if all throats of the old cluster are relabeled or if all members of the new generation get the same label. The algorithm to generate the ring pore network labeling is summarized in Fig. 3.6 as a flow chart.

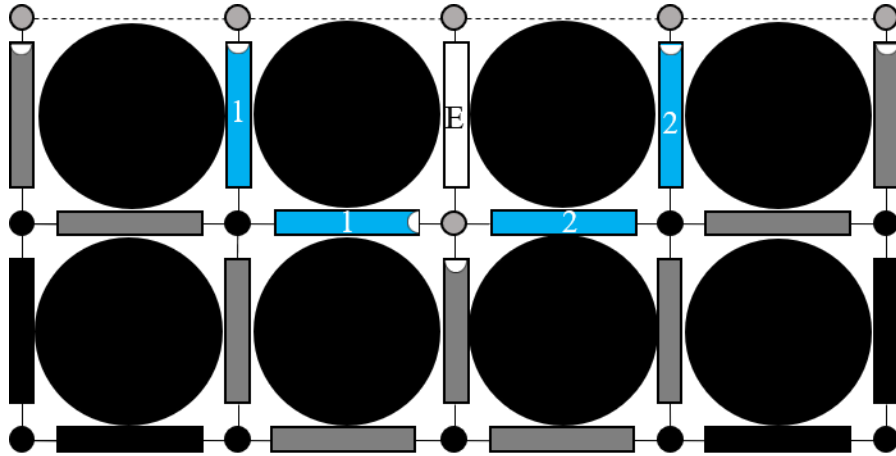


Fig. 3.5. Cluster labeling after emptying of throat E (blue throats: children, gray throats: children neighbors).

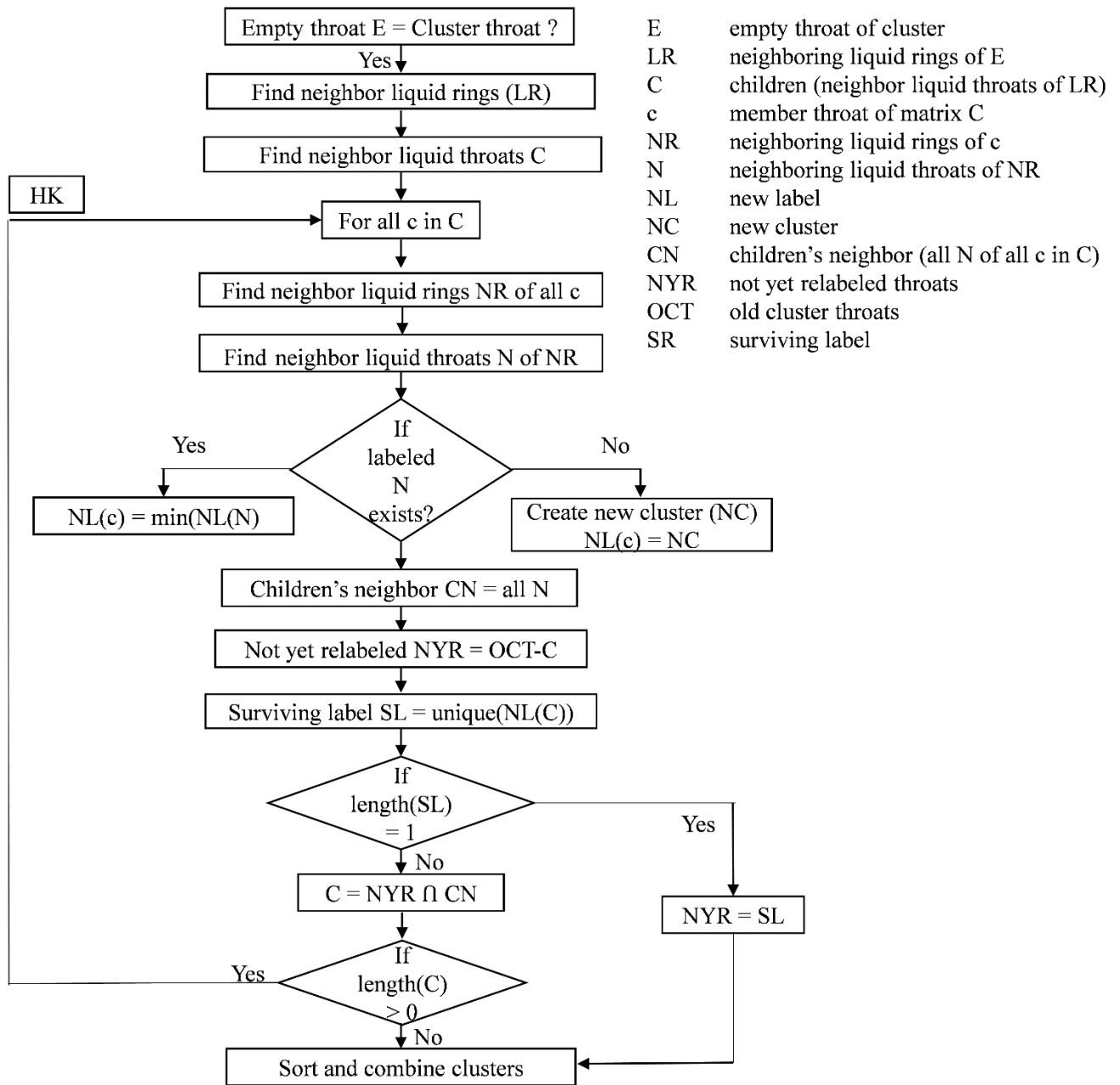


Fig. 3.6. Flowchart of ring pore network labeling algorithm.

3.2.3 Evaporation from throats and rings

The transport mechanisms in the network are described as follows: In full throats, capillary flow occurs due to difference in liquid pressure. In empty throats, vapor molecules diffuse due to difference in vapor pressure at neighboring gas pores. In partially-filled throats, liquid evaporation takes place at the menisci. In isolated rings,

liquid evaporation happens at the ring surface. In this work, capillary rings have identical volume and the liquid-gas interface of the ring is assumed to be flat. Vapor diffusion in the film and non-diffusive gas zones is suppressed since the vapor pressure is at the equilibrium vapor pressure. Additionally, the diffusive transport of the water vapor molecules in the boundary layer is taken into account.

Vapor transfer in the boundary layer and the dry zone within the network is modeled by vapor diffusion. Quasi-steady vapor flow rate between gas nodes i and j is described by

$$\sum_j \dot{M}_{v,ij} = \sum_j A_{ij} \frac{\delta}{L_{ij}} \frac{\tilde{M}_v P}{\tilde{R}T} \ln \left(\frac{P - P_{v,i}}{P - P_{v,j}} \right) \quad (3.6)$$

where A_{ij} is the exchange area (L^2 for boundary layer and πr_{ij}^2 for network), L_{ij} the distance between two nodes, $P_{v,i}$ the vapor pressure and $\dot{M}_{v,ij}$ the vapor mass flow rate, T the air temperature, \tilde{R} the universal gas constant, P the atmospheric pressure, δ the binary diffusion coefficient and \tilde{M}_v the molar mass of vapor. The boundary conditions for solving Eq. (3.6) are the vapor pressure of the dry air $P_{v,\infty}$ at the top nodes of the boundary layer and the saturated vapor pressure P_v^* at the gas pores of the network. Thus, vapor diffusion rates can be calculated for throats located in the dry zone. On this basis, evaporation rates of each cluster and isolated rings can be obtained. In this drying algorithm, only the liquid rings and throats that are direct neighbor of the evaporation front (gas nodes which provide diffusion) contribute to the overall evaporation rates according to their cross-section areas. The evaporation rate of neighbor meniscus throat k and neighbor liquid ring r of gas pore i are, respectively, computed by

$$\dot{M}_{ev,k,i} = \frac{A_k}{A_{total,i}} \sum_m \dot{M}_{v,m} \quad (3.7)$$

$$\dot{M}_{ev,r,i} = \frac{A_r}{A_{total,i}} \sum_m \dot{M}_{v,m} \quad (3.8)$$

where A_k is the cross section area of the meniscus throat k that is neighbor to pore i , A_r is the evaporating area of the liquid ring r that is neighbor to pore i , $A_{total,i} = \sum_k A_k + \sum_r A_r$ is the total area of all neighbor meniscus throats and neighbor liquid rings of pore i ,

$\sum_m \dot{M}_{v,m}$ is the total vapor flow rate away from the gas pore i through the neighboring empty throats m . Lateral area of a ring is calculated according to $2\pi rh$. Evaporating area A_r can be classified into three categories based on number of menisci: half, three quarters and full of lateral area when ring r has one, two or more than two menisci, respectively.

3.2.4 Network saturation

Since the amount of liquid in the throats and rings decreases after each drying time step, it is necessary to update the throat and ring saturations accordingly. At each time step, remaining liquid volume in the network is estimated by using throat saturation (S_{ij}) and ring saturation (S_r). If one meniscus throat or isolated ring is emptied in the drying step, the phase distribution and the boundary condition for the liquid phase are updated. The network saturation (S_n) is thus calculated as

$$S_n = \frac{\sum V_{ij} S_{ij} + \sum V_r S_r}{\sum V_{ij} + \sum V_r} , \quad (3.9)$$

where V_{ij} and V_r are the volumes of throat ij and ring r , respectively.

The overall drying algorithm is summarized in a flowchart shown in Fig. 3.7.

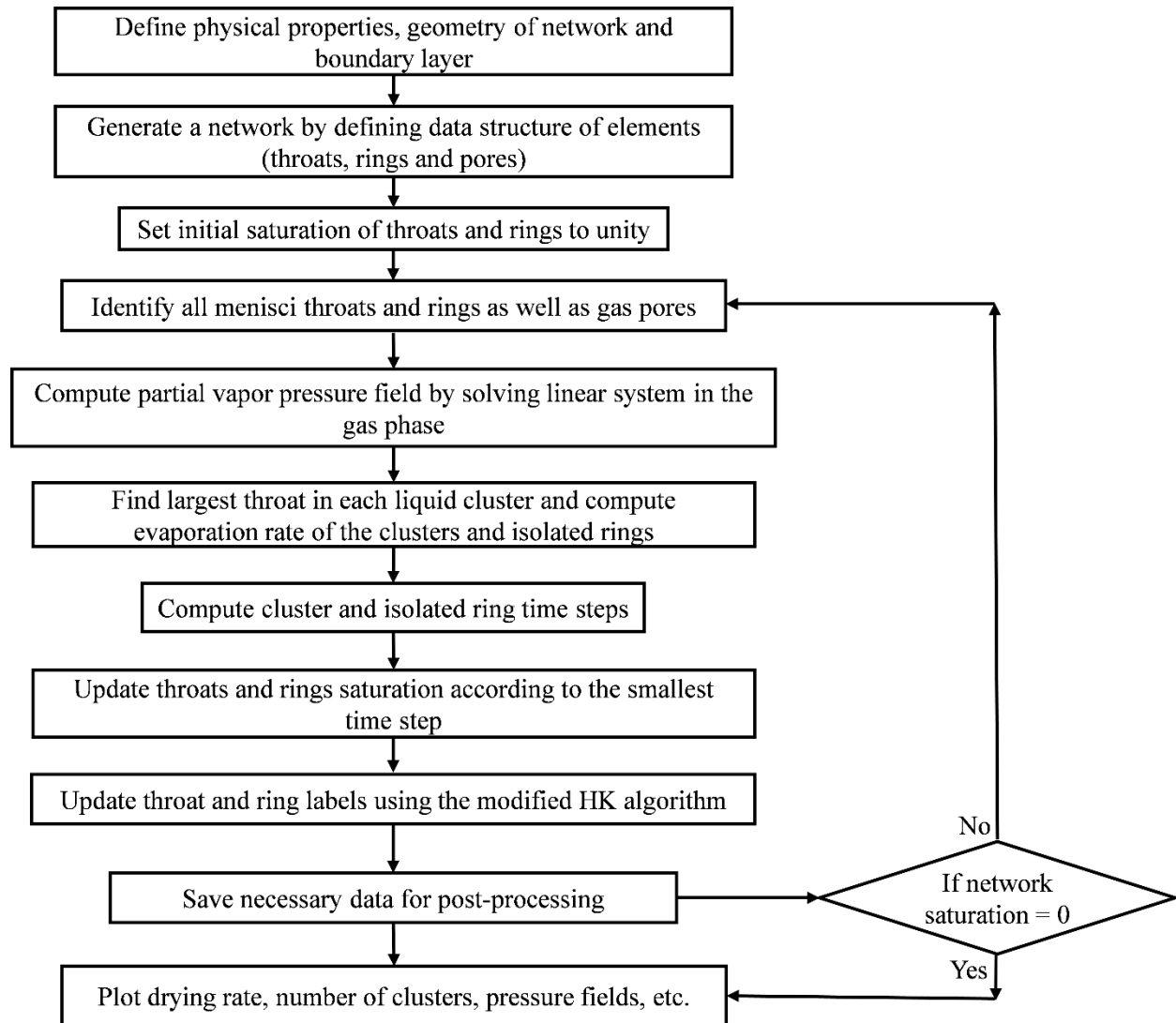


Fig. 3.7. Flowchart of the ring pore network drying algorithm.

Chapter 4

Part of this chapter has been published in “Kharaghani, A., Mahmood, H.T., Wang, Y.J., Tsotsas, E.: Three-dimensional visualization and modeling of liquid film rings observed during drying of random particle packings. *International Journal of Heat and Mass Transfer*, 177, 121505 (2021)”.

4 Evaluation of the ring pore network model

4.1 Model parameters

A cubic pore network with a size of $19 \times 18 \times 17$ is generated for both classical pore network model (CPNM) and ring pore network model (RPNM) simulations. The network size, the mass transfer coefficient and the thickness of the gas-side mass boundary layer are determined from the experimental data. The network size is determined based on the cross-sectional area and height of the container used for the particle packing drying experiments (see Sec. 2.1). The mass transfer coefficient is calculated from the air properties (i.e. mass density and moisture content) and the initial drying rate (evaporation flux) of the particle packing ($0.24 \text{ g/m}^2\text{s}$). The boundary layer with approximately 1.9 mm thickness is calculated from the binary diffusion coefficient ($25.7 \text{ mm}^2/\text{s}$) and the mass transfer coefficient (13.5 mm/s). The general geometry of both pore networks is constructed with a uniform throat length of $406 \text{ }\mu\text{m}$ and throat radius distribution of $84 \pm 1 \text{ }\mu\text{m}$ which results into volume distribution. In addition to throats,

capillary rings with a thickness of 51 μm , radius of 98 μm and filling angle of $\alpha = 29^\circ$ are generated in the RPNM. Though these rings occupy only 7.7% of the entire pore space volume approximated by throats and rings, their impact on drying is significant as shown later on. Characteristics of the particle packing and pore networks, which are worthy of comparison, are presented in Table 4.1.

Table 4.1. Characteristics of the particle packing and pore networks.

Parameter	Particle packing	Classical pore network	Ring pore network
Evaporative surface area (10^{-6} m^2)	50.3	50.4	50.4
Height (mm)	6.6	6.5	6.5
Initial volume of liquid water (10^{-7} m^3)	1.32	1.48	1.60
Porosity	0.40	0.45	0.49

4.2 Drying periods

Drying curves as well as average surface saturation as a function of network saturation are simulated using both CPNM and RPNM under identical initial and boundary conditions (Fig. 4.1). Both PNMs are able to predict the three periods of a classical drying curve. In the CPNM simulations, besides these periods, a short initial transition period is also observed which is characterized by a notable drop in the drying rate. This very first drop is essentially caused by a significant reduction in surface saturation (Fig. 4.1b). The surface saturation is defined as the average saturation of top vertical throats in CPNM and of both top vertical throats and rings in RPNM. It varies from unity (when the network surface is fully wet) to zero (when the network surface is dry).

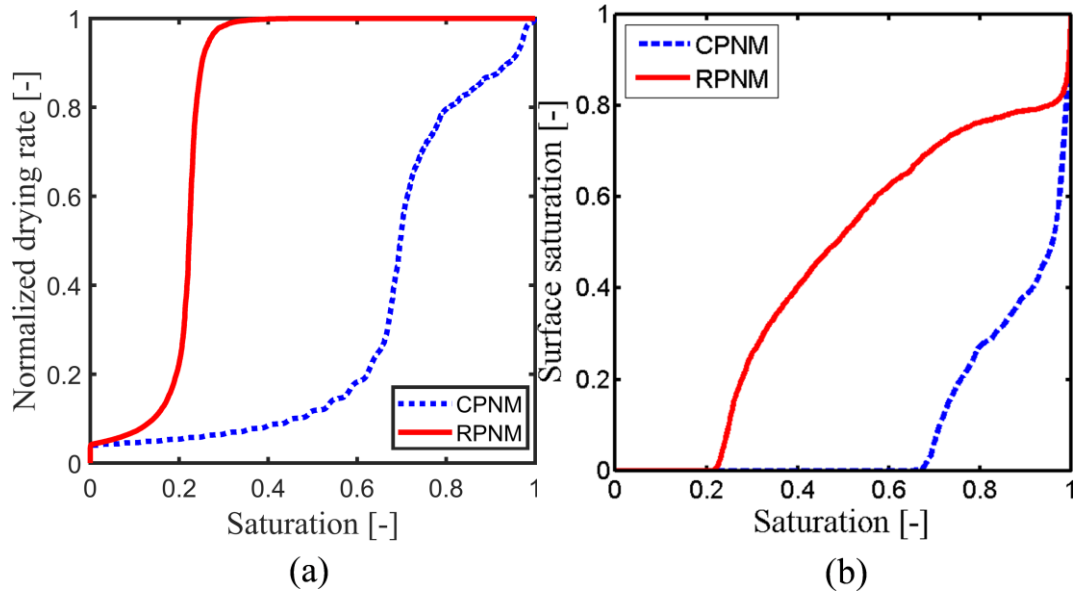


Fig. 4.1. (a) The average normalized drying rate and (b) the average surface saturation as a function of network saturation. The average curves are obtained considering 15 realizations.

According to the CPNM simulations, the surface saturation drops sharply from unity to about 0.5 (Fig. 4.1b). Abrupt removal of such huge amount of water perturbs the boundary conditions in terms of vapor field near the network surface in the following way. The surface pores are initially in contact with the liquid and have the saturated vapor pressure at drying air temperature. As drying proceeds, isolated single throats are created in the whole classical pore network, especially near the evaporative surface. The formation of these throats leads to more disconnection in the liquid phase during the transition period, as shown in Fig. 4.2a. The isolated single throats dry quickly and, as a consequence, the vapor partial pressure in the surface pores of the network drops and the drying rate decreases. Conversely, the initial transition period does not exist in the RPNM predictions. The reason can be understood in connection with the associated surface saturation profile shown in Fig. 4.1b. After the onset of drying the surface saturation drops, but not as significantly as in the CPNM. This is so because full connection of the liquid phase with the surface is maintained (Fig. 4.2a). During this time

span, evaporating liquid comes from inside of the network instead from the surface, thereby vapor pressure of the pores remains at the saturated vapor pressure.

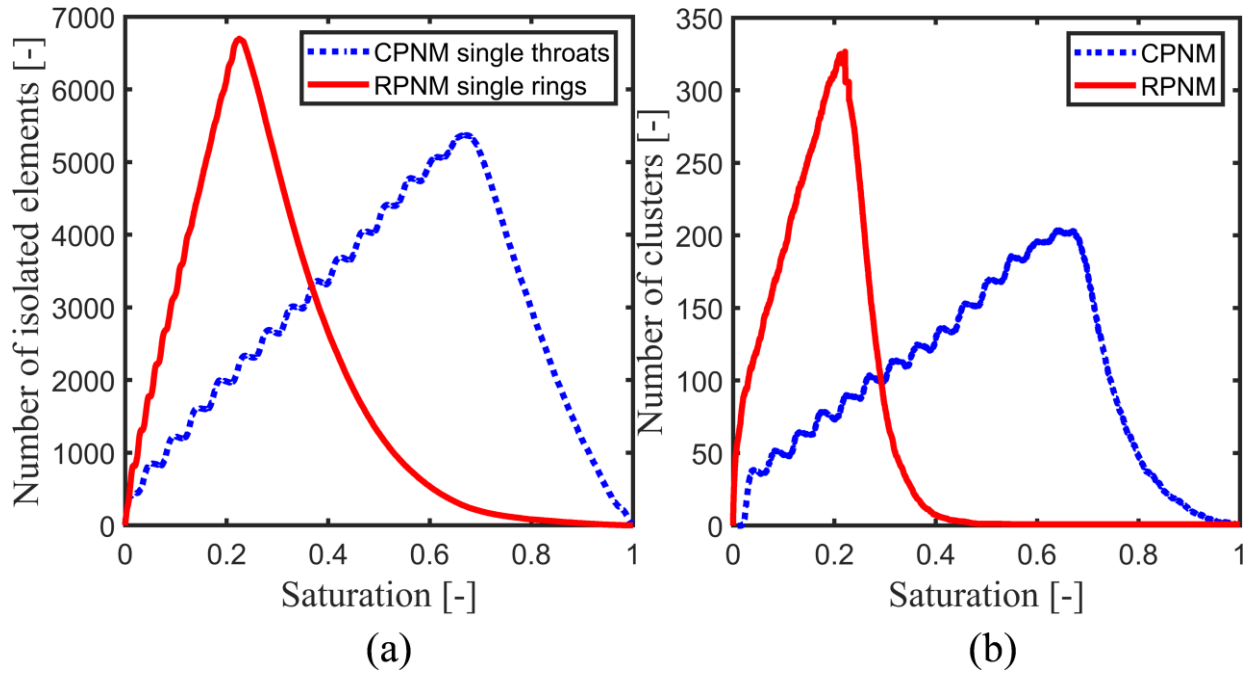


Fig. 4.2. (a) Number of isolated single throats and single rings and (b) total number of liquid clusters as a function of network saturation. The data are averaged over 15 realizations.

In the CPM the initial transition period is followed by CRP during which the surface saturation decreases slowly, and that is the reason why the drying rate is reduced only slightly. This kind of slight variation in drying rate is akin to that observed in early studies (Le Bray et al., 1999; Yiotis et al., 2006). During CRP of RPNM however, the drying rate remains constant, though the network empties significantly. The extension of CRP can be explained by late fragmentation of the liquid phase, which is visible from the evolution of the number of the clusters and isolated rings as shown in Fig. 4.2. More than half of the network liquid has evaporated when the first cluster splits. After that, the liquid phase is fragmented at higher rate, similarly to the experimental findings. As a result, the peaks of the number of clusters and isolated rings are high for the RPNM. When this fragmentation growth reaches a maximum, the capillary flow is not able anymore to

supply the liquid through a long distance to the network surface. This determines the duration of CRP and the beginning of FRP. In both PNM, the smooth decrease in surface saturation during the CRP becomes sharper during the FRP (see Fig. 4.1b). When the network surface dries, percolation of liquid from bottom to top ceases and, as a result, the evaporation front retreats from the surface to the interior of the network. At this time of drying the RFP commences. The FRP/RFP represents low drying rate with duration that is shorter by more than factor three if the ring effect is taken into account.

4.3 Evolution of fluid transport zones

In order to push this understanding forward, the transport zones forming in our pore networks during drying are characterized and shown in Fig. 4.3. One can refer to Sec. 3.2.1 for the definition of zones. As can be seen, notable differences between these two models is the existence of film zone and dramatic increase of non-diffusive gas zone in RPNM. In fact, the presence of film zone leads to enhancement of the non-diffusive gas zone which in turn extends the duration of CRP. The non-diffusive gas zone starts to dominate the liquid zone when half of the network liquid is evaporated in RPNM, while the non-diffusive gas zone never dominates the liquid zone during the whole process of drying in CPNM. In the RPNM the development of a dry zone is very much delayed. This delay postpones receding of the evaporation front. The onset of RFP corresponds to the domination of dry zone over non-diffusive gas zone in both models. Note that an obvious reason for the "ripples" observed in Fig. 4.3a is the finite size effect.

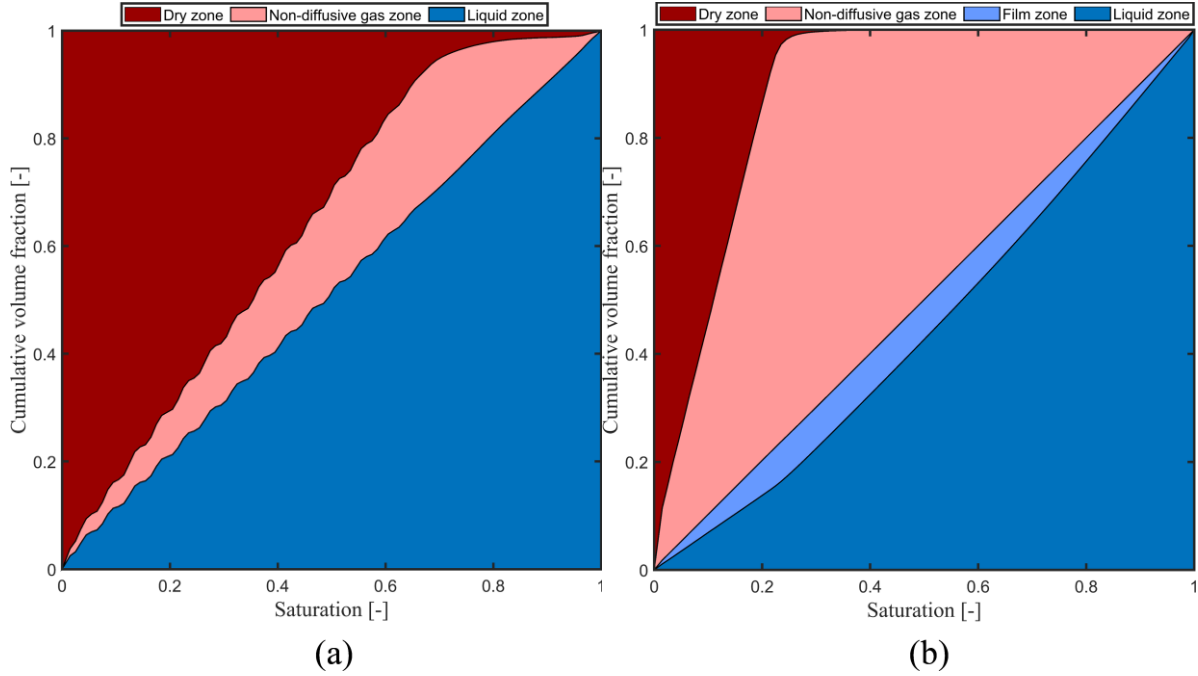


Fig. 4.3. Cumulative volume fractions of mass transport zones as a function of network saturation predicted by (a) CPNM and (b) RPNM. The data are averaged over 15 realizations.

4.4 Drying time

In earlier work (Vorhauer et al., 2015), it was found that both 2D classical and ring PNMs dramatically overpredict the drying time compared to experiments conducted using a quasi-two-dimensional micromodel made of solid blocks. It was additionally found that the drying time predicted by both PNMs is independent on the presence of liquid rings. This was partly explained by the late evaporation of the liquid films which were formed on the lateral walls of the micromodel during drying. In contrast to the previous study, the drying time is computed herein by 3D PNMs and the respective results are compared to the 3D measurement data. As can be seen in Fig. 4.4, the drying time predicted by the CPNM is about seven times longer than that determined from the measurement data. This factor however is reduced to about three in the RPNM simulations. This very significant reduction in drying time is attributed to the existence of liquid rings in the RPNM. As pointed out previously, liquid rings trapped at the contact between particles

provide connections for capillary flow and they thus pin the evaporation front on the network surface over a long time. These phenomena ensure the lateral vapor transfer in the boundary layer which, in turn, maintains drying at initial drying rate.

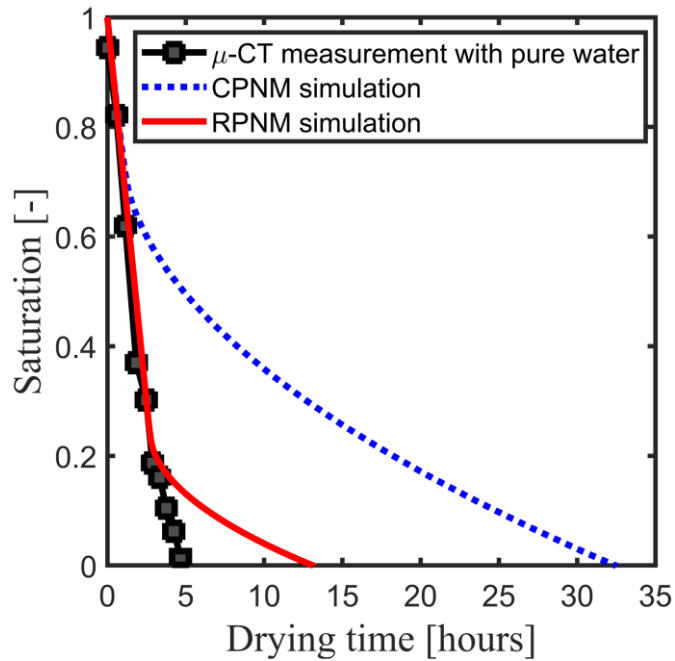


Fig. 4.4. Drying curves obtained from μ -CT measurement with pure water and both CPNM and RPNM simulations. The simulations are averaged over 15 realizations.

Though significant progress has been achieved in predicting accurately the drying time, some discrepancy exists which occurs more specifically at low saturations. This can be explained with the assumption made in the present RPNM, that is, if rings become disconnected, they do not communicate hydraulically. Because of this simplification, diffusion controls the evaporation rate during FRP and RFP in the RPNM while capillary flow may contribute to evaporation in the experiment down to low saturations in the packing (cf. Fig. 2.3). Moreover, other discrete events that may maintain liquid films stability are not taken into account in the present RPNM.

4.5 Saturation profiles

Successive slice-averaged saturation profiles obtained from the PNMs and X-ray measurement are shown in Fig. 4.5. For the sake of fair and direct comparison, profiles obtained from the PNM simulations and X-ray measurement are plotted at identical overall saturations. And, since number of slices in the PNMs are 16, 402 slices of experiment in Fig. 2.2b are averaged to 16 slices in Fig. 4.5c. Slices in the classical pore network contain one horizontal and one vertical plane of throats, while additional horizontal and vertical planes of rings exist in the ring pore network slices.

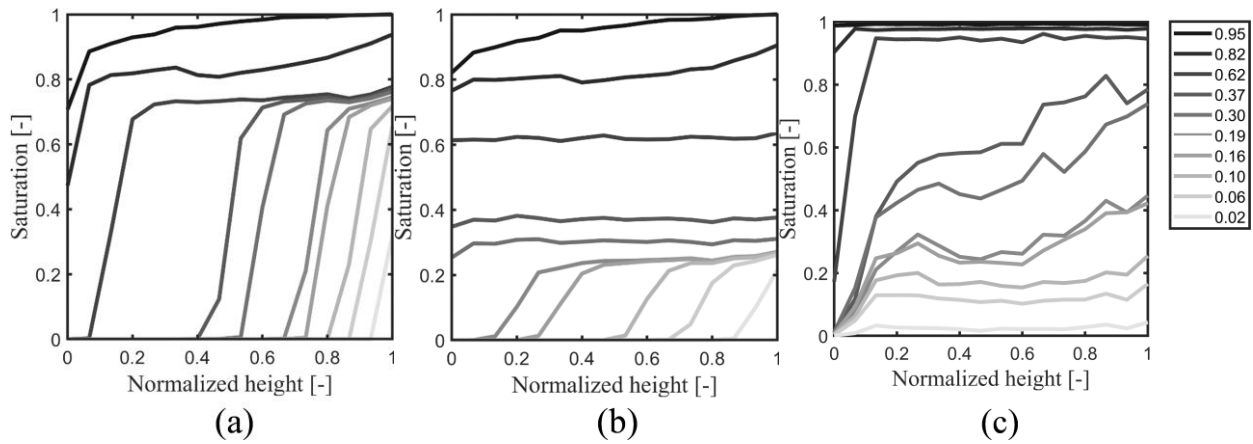


Fig. 4.5. Slice-averaged saturation profiles obtained from (a) CPNM simulations, (b) RPNM simulations and (c) experiment with pure water at network/packing saturations shown in legend. The network top surface is at 0. Results of 15 realizations are used for averaging.

Right from the beginning of the drying process a sharp drop in profiles of saturation can be seen in Fig. 4.5, similarly as in previous studies (Moghaddam et al., 2017; 2018). As mentioned earlier, this immediate drop occurs because small liquid clusters formed near the evaporative top side of the system are disconnected from the body of the liquid phase inside the system, and therefore they empty quickly, leading to a lower saturation near the top compared to deeper inside the system. Compared to CPNM simulations and μ -CT measurement, this drop, however, is significantly reduced in the RPNM simulations where saturation profiles become uniform over the liquid phase down to low network

saturation (Fig. 4.5b). This is in good agreement with the saturation profiles obtained experimentally from drying of kaolin samples (Faure et al., 2010).

Another striking difference that emerges from Fig. 4.5 is the irreducible saturation, i.e., the saturation for which the liquid phase is no longer connected over a distance comparable to the network height. An irreducible saturation of ≈ 0.22 is predicted by RPNM which is smaller than the ones simulated by CPNM (≈ 0.69) and reported models in literature (≈ 0.45) (Le Bray et al., 1999) (≈ 0.65) (Moghaddam et al., 2017), but it is closer to the experiments conducted with a random packing of monodisperse spherical particles (≈ 0.1) (Dullien et al., 1989) or fired clay brick (< 0.1) (Gupta et al., 2014). The lower irreducible saturation is indeed one factor that explains the longer CRP observed in the RPNM simulations compared to CPNM (cf. Fig. 4.4). When the point of irreducible saturation is reached, saturation of the bottom slice becomes constant down to very low overall network saturation.

4.6 Comparison with triangulation pore network model

Triangulation pore network model (TPNM) is irregular pore network model generated by regular Delaunay triangulation and its dual Voronoi tessellation (Pham, 2021). The TPNM simulates the drying behavior of capillary porous aggregates made of spherical primary particles. TPNM consists of two elements, pores and throats. Pores contain all volume, while throats are volumeless, as shown in Fig. 4.6 taken from Pham (2021). Comparative characteristics of TPNM simulations of Pham (2021) are surface area of 43.1 mm², network height of 6.4 mm, initial volume of liquid water of 144 mm³, and network porosity of 0.45. The corresponding values of throat radii and standard deviation used in TPNM are 111 μm and 70 μm , respectively (Pham, 2021).

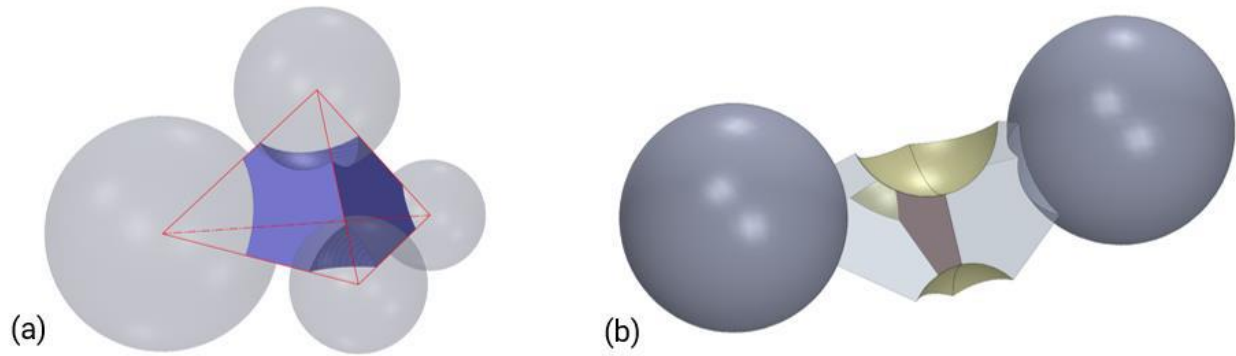


Fig. 4.6. (a) Pore (in blue) enclosed in a tetrahedral cell (red edges) among four neighboring spherical particles (transparent grey spheres). Parts of faces of the tetrahedron which are not occupied by the solid phase represent throats. (b) A throat (brown, truncated triangle) located at the common facet between two adjacent pores. The contact area between these common particles and the two pores is shown in gold. Solid particles which are not in common for these two pores are shown as gray spheres (Pham, 2021).

Pham (2021) compares findings of TPNM and RPNM in the context of μ -CT measurement with pure water in terms of drying curves and slice-averaged saturation profiles as recaptured/taken and shown in Figs. 4.7 and 4.8. Although the TPNM has a lower drying rate during CRP, however, the total drying time predicted by the model is still closer to the experimental measurement than the RPNM. The TPNM predictions of liquid phase distribution are in much better agreement with experimental results than those derived from RPNM simulations. The geometric properties of the pore network representing the void space of the porous medium, broad distributions of throat volume, and the form of boundary layer thickness have all been described as explanations for the difference between RPNM and TPNM. Further analysis, however, reveals that the discrepancy is due to differing input parameters for RPNM and TPNM, as detailed below.

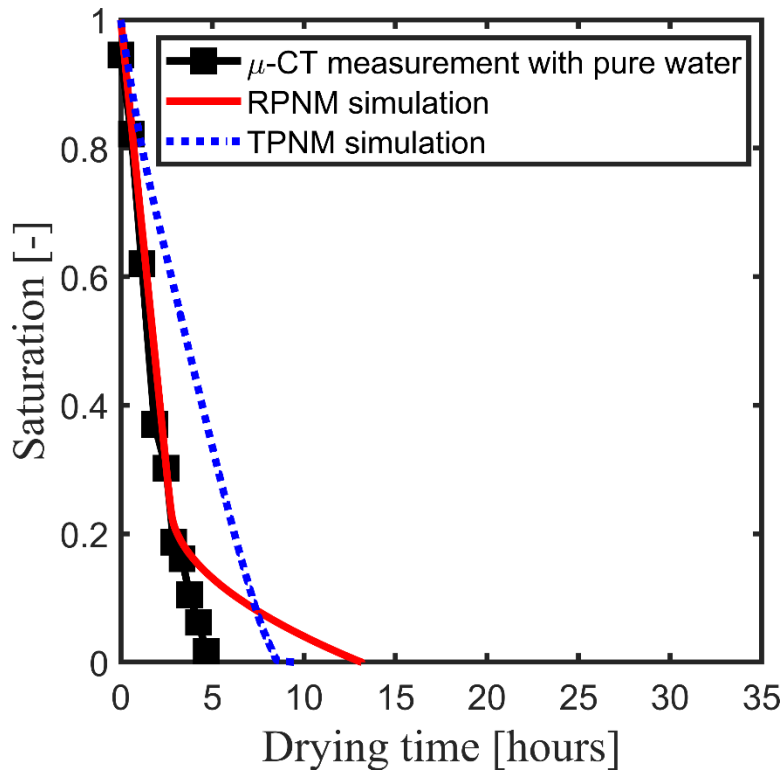


Fig. 4.7. Drying curves obtained from RPNM and TPNM simulations.

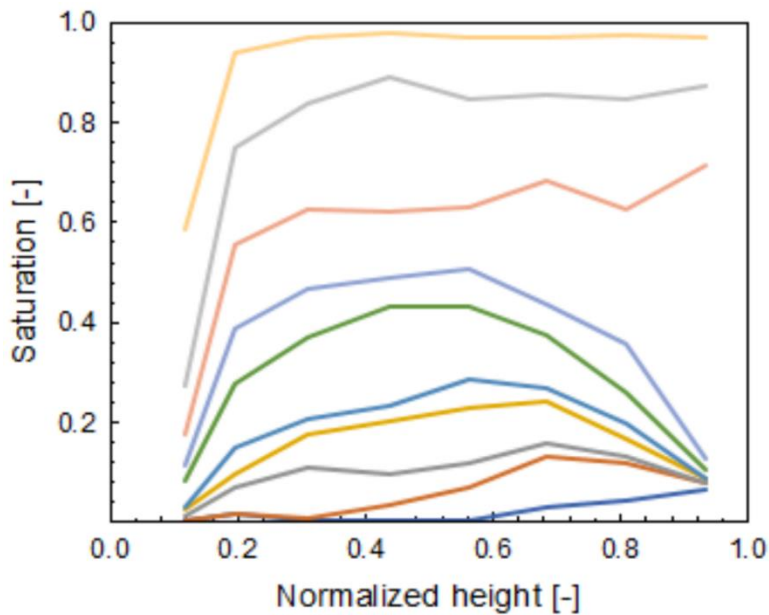


Fig. 4.8. Saturation profiles obtained from TPNM simulations. From top the profiles belong to network saturations of 0.95, 0.82, 0.62, 0.37, 0.30, 0.19, 0.16, 0.10, 0.06 and 0.02, respectively (Pham, 2021).

The critical analysis of divergent findings is presented here. The exact overall drying time predicted by TPNM and RPNM is 10.1 hours and 13.1 hours, respectively. The better prediction of overall drying time is partially due to overestimation of the liquid temperature as 26°C which results in an equilibrium vapor pressure of 3365 Pa. This temperature is assumed due to the temperature of drying air (26°C) in drying tunnel (see Fig. 2.1 and Sec. 2.2). The actual temperature of liquid is in between the temperature of drying air in drying tunnel (26°C) and the wet bulb temperature (17°C). Thus, we assume that the temperature of liquid to be 20°C because the liquid has also gained some amount of energy from the X-rays in the dryer setup which results in an equilibrium vapor pressure of 2339 Pa in Sec 4.1. To mimic temperature and equilibrium vapor pressure of TPNM, we ran RPNM simulation at 26°C. The variation of 6°C leads to an overall drying time of 9.5 hours (see comparison in Fig. 4.9).

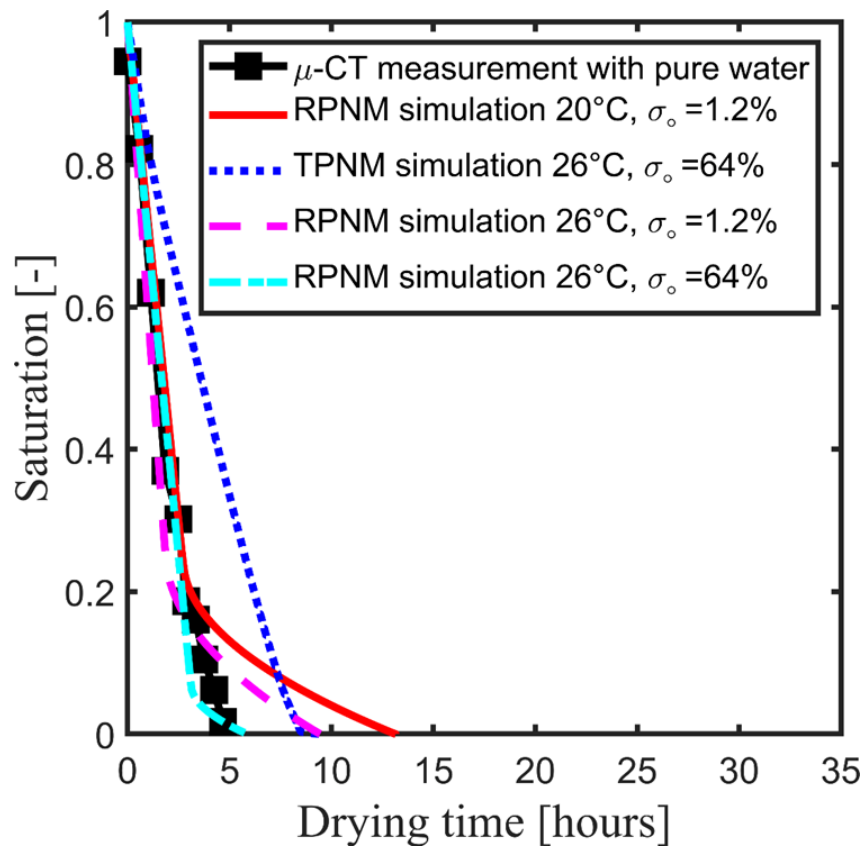


Fig. 4.9. Drying curves obtained from RPNM at three different conditions and TPNM simulations. Numerical results compared against the μ -CT experiment.

The other big factor for fast drying in TPNM is high value of standard deviation (σ_0) of throats which is 64% of the mean throat radius, while this σ_0 is 1.2% of mean throat radius in Sec. 4.1. The high value of standard deviation in TPNM increases CRP and the connectivity of the liquid phase to the top surface until 0.1 saturation, which results in fast drying. The impact of different standard deviations is discussed later in Sec. 5.2, but here a specific case of RPNM for the intended comparison is shown in Figs. 4.9 and 4.10 to mimic both temperature (26°C) and standard deviation (64%) of TPNM. The porosity of the network increases to 0.67, that means initial volume of liquid water of 221 mm³. As can be seen, CRP is extended down to 0.07 saturation of the network and the overall drying time is reduced to 5.9 hours that is much faster than predicted by TPNM and closer to the overall drying time (4.67 hours) of experiment with pure water. It is also worth noting that the RPNM contains 53% additional amount of liquid than TPNM.

The author's (Pham, 2021) second critical analysis regarding RPNM about the spatial phase distribution as shown in Fig. 4.5b is reproduced here as follows:

“there is no place in the network having saturation higher than 0.4 at network saturation of 0.37 according to the RPNM simulation, and there is no liquid remaining in the region higher than a relative network height of 0.4 at the network saturation of 0.10.”

The spatial phase distribution of RPNM for this specific case is shown Fig. 4.10 which addresses above mentioned criticism about the spatial phase distribution (compare Fig. 4.10 with Fig. 4.8). The saturation profiles obtained from RPNM simulation with 64% standard deviation of mean throat radius at 26°C better predict experimental saturation profiles than TPNM (compare Fig. 4.10 and Fig. 4.8 with Fig. 4.5c). A detailed analysis of liquid disintegration of TPNM in terms of number of clusters and isolated elements is not available for comparison, except of the main liquid cluster.

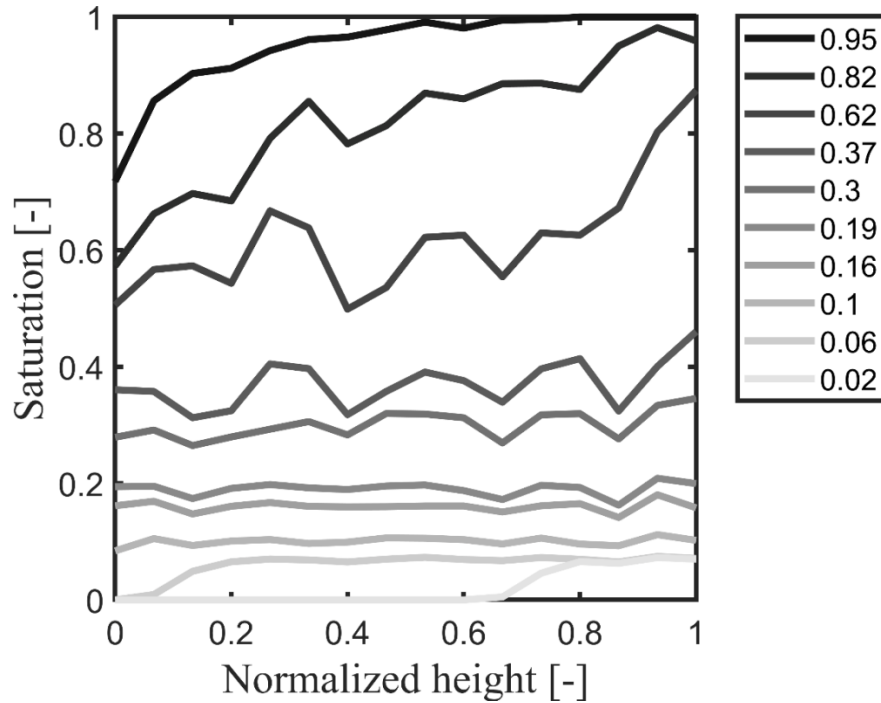


Fig. 4.10. Saturation profiles obtained from RPNM simulation with 64% standard deviation of mean throat radius at 26°C. From top the profiles belong to network saturations of 0.95, 0.82, 0.62, 0.37, 0.30, 0.19, 0.16, 0.10, 0.06 and 0.02, respectively.

Compare to RPNM, the TPNM has better capability to capture wall effect because of its irregular nature and its ability to create larger pores near the walls. Water from the larger pores will evaporate preferentially when it comes into contact with the gas phase, as can be seen in Fig. 4.8. But this effect also decreases in TPNM when standard deviation is lower than 50% (see Table 4.9 and Fig. 4.9 in Pham, 2021).

Chapter 5

5 Parametric study

In this chapter, parametric study is performed to understand the versatility and sensitivity of RPNM. Three parameters: ring volume, distribution of throat radius and boundary layer thickness are studied upon their impact. In this chapter, RPNM is employed as introduced in Chapter 3 to investigate the influence of these parameters on the drying kinetics and liquid phase distribution discussed in Chapter 4. All results are averaged over 3 realizations in this chapter. Basic characteristics of the pore networks used for drying simulations are mentioned in Tables 5.1, 5.2 and 5.3.

5.1 Variation of size of throats and rings

Three scenarios are discussed with two extreme conditions and a medium condition. The two extreme cases contain minimum and maximum amount of liquid in secondary capillary structure. The ring size is varied by varying the half-filling angle α . The radius of throat is calculated according to Eq. 2.2.

- **Case 1:** $\alpha = 14^\circ$ generates capillary rings with a thickness of $12 \mu\text{m}$ and radius of $50.6 \mu\text{m}$. The mean throat radius is $84 \mu\text{m}$ similar to Chapter 4 to avoid overlap with solid particles. The standard deviation of throat radius is 10% of mean throat radius. Throats and rings contain 99.4% and 0.6% of total liquid in the network, respectively.

- **Case 2:** $\alpha = 30.4^\circ$ generates capillary rings with a thickness of 55.7 μm and radius of 103 μm . The mean throat radius is 84 μm . The standard deviation of throat radius is 10% of mean throat radius. Throats and rings contain 91% and 9% of total liquid in the network, respectively.
- **Case 3:** $\alpha = 44^\circ$ generates capillary rings with a thickness of 114 μm and radius of 196 μm . The mean throat radius decreases to 7 μm correspondingly. The standard deviation of throat radius is 10% of mean throat radius. Throats and rings contain 0.6% and 99.4% of total liquid in the network, respectively.

Table 5.1. Characteristics of the pore networks used for drying simulations.

Parameter	Case 1	Case 2	Case 3
	$\alpha = 14^\circ$	$\alpha = 30.4^\circ$	$\alpha = 44^\circ$
Network size	19×18×17	19×18×17	19×18×17
Boundary layer size	19×18×5	19×18×5	19×18×5
Throat length (μm)	406	406	406
Mean throat radius (μm)	84	84	7
Standard deviation of throat radius (μm)	8.4	8.4	0.7
Initial volume of liquid water (10^{-7} m^3)	1.50	1.64	1.65
Network porosity	0.46	0.50	0.50

The drying rate is normalized over the initial drying rate of the same case in Fig. 5.1a. The initial evaporation rate depends on the boundary layer thickness. The boundary layer is the same in all three cases therefore, the same initial evaporation rate is observed. However, the change in the ring volume affects the duration of the faster drying period.

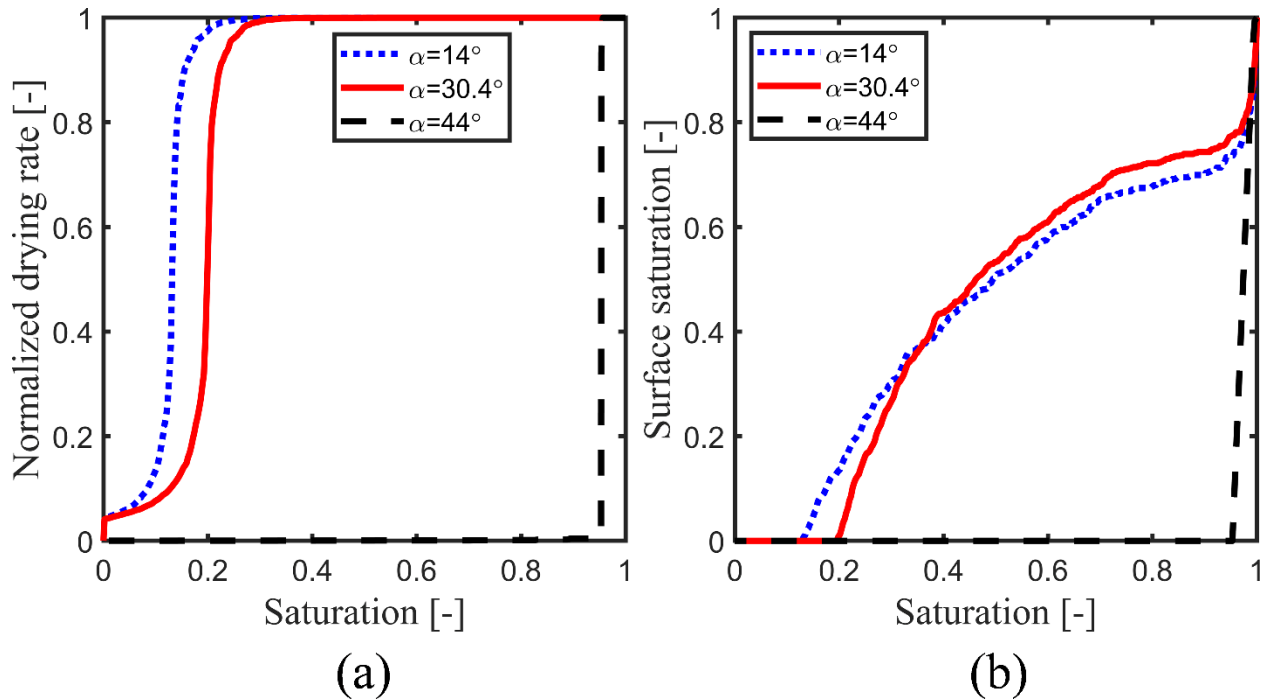


Fig. 5.1. (a) The average normalized drying rate and (b) the average surface saturation as a function of network saturation for different values of half-filling angle α . The average curves are obtained considering 3 realizations.

The longer CRP is observed in the case with the smaller ring volume and duration of CRP decreases with the increase in ring volume. Case 2 is reference case in this section and similar to the previous case from Chapter 4, with only difference the angle of 30.4° instead of 29° . The calculated angle value was 30.4° but 29° was used to avoid overlap of throats and rings in Chapter 4. The other purpose of medium condition (case 2) is also to see the impact of 1.4° differential which was neglected in previous chapter. Case 1 and case 3 are opposite in terms of volume of throats and rings, so that their drying kinetics are interesting to observe. The overall trend of CRP, FRP and RFP in Case 1 is similar to reference case 2 as shown in Figs. 5.1 to 5.6. The decrease in volume of rings increases CRP and decreases RFP. The evolution of drying periods is supported by evolution of surface saturation which controls CRP (see Fig. 5.1b). The initial drop in surface saturation is slightly higher but overall duration is slightly longer. On the contrary, case 3 shows dramatic changes with respect to reference case 2. The CRP is reduced to a small

duration with sudden huge drop in surface saturation as shown in Fig. 5.1. The CRP/FRP transition is sharper and drying rate drops to very low value.

To analyze the impact of these changes on drying kinetics, the average vapor pressure in the network including boundary layer and profiles of horizontal layer-averaged vapor pressure including boundary layer as a function of network saturation for three half-filling angles are computed as shown in Figs. 5.2 and 5.3. Total number of horizontal layers are 21 and each horizontal plane consists of 19×18 number of pores. Out of 21 layers, 17 belong to the network. In Fig. 5.3, 0 to 0.19 normalized height depicts the boundary layer thickness. For the sake of direct comparison, profiles obtained from the PNM simulations for all three cases are plotted at identical overall saturations 0.99, 0.9, 0.8, 0.7, 0.6, 0.5, 0.4, 0.3, 0.2 and 0.1 in Fig. 5.3. Figures 5.3a and 5.3b show only three profiles, because other profiles are overlapping existing profiles. The overall vapor pressure field trend of those three cases explains CRP, FRP and RFP in Fig. 5.2. As long as surface remains wet, the surface pores stay at the equilibrium vapor pressure and the higher average vapor pressure is observed. The higher vapor pressure leads to higher evaporation rate.

Right from the beginning of the drying process a sharp drop in profiles of horizontal layer-averaged vapor pressure can be seen in Fig. 5.3. This immediate drop occurs due to boundary layer and its contact to bulk air. After that, compared to reference case (Fig. 5.3b), case 1 (Fig. 5.3a) shows lower drop in averaged vapor pressure of horizontal layers near the surface of the network at lower network saturations. Figure 5.3c shows an increase in resistance for vapor transport deep in the network at higher saturation by increasing volume of liquid in rings and decreasing volume of liquid in throats.

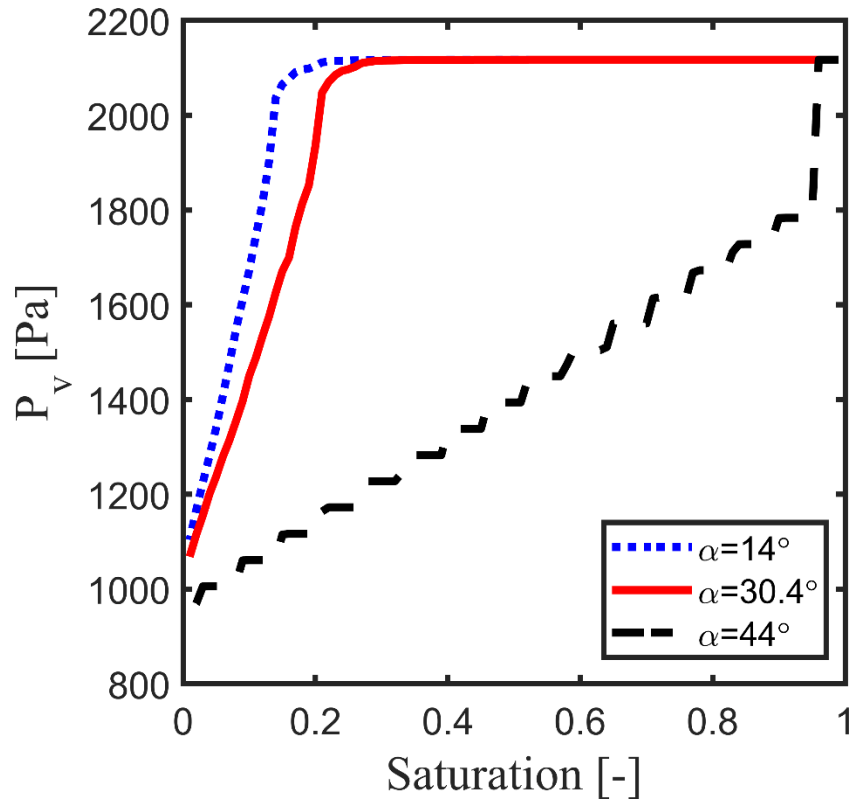


Figure 5.2. Average vapor pressure in the network including boundary layer as a function of network saturation for different values of half-filling angle α .

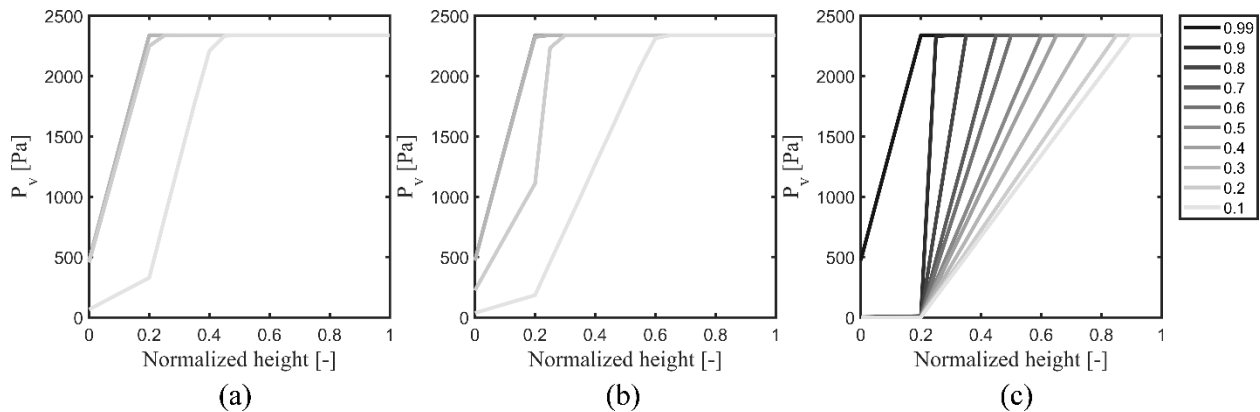


Figure 5.3. Profiles of horizontal layer-averaged vapor pressure in the network including boundary layer for: (a) $\alpha = 14^\circ$ (b) $\alpha = 30.4^\circ$ and (c) $\alpha = 44^\circ$. The network top surface is at 0 and bottom of the network is at 1; (a and b show only three profiles because other profiles are overlapping).

The change in the kinetics can also be analyzed by looking into the liquid connectivity during drying. An irreducible saturation of ≈ 0.13 is predicted at $\alpha = 14^\circ$, which is smaller than the one simulated at $\alpha = 30.4^\circ$ (≈ 0.20). The irreducible saturation predicted at $\alpha = 44^\circ$ is dramatically high (≈ 0.99). The fragmentation of the liquid phase starts at different network saturation. The late fragmentation of the liquid phase in cases 1 and 2 is visible from the evolution of the number of liquid clusters and isolated rings as shown in Fig. 5.4. As can be seen, the whole liquid phase belongs to the single main cluster until low network saturation. In case 3, right from the beginning, liquid phase becomes highly disintegrated as can be seen by the peak in the number of clusters and single rings, which results in slow drying.

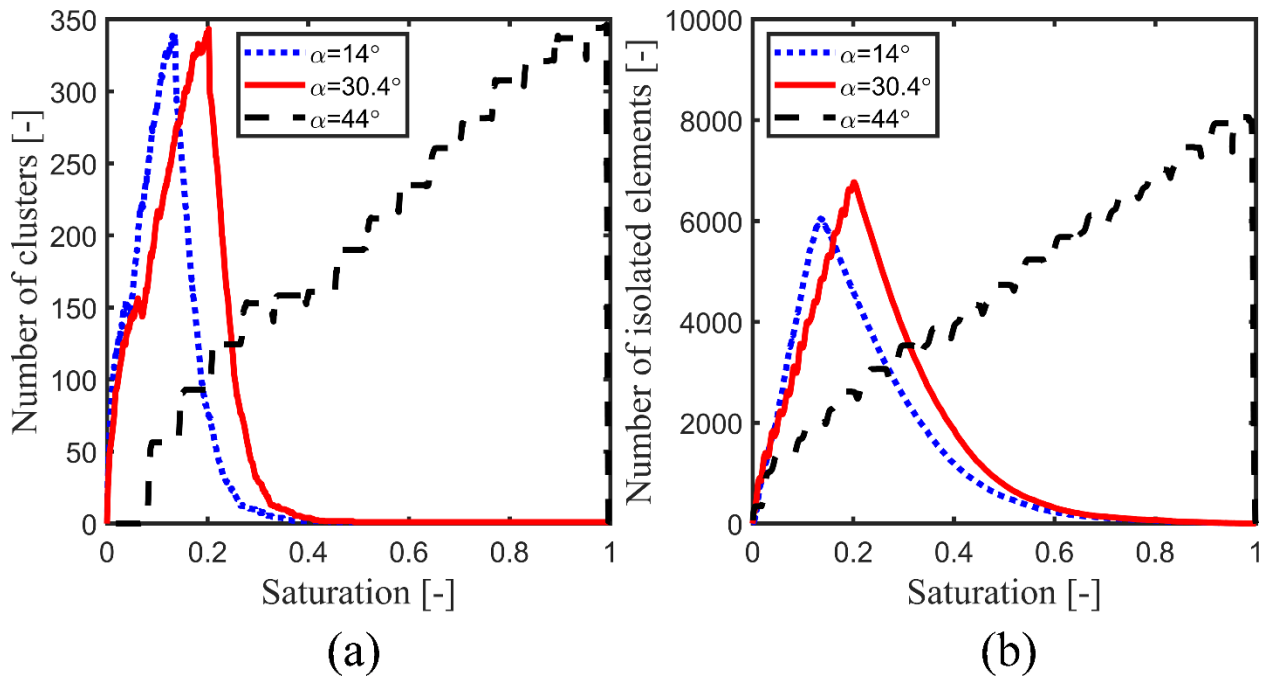


Figure 5.4. (a) Total number of liquid clusters and (b) number of isolated single rings as a function of network saturation for different values of half-filling angle α .

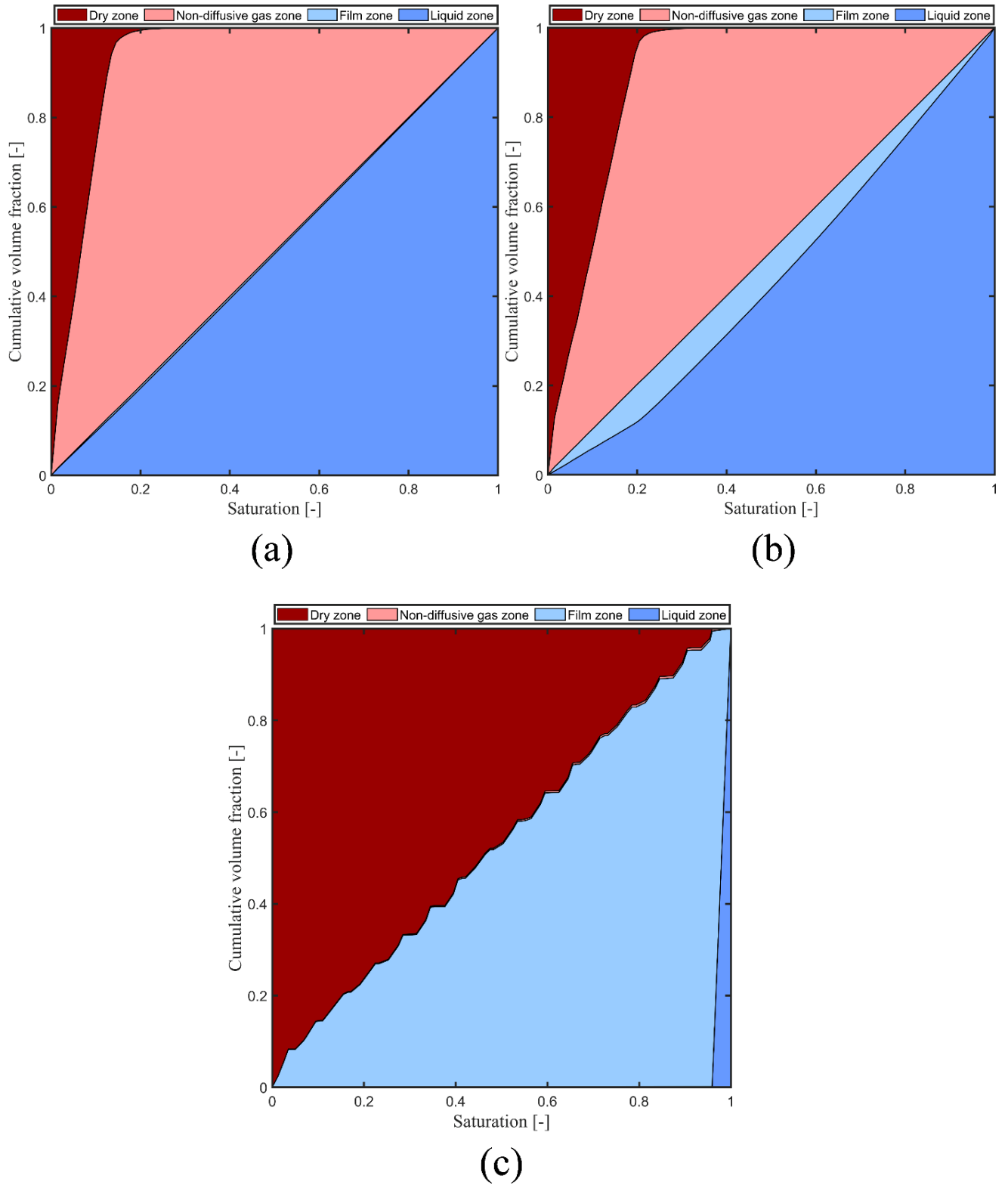


Figure 5.5. Cumulative volume fractions of mass transport zones as a function of network saturation predicted by RPNM (a) $\alpha = 14^\circ$ (b) $\alpha = 30.4^\circ$ and (c) $\alpha = 44^\circ$.

The impact of variation of size of both elements, especially rings, is visualized by means of transport zones in Fig. 5.5. Notable differences between these three cases is the dramatic increase of film zone and decrease of non-diffusive gas zone in case 3 with respect to reference case. In first two cases (Fig. 5.5a and Fig. 5.5b), the development of a dry zone is delayed, which postpones CRP/FRP transition. In case 3, from the beginning, dry zone dominates the non-diffusive gas zone, which triggers the onset of RFP.

Drying curves for the three cases are compared in Fig. 5.6. As can be seen, the drying time predicted for $\alpha = 14^\circ$ and $\alpha = 44^\circ$ are 0.7 times and 497 times longer than that determined for the reference case. The difference between reference case and previous case from Chapter 4 is negligible.

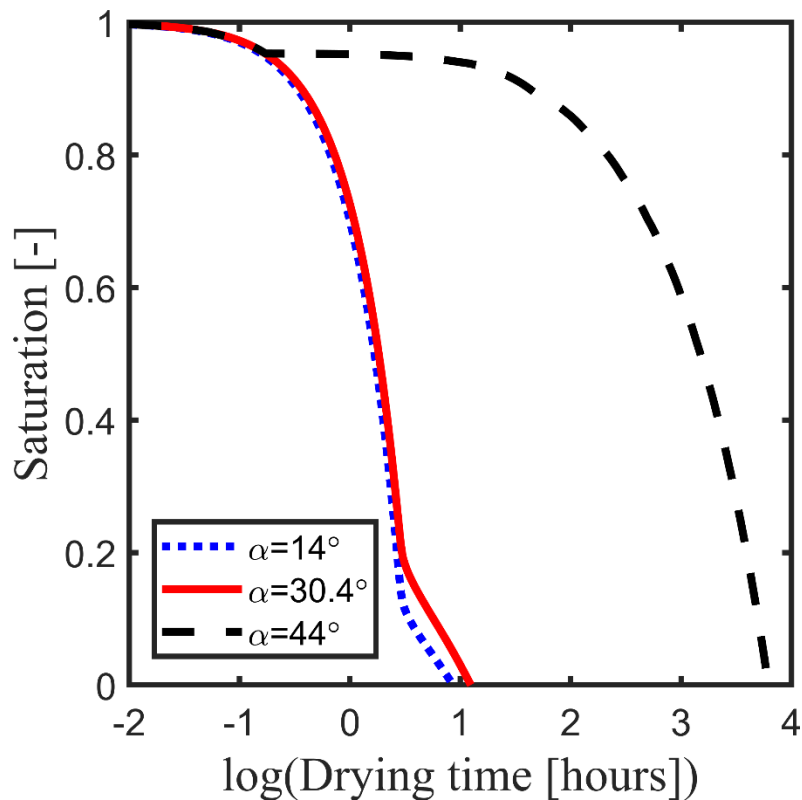


Figure 5.6. Drying curves obtained from RPNM simulations for different values of half-filling angle α .

5.2 Variation of throat radius distribution

Three scenarios are discussed with two extreme conditions and one medium condition for CPNM and RPNM. The throat radius is distributed in the network by normal random distribution. Table 5.2 shows the characteristics of drying simulations for three networks of CPNM and RPNM with three different values of the standard deviation of throat radius (10%, 50% and 100% standard deviation of mean throat radius), which results in porosity change. The liquid transfer depends upon the discrepancy between the radii of hydraulically connected menisci. The change in standard deviation of throat radius leads to change in the duration of CRP.

Figs. 5.7 and 5.8 shows longer CRP and faster drying with increase in the value of standard deviation of throat radius, but the extent of impact is different in CPNM and RPNM. The initial transition period is reduced with an increase in standard deviation despite of larger drop in surface saturation as shown in Fig. 5.9. Similarly, abrupt removal of liquid at surface also occurs in RPNM, but it does not generate an initial transition period. However, the increase in standard deviation increases the duration of surface saturation in both models. The CPNM produces almost double duration of CRP from one extreme case 4 to another extreme case 6. The CRP of RPNM changes significantly from case 7 to case 8, in comparison to very small change from case 8 to 9.

To understand this phenomenon, we investigated the evolution of liquid phase in Figs. 5.10, 5.11 and 5.12. Duration of liquid belonging to one big cluster increases, which ensures transport of liquid towards surface. This spatial connectivity supplies water to provide the evaporative demand. The initial disintegration of liquid phase is delayed in both models. However, disintegration rate during the end of CRP is different, as shown in Figs. 5.10 and 5.11. The disintegration rate of CPNM is decreasing with increase of standard deviation and peak number of clusters and single throats is also declining. While in RPNM, the late disintegration rate and peak number of clusters and single rings

Table 5.2. Characteristics of the pore networks used for drying simulations.

Parameter	CPNM			RPNM		
	Case 4 $\sigma_0 = 10\%$	Case 5 $\sigma_0 = 50\%$	Case 6 $\sigma_0 = 100\%$	Case 7 $\sigma_0 = 10\%$	Case 8 $\sigma_0 = 50\%$	Case 9 $\sigma_0 = 100\%$
Network size	19×18×17	19×18×17	19×18×17	19×18×17	19×18×17	19×18×17
Boundary layer size	19×18×5	19×18×5	19×18×5	19×18×5	19×18×5	19×18×5
Throat length (μm)	406	406	406	406	406	406
Mean throat radius (μm)	84	84	84	84	84	84
Standard deviation of throat radius (μm)	8.4	42	84	8.4	42	84
Initial volume of liquid water (10 ⁻⁷ m ³)	1.50	1.85	2.95	1.62	1.97	3.1
Network porosity	0.46	0.56	0.90	0.49	0.60	0.94

is rising. This change in liquid phase distribution is also reflected in the transport zones of both models. The role of non-diffusive gas zone in CPNM increases with increasing standard deviation of throat size distribution, as shown on the left side of Fig. 12. The relative decrease in film zone on the right side of Fig. 12 is due to the increase in the volume of throats. The increase in the duration of CRP is reflected in the by evolution of film and non-diffusive gas zone.

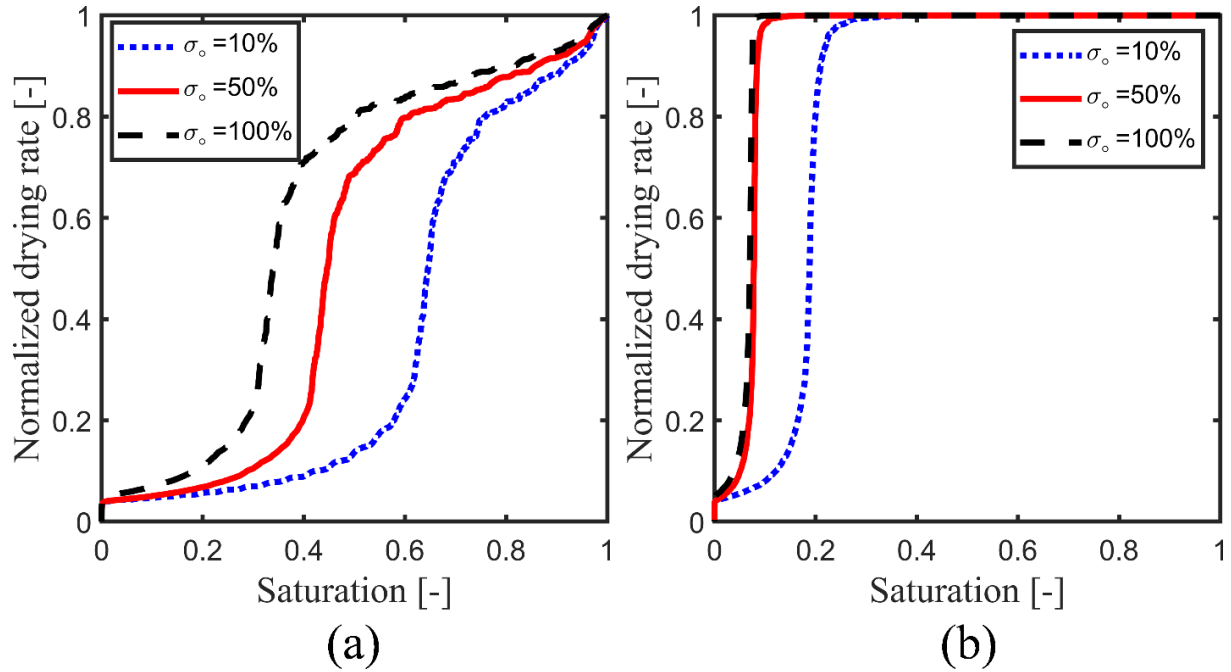


Fig. 5.7. The average normalized drying rate as a function of network saturation predicted by (a) CPNM and (b) RPNM for different values of standard deviation σ_0 . The average curves are obtained considering 3 realizations.

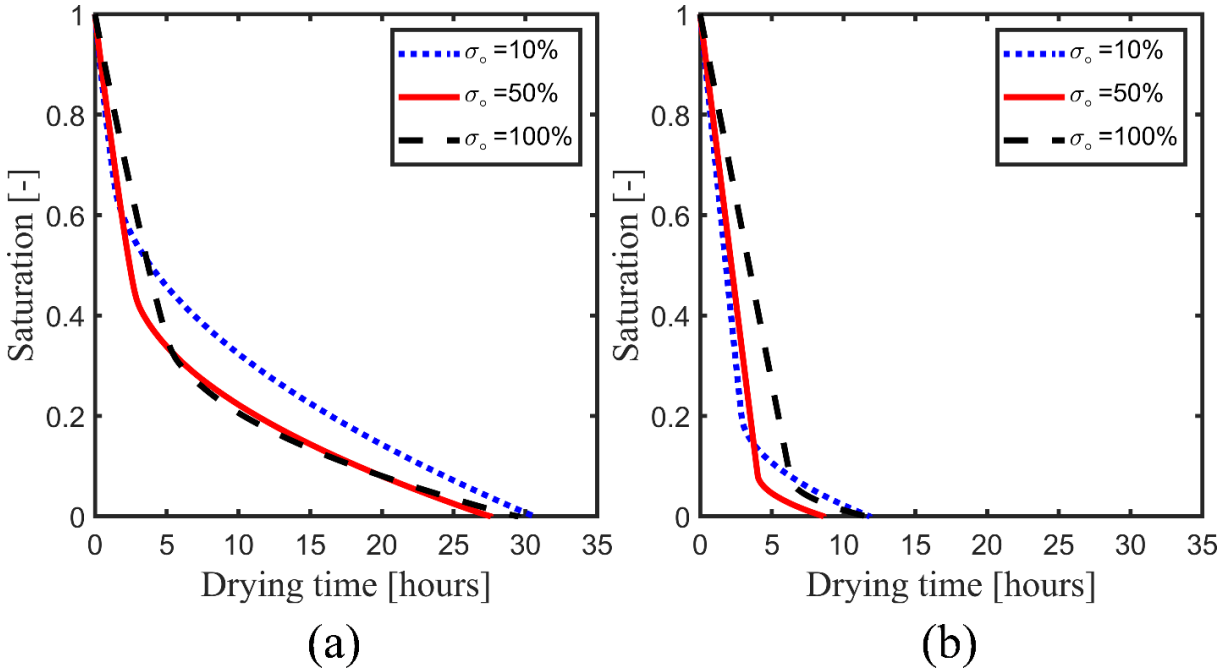


Figure 5.8. Drying curves obtained from (a) CPNM and (b) RPNM for different values of standard deviation σ_0 .

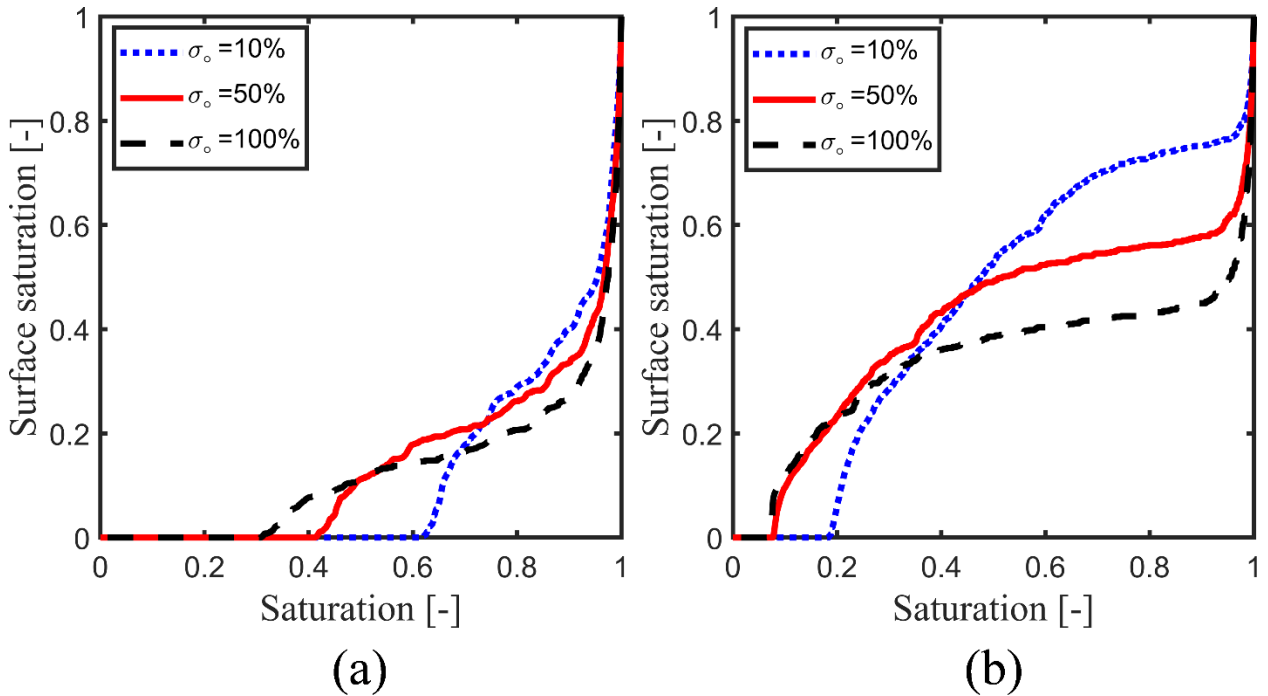


Fig. 5.9. The average surface saturation as a function of network saturation predicted by (a) CPNM and (b) RPNM for different values of standard deviation σ_0 .

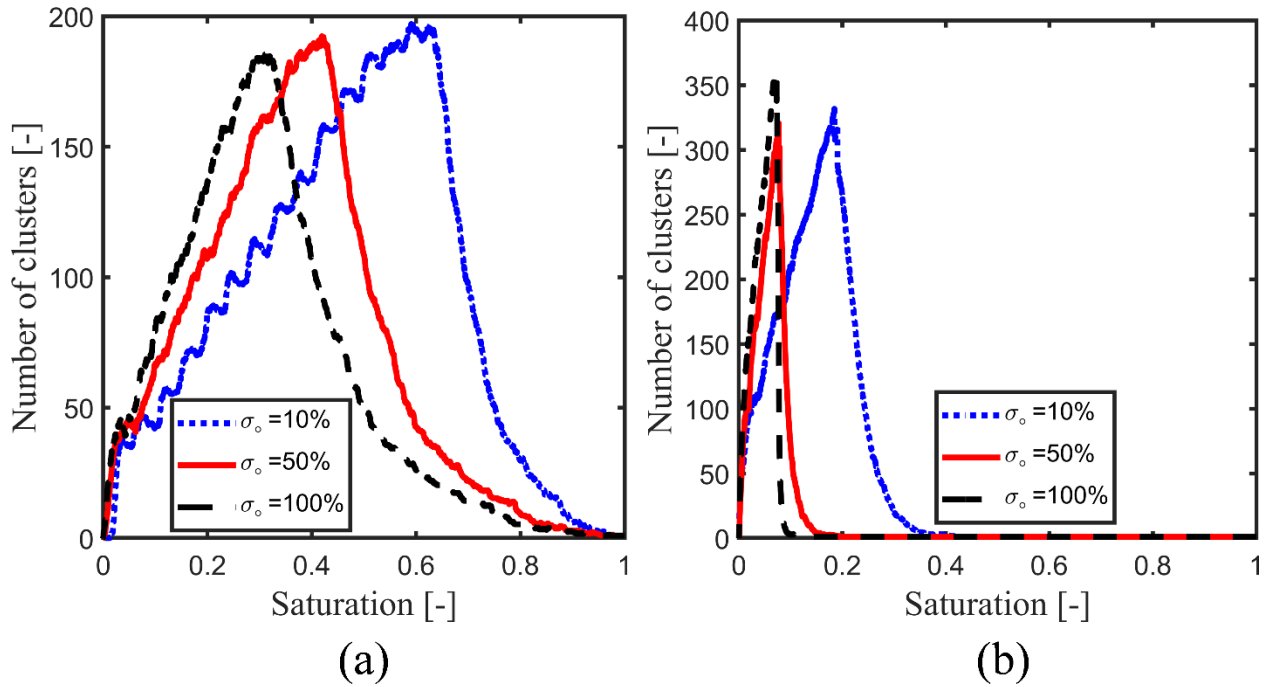


Figure 5.10. Number of clusters as a function of network saturation by (a) CPNM and (b) RPNM for different values of standard deviation σ_o .

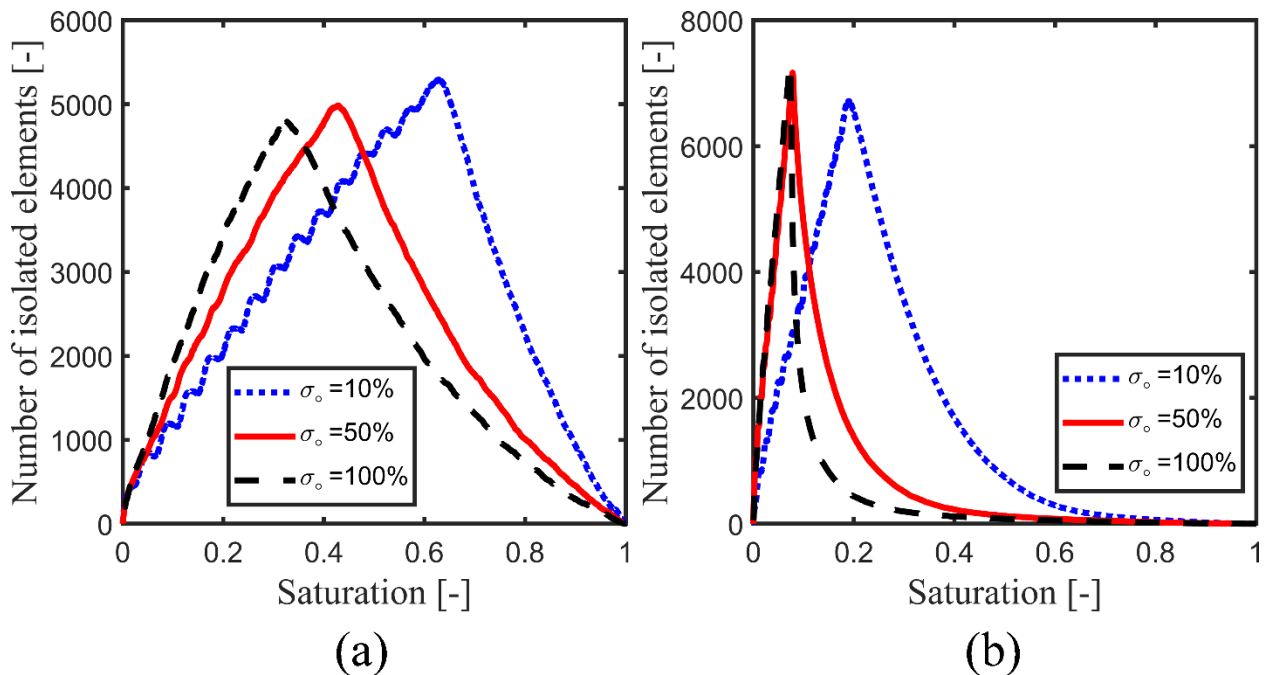
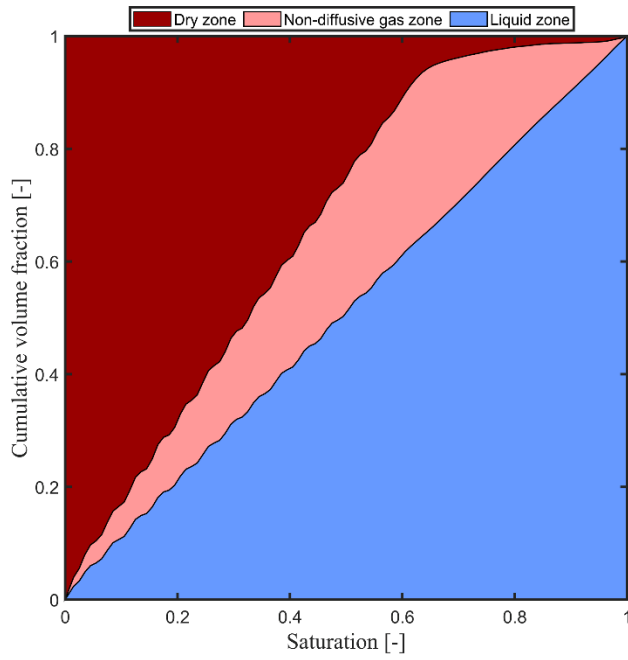
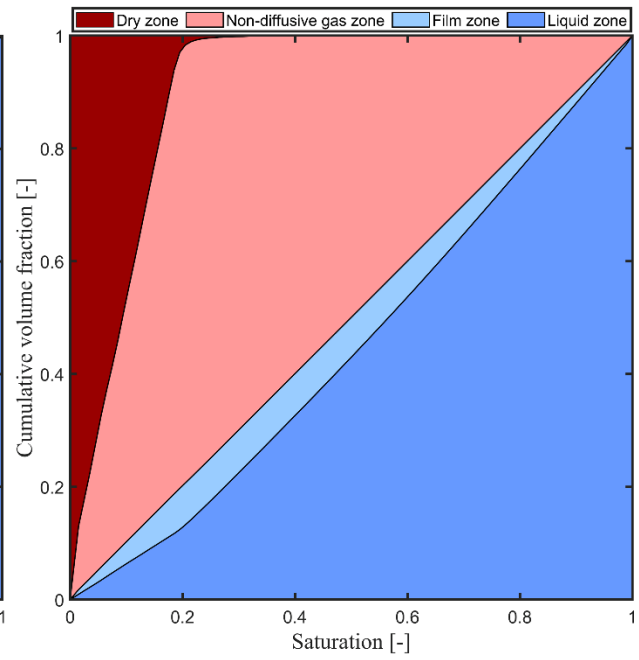


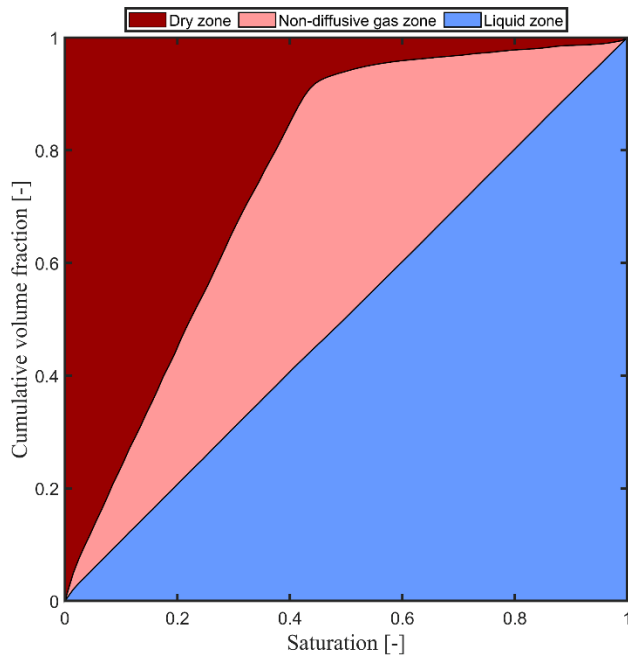
Figure 5.11. Number of isolated single throats and single rings as a function of network saturation by (a) CPNM and (b) RPNM for different values of standard deviation σ_o .



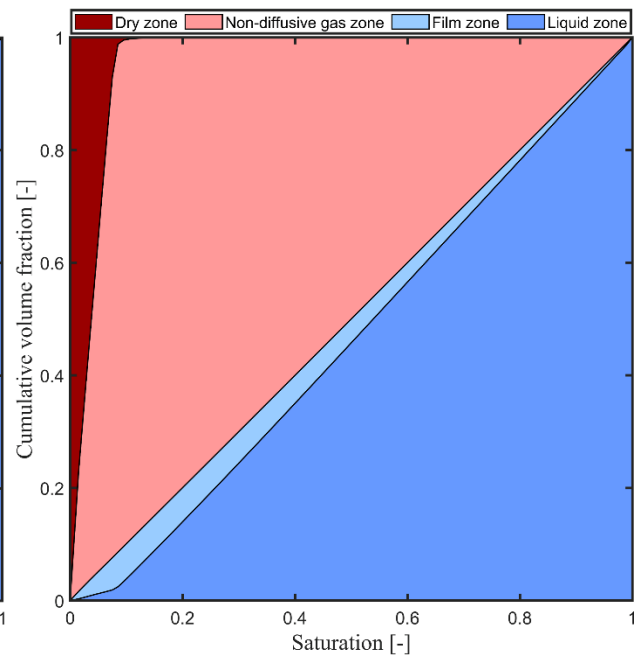
(a)



(d)



(b)



(e)

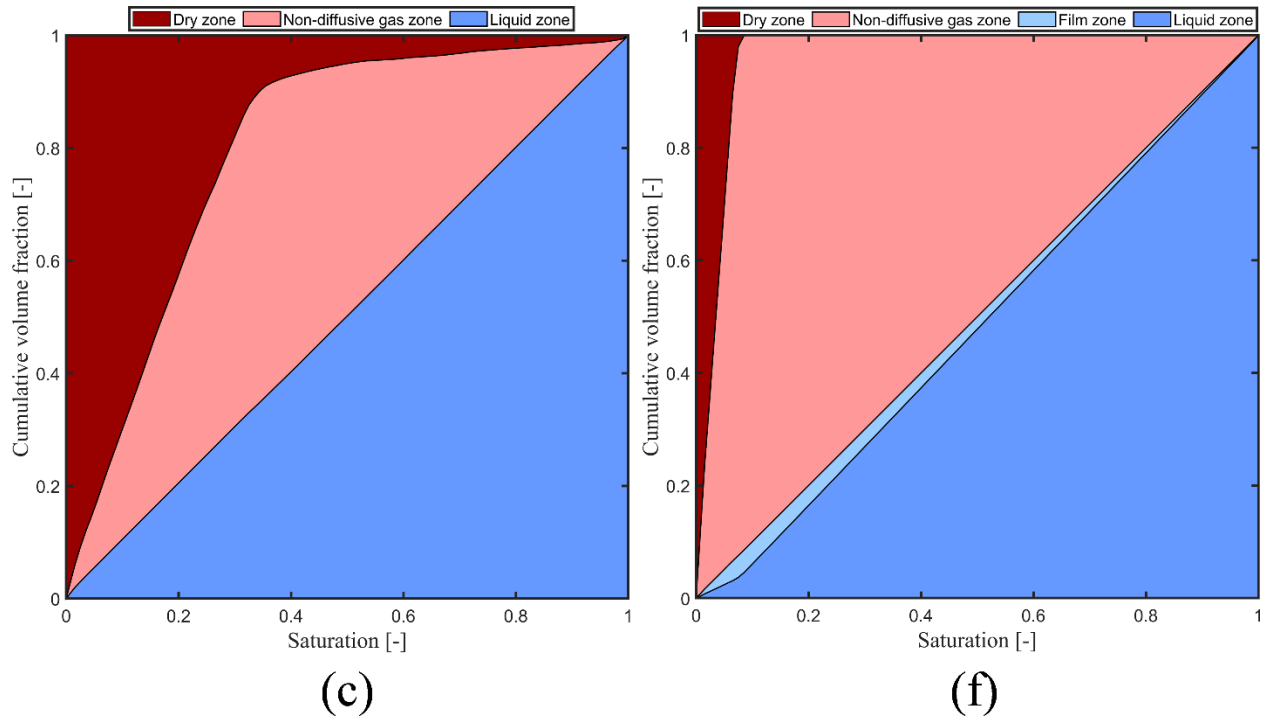


Figure 5.12. Cumulative volume fractions of mass transport zones as a function of network saturation for different standard deviation predicted by CPNM: (a) $\sigma_0 = 10\%$ (b) $\sigma_0 = 50\%$ (c) $\sigma_0 = 100\%$ and RPNM: (d) $\sigma_0 = 10\%$ (e) $\sigma_0 = 50\%$ (f) $\sigma_0 = 100\%$.

5.3 Effect of boundary layer thickness

In order to study the effect of external conditions on drying kinetics, the boundary layer thickness in capillary porous media is changed. This can be achieved in two ways: Either change the number of layers or change the throat length in the boundary layer. In Chapter 4, number of layers is 5 (ϵ_0). In this chapter the number of layers is increased 5 times ($5\epsilon_0$) and 10 times ($10\epsilon_0$) to observe the impact of thickness of boundary layer in RPNM in comparison to CPNM. Table 5.3 shows the characteristics of drying simulations for three networks of CPNM and RPNM with two different values of the boundary layer thickness.

Table 5.3. Characteristics of the pore networks used for drying simulations.

Parameter	CPNM		RPNM	
	Case 10 $\epsilon = 5\epsilon_0$	Case 11 $\epsilon = 10\epsilon_0$	Case 12 $\epsilon = 5\epsilon_0$	Case 13 $\epsilon = 10\epsilon_0$
Network size	19×18×17	19×18×17	19×18×17	19×18×17
Boundary layer size	19×18×25	19×18×50	19×18×25	19×18×50
Throat length (μm)	406	406	406	406
Mean throat radius (μm)	84	84	84	84
Standard deviation of throat radius (μm)	1	1	1	1
Initial volume of liquid water (10^{-7} m ³)	1.48	1.48	1.60	1.60
Network porosity	0.45	0.45	0.49	0.49

The initial evaporation rate depends on the boundary layer thickness, as shown in Fig. 5.13. The boundary layer thickness varies therefore the drying rate is normalized over the initial drying rate of the case 10 in Fig. 5.13 and over the initial drying rate of the same case in Fig. 5.14 to compare change in initial evaporation rate and drying periods, respectively. The water vapor diffusion length increases as the boundary layer becomes thicker. As a result, the rate of evaporation will decrease by the same amount. Therefore, the initial evaporation rate of cases 11 and 13 is half of in case 10 and case 12 in CPNM and RPNM, as shown in Fig. 5.13. Figure 5.14a shows reduction in initial transition period in CPNM with increase of boundary layer thickness and almost perfect CRP similar to RPNM. This change in CRP is due to impact of the boundary layer thickness on the vapor pressure field at the surface. With the thicker boundary layer, a smaller drop in the vapor pressure of the surface pores is observed. The smooth drop in average vapor pressure at

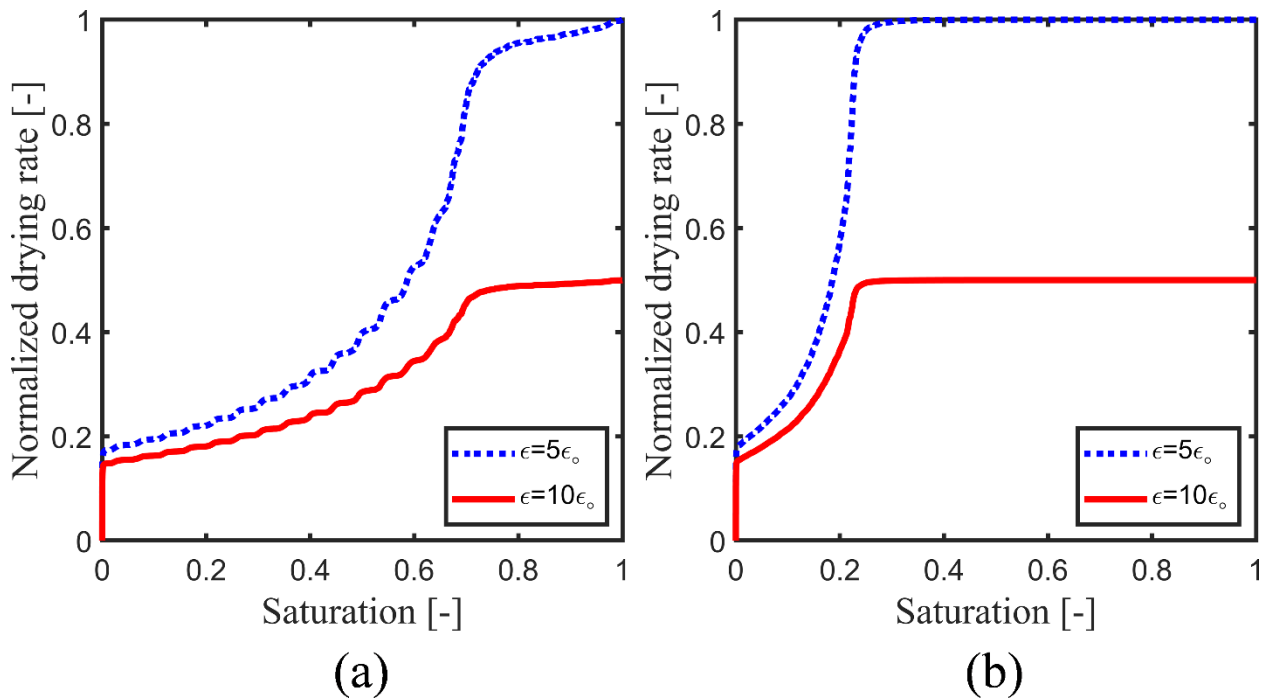


Fig. 5.13. The average normalized drying rate over initial drying of case 10 and 12 ($5\epsilon_0$) as a function of network saturation predicted by (a) CPNM and (b) RPNM, respectively, for different values of boundary layer thickness ϵ . The average curves are obtained considering 3 realizations.

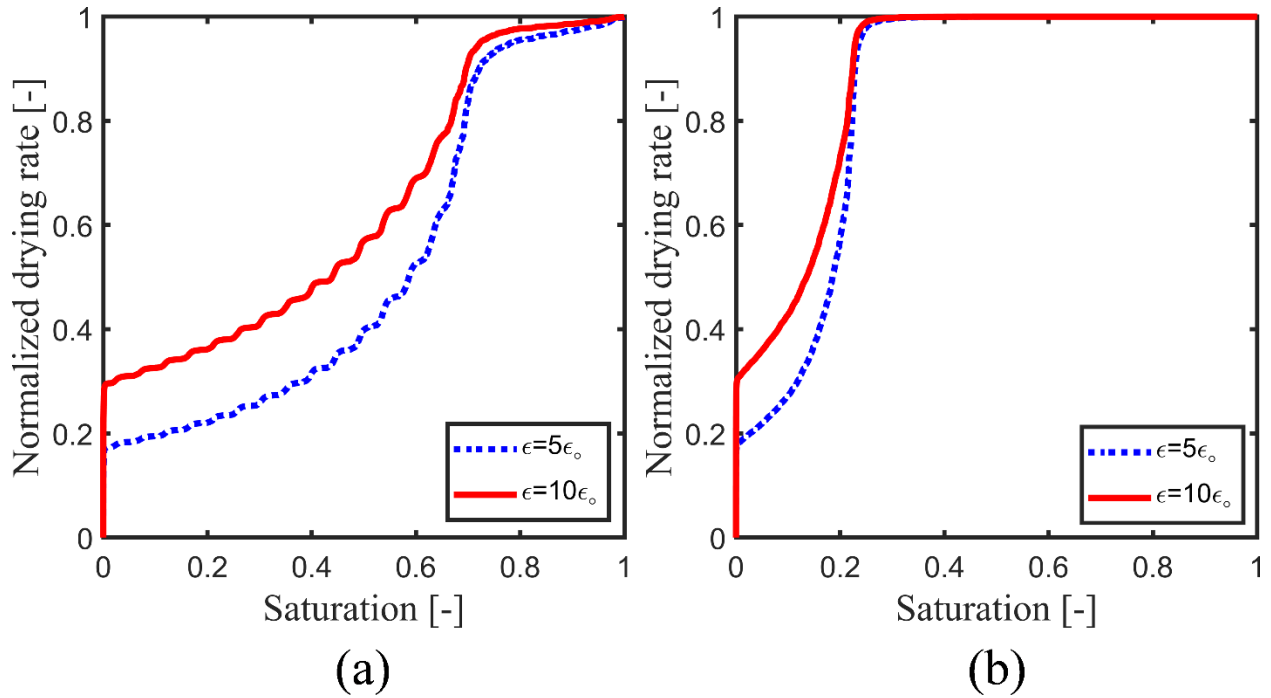


Fig. 5.14. The average normalized drying rate over initial drying of the same case as a function of network saturation predicted by (a) CPNM and (b) RPNM for different values of boundary layer thickness ϵ .

the surface is noticed due to the long distance between the surface pores and the bulk air. Therefore, slightly longer CRP is observed with thicker boundary layer in both models.

The thinner boundary layer results in larger drop of evaporation rate during CRP/FRP transition and lower evaporation rate during RFP. The drying time mainly depends on the initial evaporation rate and the duration of the faster drying period. It decreases with an increase in the initial drying rate and the CRP. As discussed, the evaporation rate decreases with increase in the boundary layer thickness but does not significantly affect the duration of CRP. Therefore, the time required to evaporate the liquid from the network increases with increase in the boundary layer thickness, as shown in Fig. 5.15. But the drying time in CPNM increases by a factor of 1.36, as compared to a factor of 1.65 in RPNM due to reduction in initial transition period and smoother CRP. The liquid phase distribution and transport zones of both models are independent of the boundary layer thickness, as shown in Fig. 5.16.

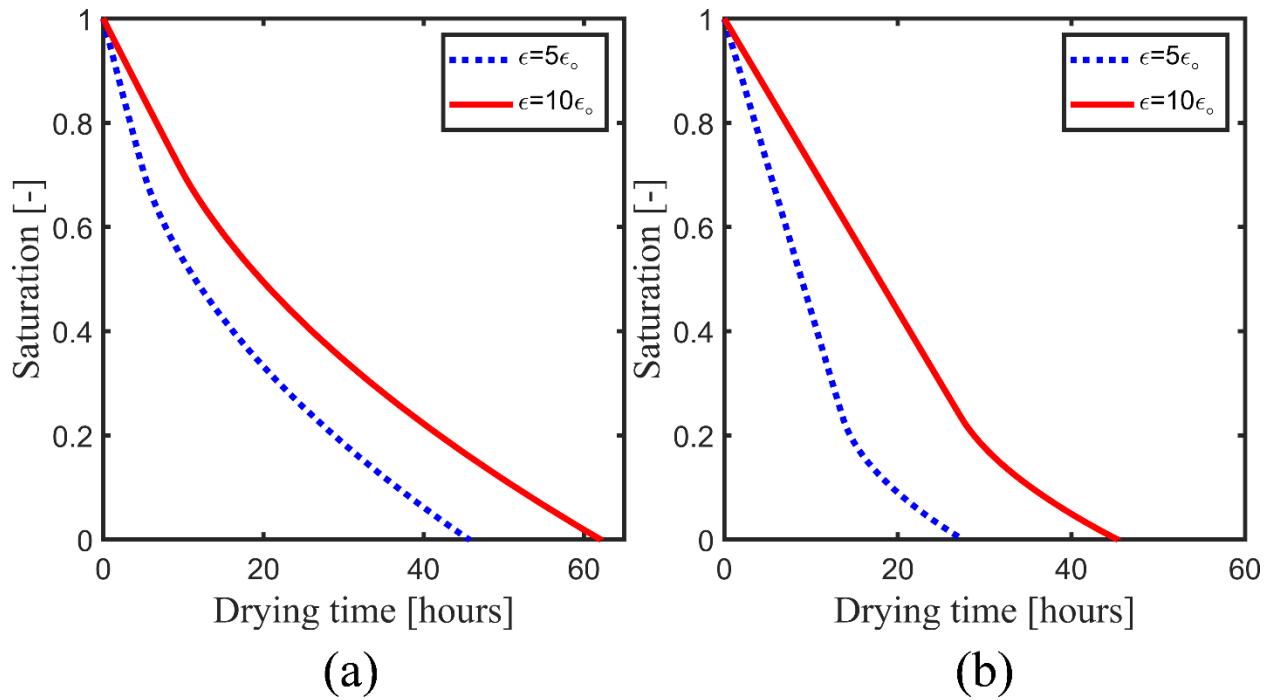
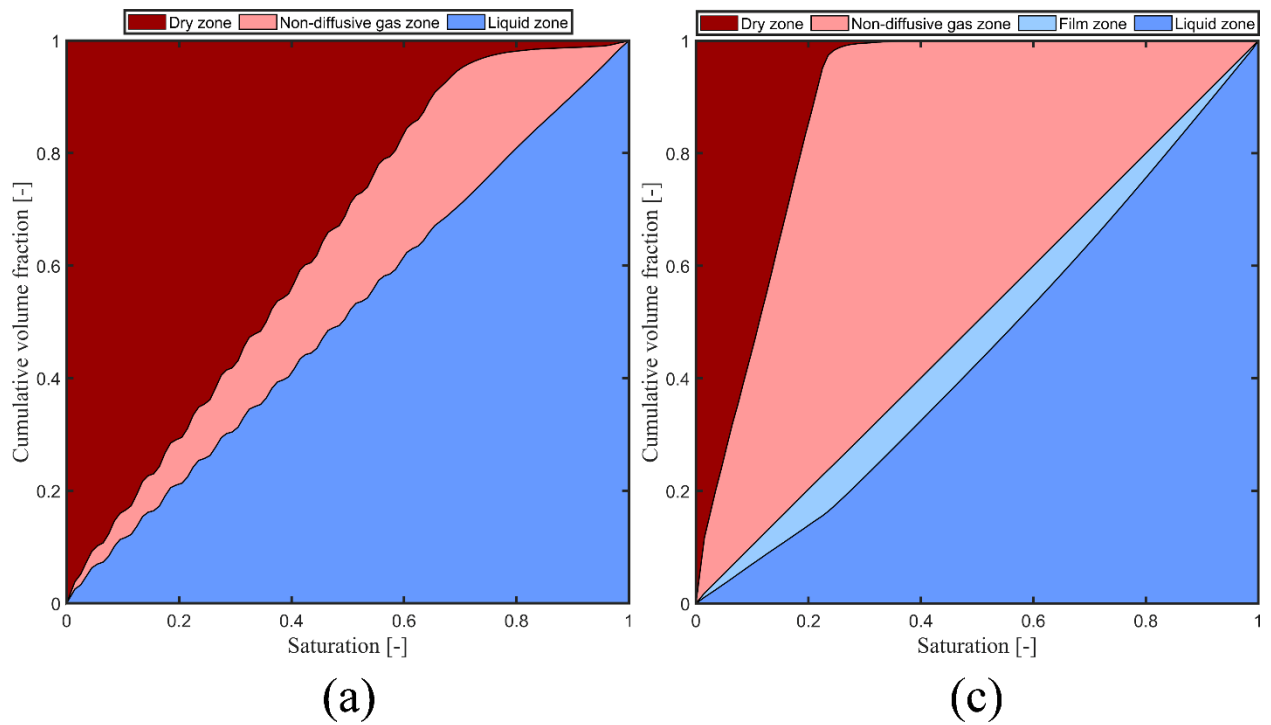


Figure 5.15. Drying curves obtained from (a) CPNM and (b) RPNM for different values of boundary layer thickness ϵ .



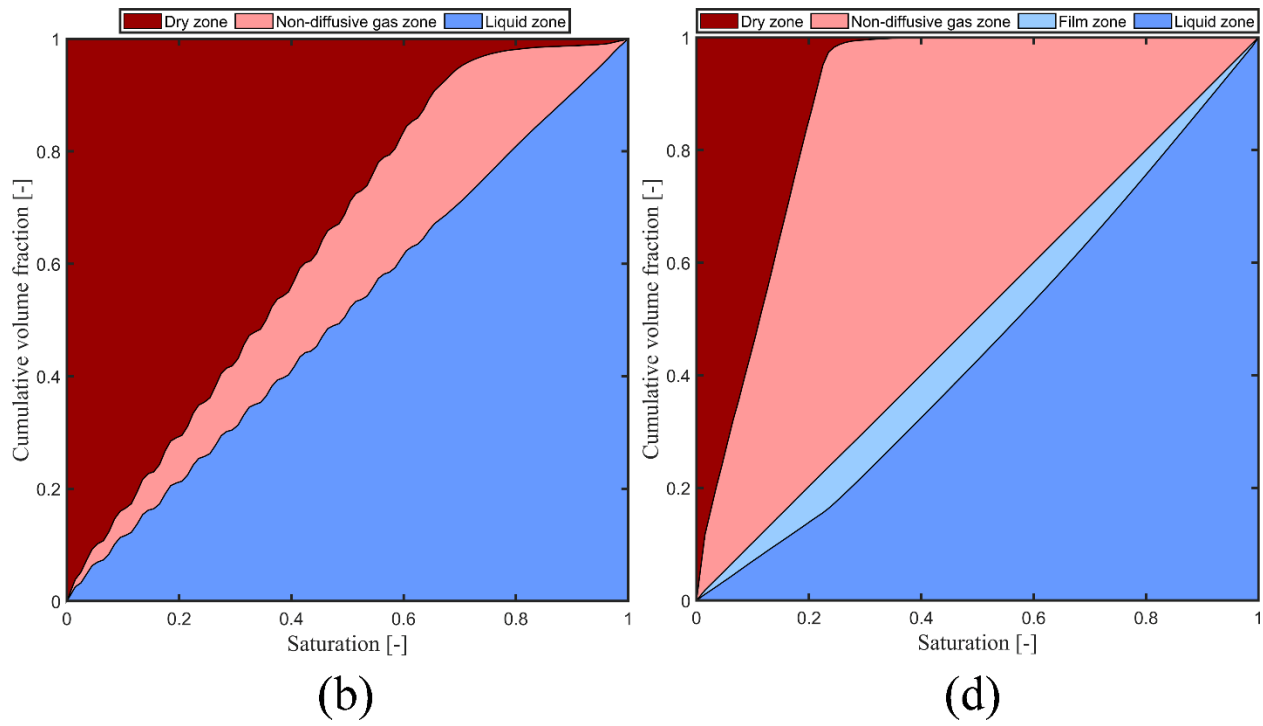


Figure 5.16. Cumulative volume fractions of mass transport zones as a function of network saturation for different boundary layer thickness predicted by CPNM: (a) as $5\epsilon_0$, (b) as $10\epsilon_0$ and RPNM: (c) as $5\epsilon_0$, (d) as $10\epsilon_0$.

Chapter 6

Part of this chapter has been published in “Mahmood, H.T., Tsotsas, E., Kharaghani, A.: The role of discrete capillary rings in mass transfer from the surface of a drying capillary porous medium. *Transport in Porous Media*, 140, 351-369 (2021)”.

6 Role of rings in mass transfer from the surface of a drying porous medium

6.1 Background

The role and significance of liquid films in relation to the mass transport at the interface between the porous medium surface and the adjacent air have not been widely studied in literature, neither experimentally nor numerically. Linking the surface mass transfer attributes with the adjacent air has been considered as a specific research topic by Schlünder (1988, 2004). His main motivation was essentially to explain why the evaporation rate from the surface of a partially saturated porous medium is nearly identical to that of a fully saturated surface. In other words, a simple mathematical description of a long constant rate period (CRP) in drying kinetic curves determined experimentally was aimed. In order to derive an analytical model, Schlünder made four assumptions: (i) Only wet patches at the surface contribute to the net evaporation rate, (ii) wet patches are hemispherical droplets with uniform radius (r_t) which are evenly placed inside squares of size $(2l \times 2l)$, (iii) the liquid vapor generated by evaporation is

transported by equimolar diffusion from the medium surface to the bulk air and (iv) wet patches have radii much smaller than the thickness of the external boundary layer (δ). On the basis of these assumptions, Schlünder derived the following correlation:

$$\frac{J}{J_{\max}} = \frac{1}{1 + \frac{2r_t}{\pi\delta} \sqrt{\frac{\pi}{4\theta}} (\sqrt{\frac{\pi}{4\theta}} - 1)}, \quad (6.1)$$

where J denotes the evaporation rate, J_{\max} the initial evaporation rate when the surface is fully wet and $\theta = \frac{\pi r_t^2}{(2l)^2}$ the wetted surface area.

The surface attributes during the drying process are, though, not as simple as "seen" and formulated by Schlünder. The research conducted by classical 3D pore network model (CPNM) simulations shows that instead of only wet patches (represented by liquid-filled surface pores in PNM) both wet patches and dry patches (represented by empty surface pores in PNM) contribute to the mass exchange at the medium surface (Moghaddam et al., 2018). The study conducted by Talbi and Prat (2019) clearly shows that the size distribution of wet patches and the shape of droplets impact the drying characteristics at the surface. Details of Schlünder's model in connection to closure relationship and CPNMs have thoroughly been described in previous works (e.g. Lehmann and Or, 2013; Moghaddam et al., 2018; Talbi and Prat, 2019; Lu et al., 2021). While these works contributed to a much better understanding of the mass transfer at the surface, they disregarded the impact of the liquid films developing in geometrical singularities of the pore space during drying.

In this work, the extent over which capillary rings can impact the mass exchange between the porous medium surface and the bulk air is studied. For this purpose, numerical simulations of a drying capillary porous medium are carried out using the CPNM and ring pore network model (RPNM). The results obtained from these two models are compared against the model proposed by Schlünder.

6.2 Model parameters

The parameters used for both PNM simulations are presented in Table 6.1. The boundary layer is embodied by adding 10 nodes in vertical direction with the same cross-section of the network (25×25). The results are averaged over 15 realizations for each model. The drying process is limited to isothermal capillary dominated regime for non-adsorbed water. Vapor diffusion in the film and non-diffusive gas zones is suppressed. Gas pores at equilibrium vapor pressure and vapor pressure of dry air at uppermost layer of pores of the external boundary layer ($P_{v,\infty} = 0$) provides boundary conditions. The diffusive transport in the boundary layer is considered.

Table 6.1. Parameters used for CPNM and RPNM drying simulations.

Parameter	CPNM	RPNM
Pore network size	25×25×51 nodes	25×25×51 nodes
Boundary layer size	25×25×10 nodes	25×25×10 nodes
Mean throat radius (μm)	207	207
Standard deviation in throat radii (μm)	20.7	20.7
Throat length (μm)	1000	1000
Ring radius (μm)	-	252
Ring thickness (μm)	-	137.1
Temperature (°C)	20	20
Gas pressure (atm)	1	1
Network porosity (-)	0.44	0.49
Top network surface porosity (-)	0.15	0.18

6.3 Drying kinetics

The normalized evaporation rate and surface saturation obtained from both pore network models, i.e. CPNM and RPNM, under identical initial and boundary conditions

are shown in Fig. 6.1. Both models are capable of predicting three main periods of drying of capillary porous media, but with different extent. During constant rate period (CRP), the evaporation rate decreases slightly in the CPNM. The drop from the initial evaporation rate termed as initial transition period has also been observed in previous classical pore network simulations (Moghaddam et al., 2017 and 2018). In these studies, the drop was commonly deduced to occur due to the invasion of surface pores from the beginning of the drying process until the gas phase breakthrough, i.e. until the gas phase reaches the network bottom for the first time. Interestingly, even though the surface pores are invaded by the gas phase and the breakthrough predicted by both CPNM and RPNM occurs more or less at the same time (see circles in Fig. 6.1), the drop is completely circumvented and the evaporation rate remains at the highest initial value for a significant period of drying in RPNM. In order to find out reasons underlying this observation, the saturation of the network surface is calculated for both types of pore network. The surface in RPNM is defined as all vertical throats and rings at the interface between the network and ambient air, whereas only vertical throats at the interface describe the surface in CPNM. A sharp drop in the saturation of the network surface is readily notable in both pore networks, but with magnitudes that differ by a factor of more than two (see Fig. 6.1). At first sight it may appear that this difference attributes to the decrease in evaporation rate during the initial transition period. If this was the only reason, one would also expect a decrease in the evaporation rate of RPNM, though to a smaller extent. We will get back to this point later on in this section.

When CRP ends, the evaporation rate drops significantly and the falling rate period (FRP), often called the diffusion-controlled regime, onsets. At some point during the CRP/FRP transition, the liquid phase does not spread over the whole height of the network (irreducible saturation) as indicated by squares in Fig. 6.1. Compared to CPNM (also, see, Yiotis et al., 2006; Moghaddam et al., 2017), the irreducible saturation of RPNM is very low, similarly as in experiments (Faure and Coussot, 2010). The decrease in irreducible saturation is caused by the liquid rings within the network. The inclusion of

this secondary capillary structure in the RPNM promotes spanning of the main liquid cluster and also increases the coordination number of pores from 6 neighboring throats in CPNM to additional 12 neighboring rings in RPNM.

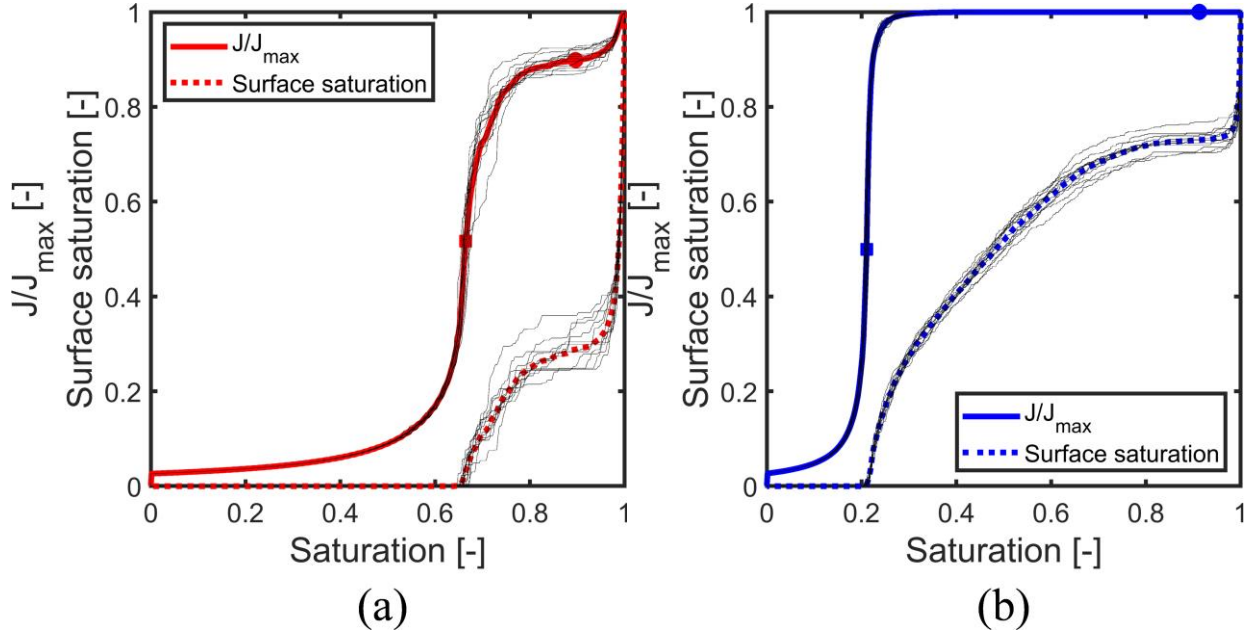


Fig. 6.1. The normalized evaporation rate and surface saturation as a function of network saturation predicted by (a) CPNM and (b) RPNM. All 15 realizations (thin lines) and the arithmetic mean (thick lines) are shown. The instants at breakthrough and irreducible saturation are indicated by circles and squares, respectively.

Let us come back to the question why the immediate drop in surface saturation cannot reduce the evaporation rate in the RPNM. In other words, why the initial transition period is completely bypassed in the RPNM. To answer this question, the transport zones defined in Sec. 3.2.1 are computed using both types of pore networks and the respective simulation results are visualized in Fig. 6.2. As can clearly be seen, the role of liquid rings in distribution of the liquid and gas phases is remarkable. Though the rings contribute only 7.7% to the total liquid volume, they can assure liquid transport from the network inside towards its surface, hence enhancing and prolonging the surface wetness. The zones occupied by the gas phase, i.e. non-diffusive gas zone and dry (or diffusive gas) zone, are distinguished based on their resistance for vapor transport. Vapor diffusion is

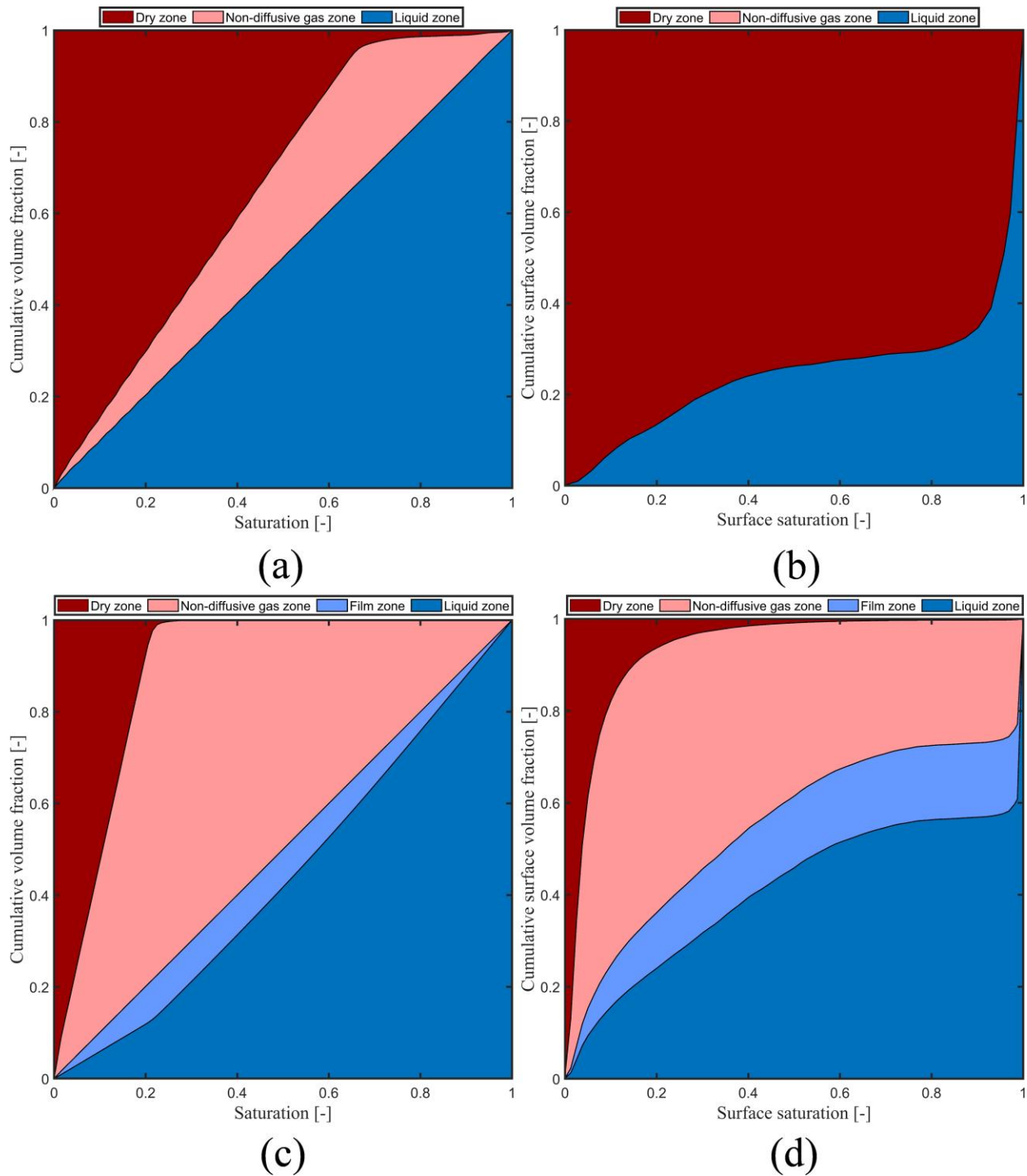


Fig. 6.2. Cumulative volume fractions of mass transport zones as a function of network saturation predicted by CPNM (a, b) and by RPNM (c, d). The transport zones developed inside the pore networks (a, c) and at their respective surfaces (b, d). The data have been averaged over 15 realizations.

fully suppressed in the non-diffusive gas zone, whereas the dry zone poses resistance to vapor transport. Right from the beginning of drying the non-diffusive gas zone develops and its relative contribution to the total volume of zones increases during CRP, thereby an initial transition period cannot be developed in the RPNM.

Another interesting piece of information that can be inferred from Fig. 6.2 is the transition from the FRP to the RFP. This transition point occurs when the extent of the dry zone across the network becomes the largest (cf. Figs. 6.1 and 6.2).

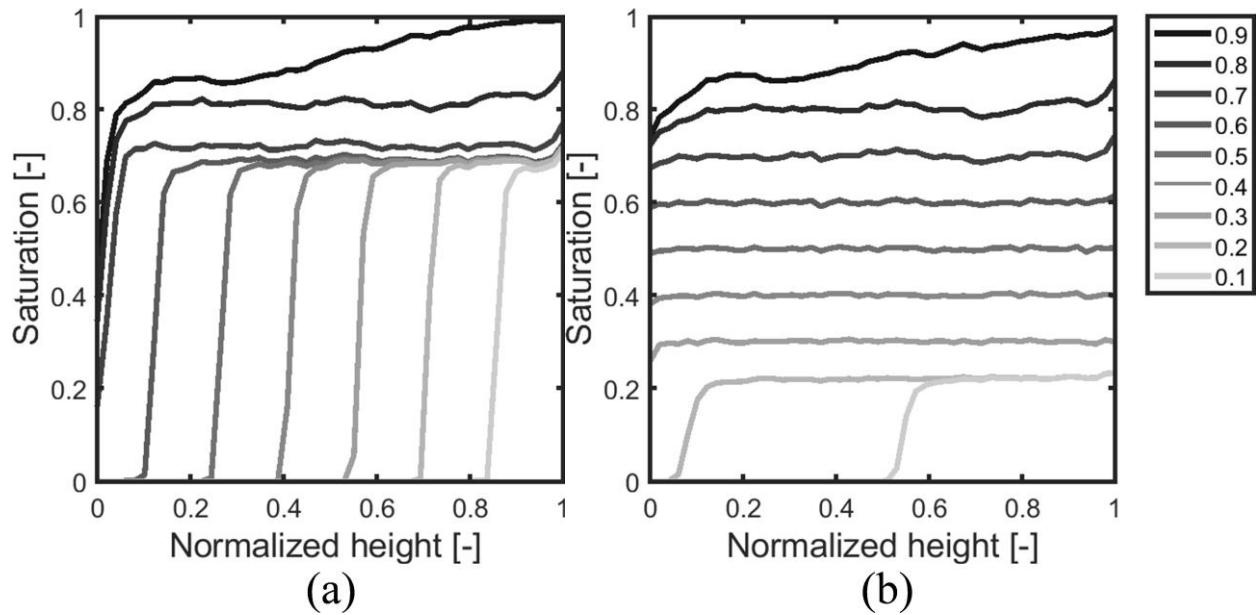


Fig. 6.3. Profiles of slice-averaged saturations for: (a) CPNM and (b) RPNM, averaged over 15 realizations. The network top surface is at 0 and bottom of the network is at 1.

The network saturation reaches the irreducible saturation during the CRP/FRP transition in both models. The impact of the irreducible saturation is shown in Fig. 6.3. Each slice of the ring pore network contains horizontal and vertical planes of throats and rings (see Fig. 3.2), while it consists of only throats in the classical pore network. As pointed out previously, the process of liquid percolation from the bottom slice to the surface slice is terminated after the irreducible saturation. This is obvious from the profiles of slice-

averaged saturations (cf. Fig. 6.3). After 0.66 network saturation in CPNM, saturation of the bottom slice remains nearly unchanged while in RPNM saturation of the bottom slice decreases until 0.21. These profiles are spatially uniform along the height during CRP in both models. A sharp drop in profiles of saturation near the surface of evaporation (top edge effect) is not dominant in RPNM as it is in CPNM because of gradual decrease in surface saturation and absence of initial period (see Fig. 6.3).

6.4 Evolution of liquid structure

The influence of rings on the evolution of the liquid structures (isolated elements and clusters) inside the network and at the surface is presented in Fig. 6.4. As can be seen, the number of single throats and clusters at the surface in CPNM increases significantly right from the beginning of the drying process. This behavior again explains the initial transition period in CPNM. After this period the liquid structures at the surface develop with a similar trend in both models with an exception of delayed disintegration in RPNM (Figs. 6.4a and b). Inside the network, the disintegration of the liquid structure occurs at a later stage of CRP in RPNM while it starts from the beginning in CPNM. In both networks, the maximum number of liquid structures exists near the end of CRP (Figs. 6.4c and d).

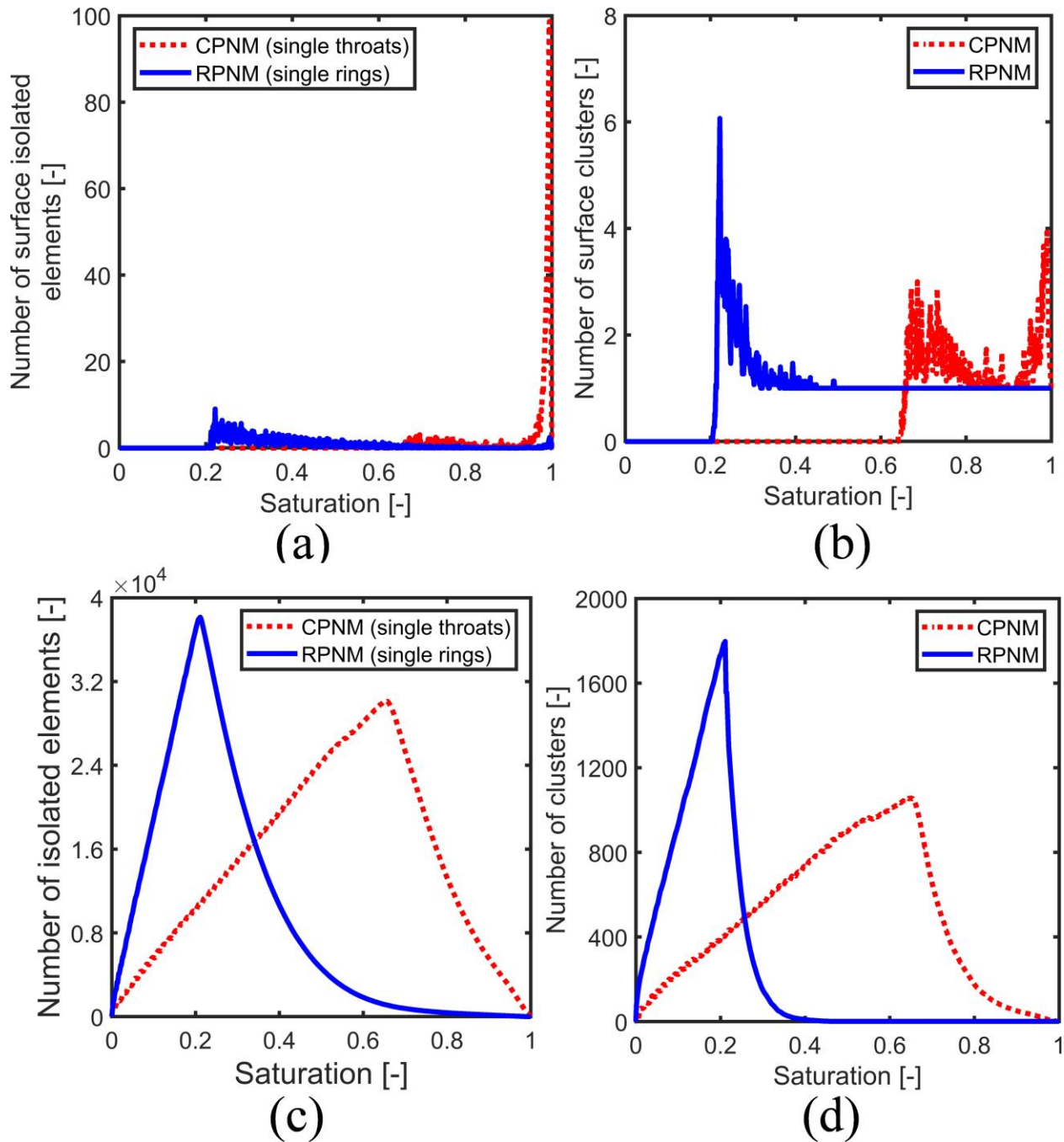


Fig. 6.4. For both CPNM and RPNM: (a) Number of isolated elements at the network surface, (b) number of clusters connected to the network surface, (c) number of isolated elements in the network and (d) number of clusters in the network as a function of network saturation, averaged over 15 realizations.

A detailed analysis of the evolution of liquid structures inside the network based on the position and the main liquid cluster provides interesting insight into the phenomena that occur during drying. As shown in Fig. 6.5, the pore network is divided into top and bottom regions in the direction of height based on proximity to the open side of the network or the opposite sealed side of the network. During CRP, the evolution of liquid structures in both regions and models is similar except an initial higher growth of the disintegration of the liquid in the top region of CPNM. Afterwards, this conduct becomes contradictory. The liquid structures in the top region of the network decline while they become almost stable in the bottom region for considerable duration in both models. This stability in the bottom region is due to increase in number of small clusters and the liquid removal from the top region only, as explained later. Apparently, duration of this stable state is longer in CPNM, however, this duration is approximately similar relative to

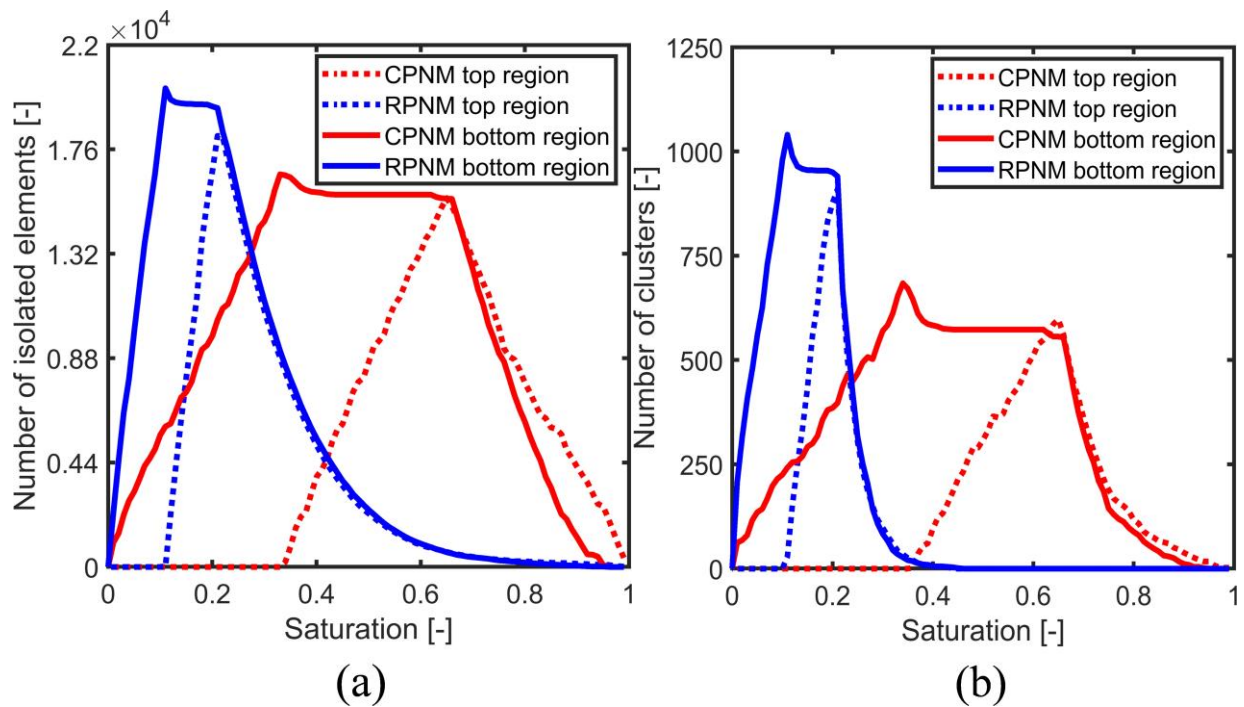


Fig. 6.5. Number of isolated elements (a) and clusters (b) as a function of network saturation, obtained for a single realization.

duration of RFP in both networks. The number of clusters spreading over both regions is very small in both models and not plotted in Fig. 6.5.

Figure 6.6 reveals size of clusters, especially the main cluster, during drying. Almost all liquid belongs to the main cluster during CRP in RPNM (Fig. 6.6a). The relative volume of the main cluster to total liquid volume in RPNM is close to experimentally measured value (Kharaghani et al., 2021). The abrupt drop in the volume of the main cluster illustrates a high disintegration of the liquid phase inside the network and triggers CRP/FRP transition in both models. Size of other clusters is minuscule relative to the main cluster in both networks, however, a significant amount of volume belongs to the isolated elements in CPNM during CRP as can be concluded from disparity between Figs. 6.6a and b. After FRP, size of all clusters is small and comparable.

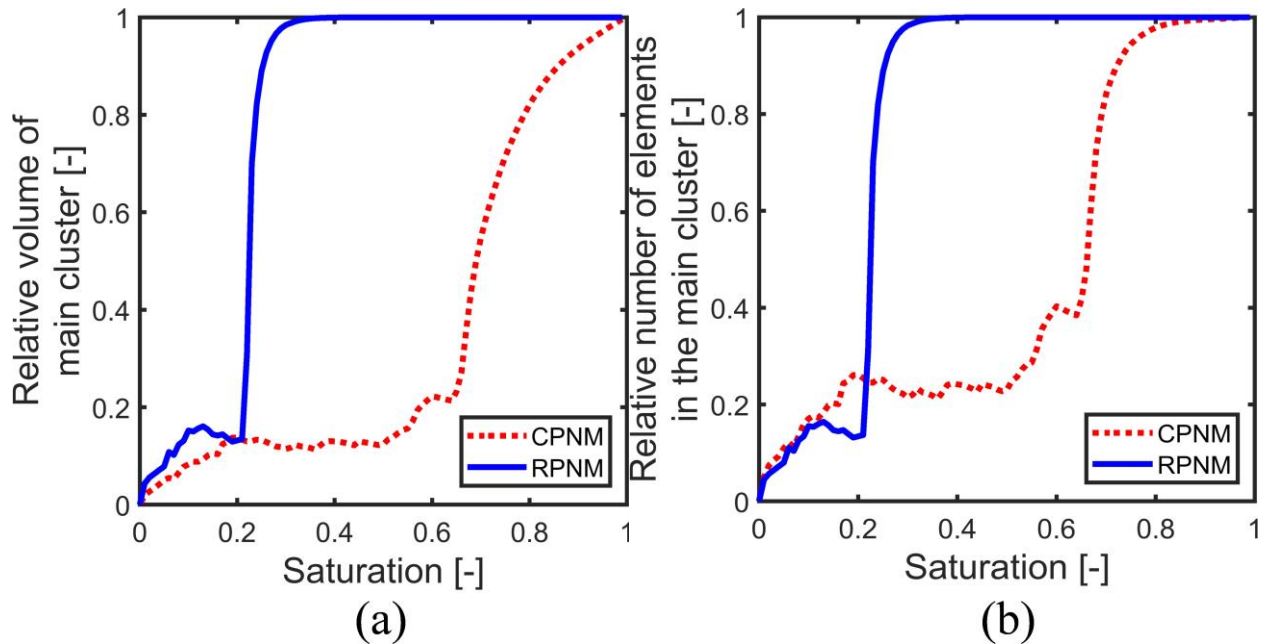
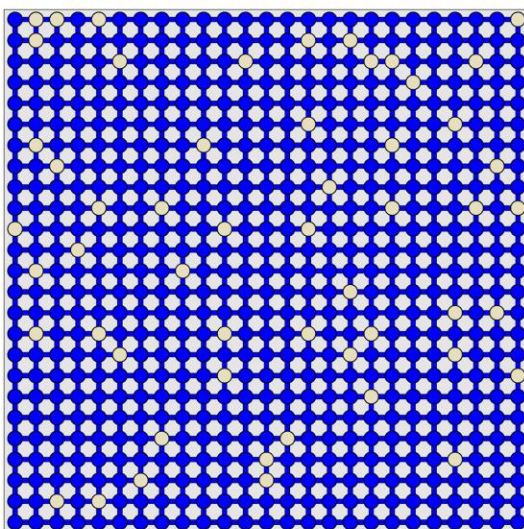


Fig. 6.6. (a) Relative volume of the main liquid cluster to the total liquid volume and (b) relative number of elements in the main liquid cluster to the total liquid clusters (excluding isolated elements) as a function of network saturation, averaged over 15 realizations.

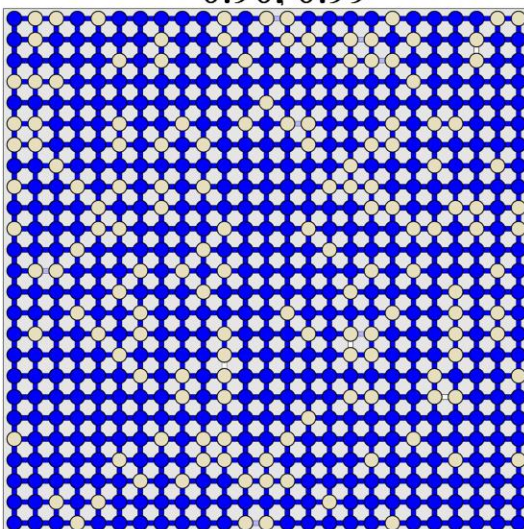
As discussed above, the drying process can be described by the liquid cluster formation inside the network and at the network surface. The residence time of a cluster depends upon the position and size of the cluster. A cluster will stay longer if it is large and stays further away from the network surface. Figure 6.7 shows the top view of the network where throats are represented by circles and rings by rectangles. Different colors have been assigned to different clusters. If two elements are not connected at the surface but they are connected inside the network, they belong to the same cluster. Diffusive empty throats and empty rings are shown in white, non-diffusive gas throats in off-white, and isolated elements in red. The biggest cluster at the surface is visualized in blue. The total number of throats at the surface is 625 in both models. The surface of RPNM contains additional 1250 rings with an attribution of only 3% additional volume. The RPNM and CPNM are visualized side by side for comparison. In addition to values of the surface saturation, values of the network saturation are shown.

Saturation of the surface decreases rapidly before the breakthrough occurs in both models. After breakthrough, saturations of both the surface and network decrease in RPNM while in case of CPNM this trend is different. For surface saturation 0.90-0.60, the network saturation in RPNM decreases to 0.58, while the network saturation of CPNM remains nearly unchanged. This means almost all liquid is evaporated from the surface of the classical pore network during this period. Moreover, the liquid and gas elements at the surface based on $(P_{v,eq})$ or (P_v) are termed as wet patch and dry patch, respectively. At a lower surface saturation of 0.45, the network saturation is 0.45 and 0.97 in RPNM and CPNM, respectively, which indicates pumping of liquid from deep inside of the network towards surface is efficient in presence of rings. Isolated elements and different clusters at the surface represent disintegration of the liquid phase. Number of single throats at the surface of classical pore network is significant from high to low saturation (see red color on the right side of Fig. 6.7). It means single throats stay there for longer time. Number of isolated rings is insignificant in RPNM, even number of rings is double

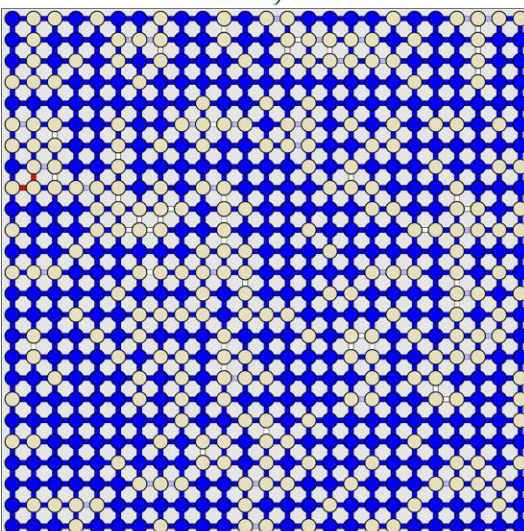
RPNM



0.90, 0.99

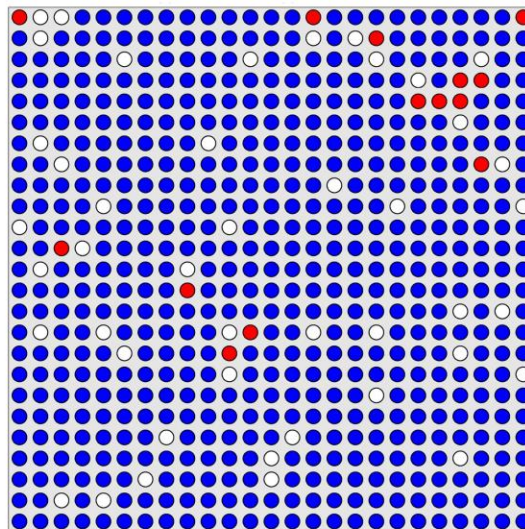


0.75, 0.96

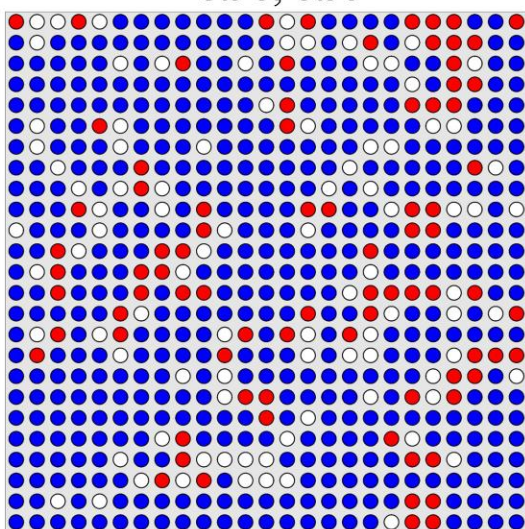


0.60, 0.58

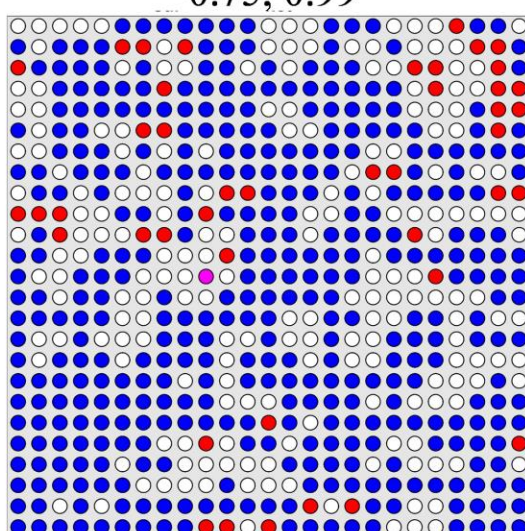
CPNM



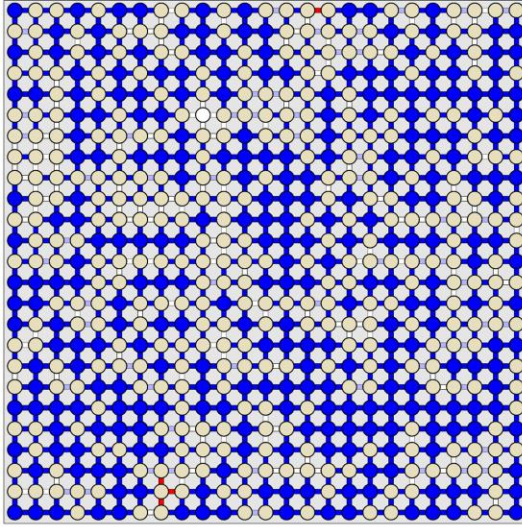
0.90, 0.99



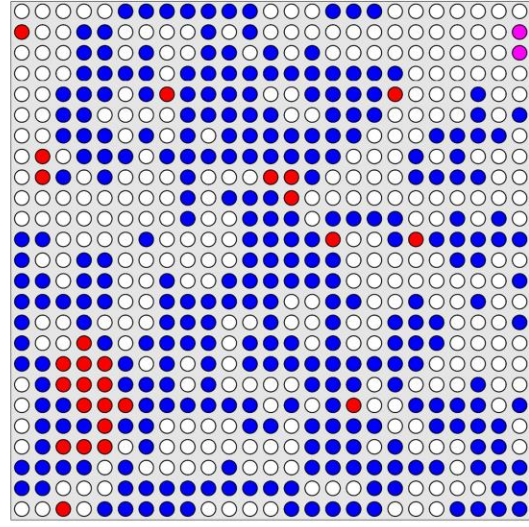
0.75, 0.99



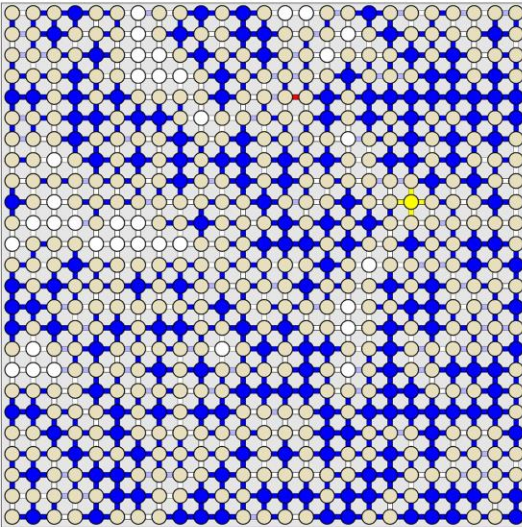
0.60, 0.99



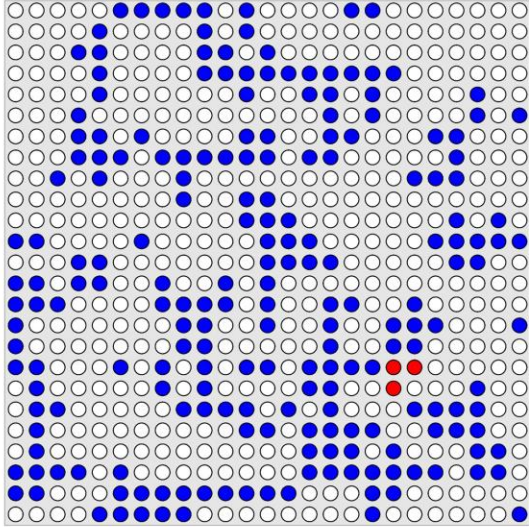
0.45, 0.44



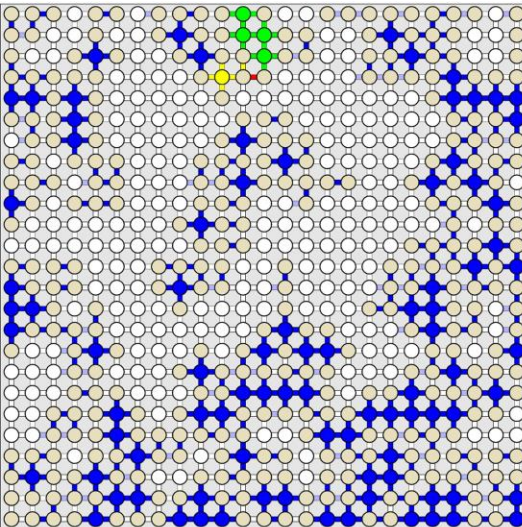
0.45, 0.97



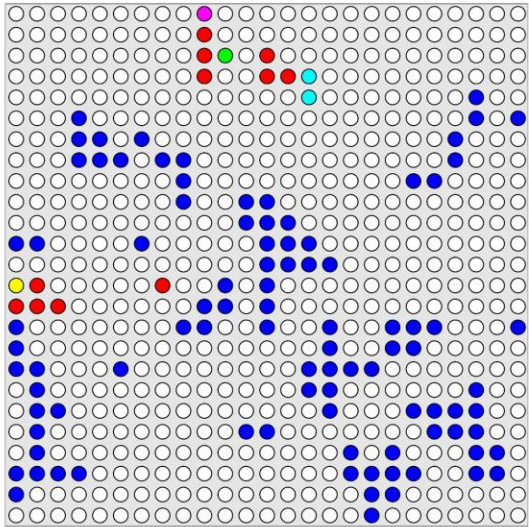
0.30, 0.32



0.30, 0.82



0.15, 0.24



0.15, 0.72

Fig. 6.7. Two-dimensional visualization of the evolution of liquid structure at the surface of a RPNM (left) and CPNM (right) for the surface saturation values of 0.90, 0.75, 0.60, 0.45, 0.30, 0.15 (Adjacent values at the bottom are network saturation values on these surface saturation values). Empty and isolated elements are shown in white/off-white and red, respectively. Other colors indicate liquid clusters while the main cluster is shown in blue (a single realization).

than the number of throats while the number of empty elements is growing (see red and white color on the left side of Fig. 6.7). This indicates that the single rings dry quickly when they become isolated. Maximum liquid clusters at the surface belong to the main cluster from high to low saturation of the surface in both models (see blue color in Fig. 6.7).

6.5 Pressure field

The impact of rings on the time evolution of the vapor pressure field at the network surface is shown in Fig. 6.8. During the initial transition period of the CPNM, the quick removal of liquid from the surface reduces the vapor pressure at the entrance of surface pores from the equilibrium vapor pressure ($P_{v,eq}$) to lower values. Thus, the fraction of the surface pores at vapor partial pressure (P_v), which are not connected to the liquid phase, starts increasing progressively from the beginning of the drying process until complete drying of the network. When almost half of the network surface has been dried, the number of surface pores at P_v becomes dominant, while all the surface pores in the ring pore network remain at equilibrium vapor pressure during this period. This transition point occurs when only a small amount of the total liquid ($\sim 2\%$) is evaporated from the classical pore network. However, the transition point in RPNM is reached when an enormous amount of the total liquid ($\sim 75\%$) has been evaporated (cf. Figs. 6.8 and 6.1).

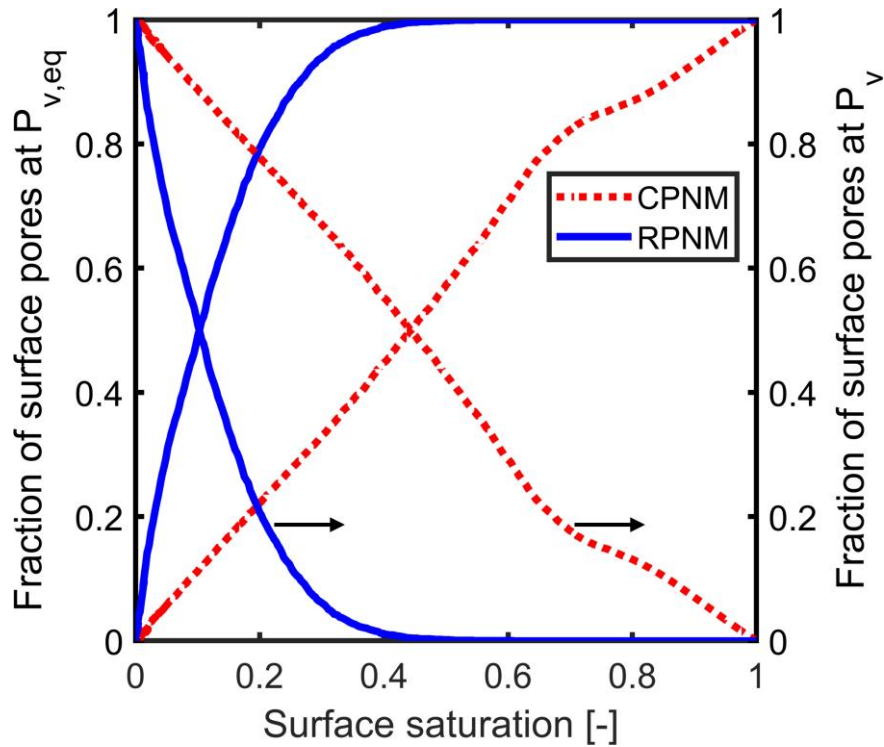


Fig. 6.8. Fraction of surface pores at equilibrium vapor pressure ($P_{v,eq}$) and pores at averaged vapor partial pressure (P_v) as a function of surface saturation, averaged over 15 realizations.

The fact that the average vapor partial pressure at the surface of a drying capillary porous medium is lower than the equilibrium vapor partial pressure is referred to as non-local equilibrium effect in previous studies (Moghaddam et al., 2017; Lu et al. 2021). This effect is decreased in RPNM, as shown in Fig. 6.9a. Figure 6.9b shows standard deviation of the averaged vapor pressure at the surface for both models as a function of surface saturation. The standard deviation of the averaged vapor pressure of RPNM remains zero until low network saturation (cf. Figs. 6.9b and 6.1), while it increases continuously towards maximum value in CPNM. The highest standard deviation shows in the end of the CRP/FRP transition and with a small part of wet patches at the surface in both models. After that, the surface dries out completely. The variation of the vapor pressure field due to rings also explains duration of CRP and dominance of wet patches during most of the CRP.

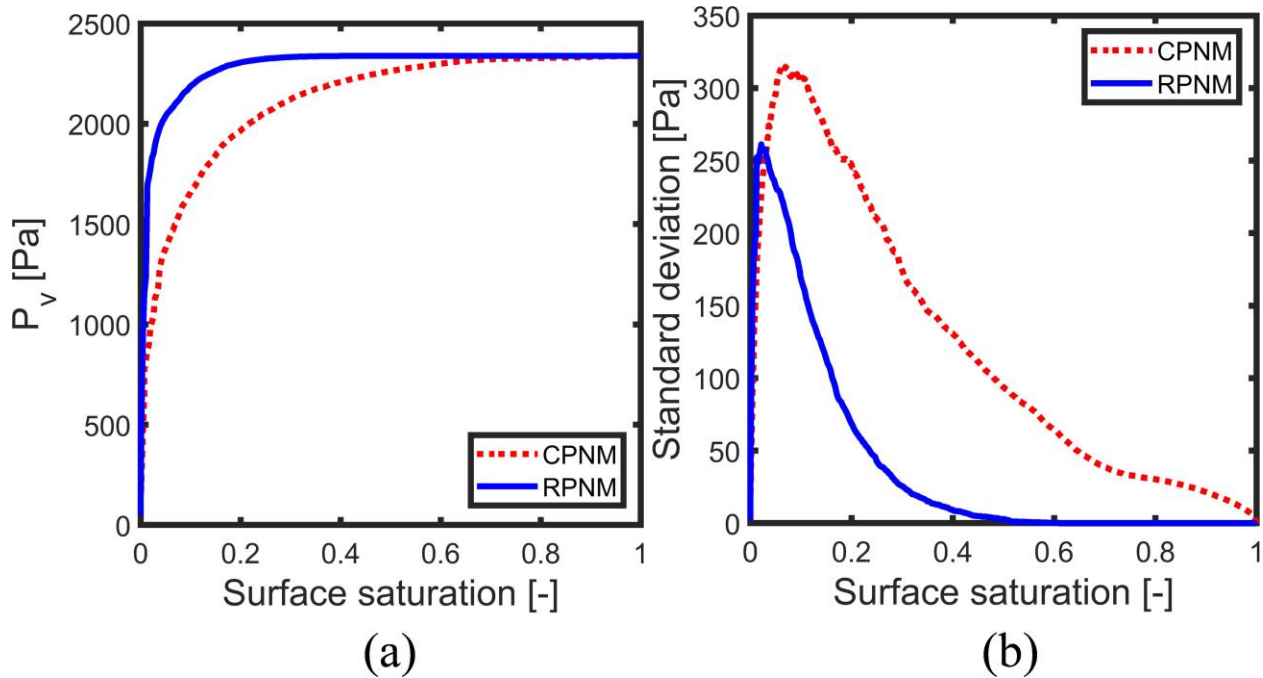


Fig. 6.9. Variation of the average (a) and standard deviation (b) of the vapor partial pressure as a function of surface saturation, averaged over 15 realizations.

The evaporation rate can be fractionated into two components: The evaporation rate from the wet patches and that from the dry patches at the surface. The relative contribution of the wet and dry patches at the surface to the net evaporation rate is shown in Fig. 6.10. The role of dry patches in CPNM is significant and starts from the beginning of the drying process to fully dried surface. The contribution of dry patches becomes dominant at 0.25 saturation of the surface. The role of wet patches in RPNM is fully dominant from start of the drying process to surface saturation of 0.38. After this point, dry patches start contributing, but their role is still smaller than that of wet patches until the surface saturation reaches 0.04. The evaporation rate is high in case of wet patches, as vapor pressure at the pore entrances is the equilibrium vapor pressure. Rings have shifted the transition between dominant contributing patches towards very low saturation and have made the wet patches to the sole contributor for most of the CRP.

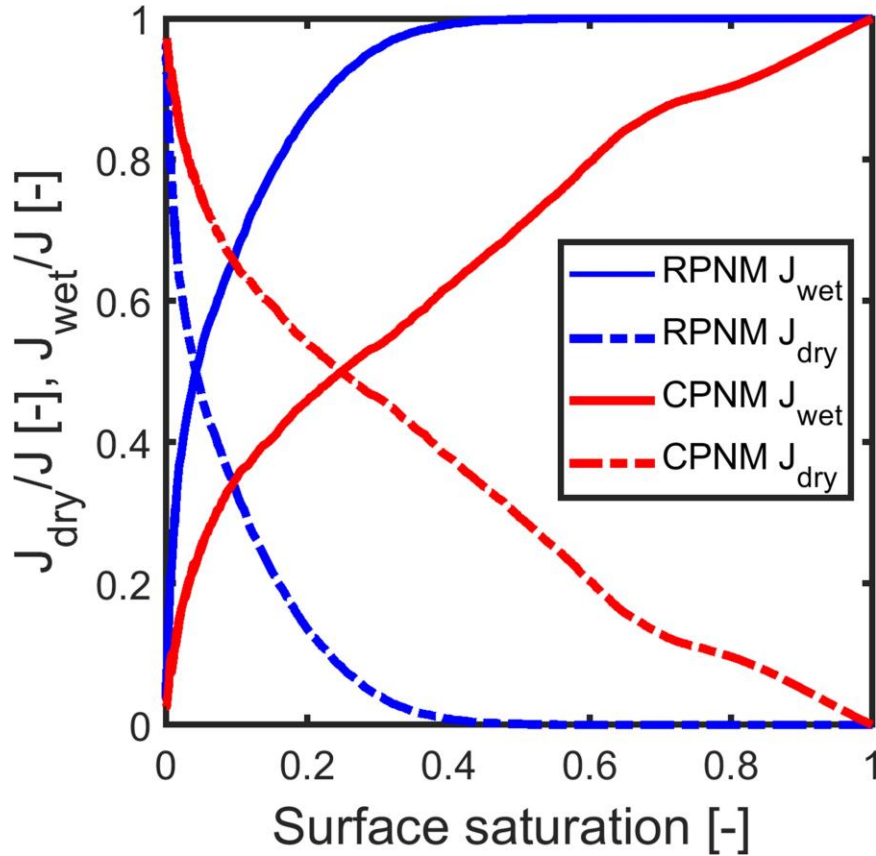


Fig. 6.10. Relative contributions of dry and wet patches at the network surface to the total evaporation rate for CPNM and RPNM as a function of surface saturation, averaged over 15 realizations.

6.6 Comparison with classical and Schlünder's model

As discussed in Sec. 6.1, Schlünder's model provides the closure relationship of the evaporation rate with the surface wetness. This model requires three input parameters with values which need to be specified a priori. A gas diffusion length of $10L$ is considered in the pore network simulations, where L denotes the throat length. The porous medium surface of Schlünder's model is homogeneous, as opposed to pore network models. The radius of a wet patch (r_t) is taken as the mean throat radius and the surface wetness (θ) is identified from the pore network modeling as wet area of throats or surface saturation.

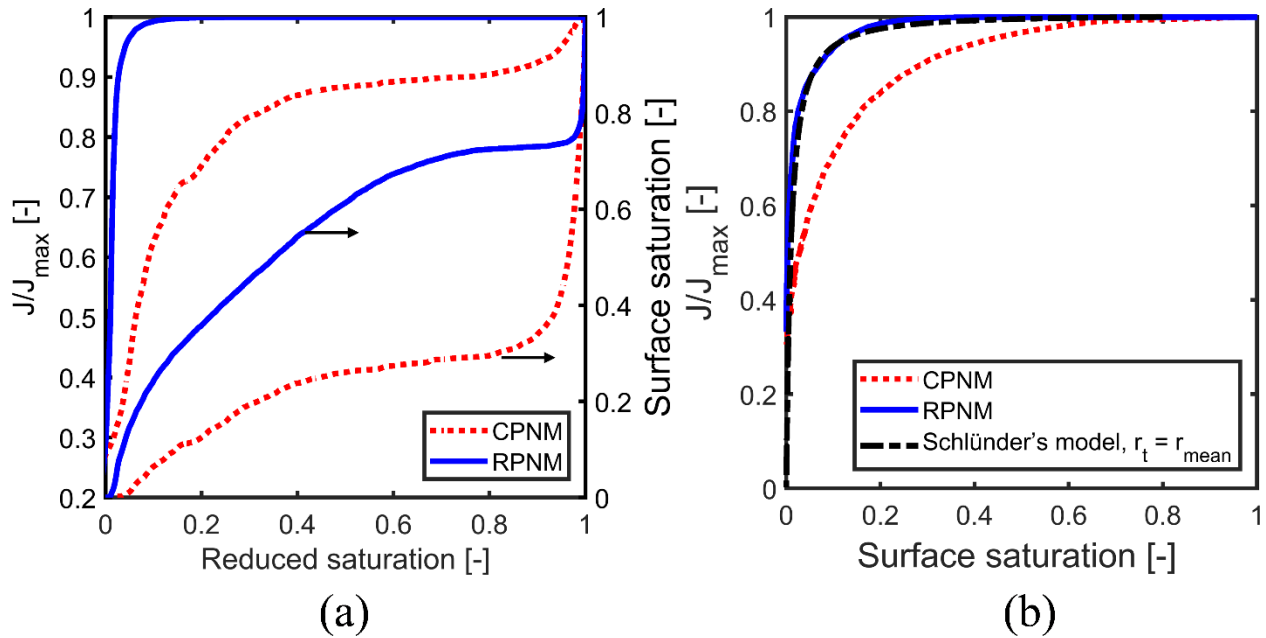


Fig. 6.11. (a) Normalized evaporation rate and surface saturation as a function of reduced network saturation and (b) normalized evaporation rate as a function of surface saturation obtained from the CPNM and RPNM simulations as well as from the solution of Schlünder's model for $r_t = r_{\text{mean}}$.

Figure 6.11 shows CRP and transition of CRP/FRP as a function of reduced saturation and the comparison between Schlünder's model prediction and the CPNM and RPNM simulations. Reduced saturation is calculated as $(S_{\text{net}} - S_{\text{dry}}) / (1 - S_{\text{dry}})$, where S_{net} and S_{dry} are the network saturation and the saturation when the network surface dries, respectively. S_{dry} for CPNM and RPNM is 0.64 and 0.20, respectively. Figure 6.11a displays the portion of Fig. 6.1 which is comparable to Schlünder's model. The results obtained from the CPNM indicate a poor agreement with the Schlünder formula as shown in Fig. 6.11b. The agreement is improved quite significantly with the evaporation rate based on RPNM simulations. According to Schlünder's approach, the evaporation rate from a partially saturated surface remains almost consistent with the initial evaporation rate though the surface saturation decreases, that means, until θ becomes small enough. The inclusion of secondary capillary structure as rings in CPNM explains the significant difference between the CPNM and Schlünder's model. The rings increase

liquid connectivity and reduce the internal moisture transport resistance, promoting the surface wetness. Due to this support, the lateral vapor transfer in the boundary layer ensures that the liquid is evaporated at the initial evaporation rate. For the CPNM, the high internal moisture transport resistance prevents the replenishment of the surface wetness from the bottom of the pore network.

Chapter 7

7 Conclusions and outlook

7.1 Conclusions

In this work, two drying experiments under controlled, fixed conditions have been performed with two dense glass bead packings saturated either with pure liquid water or with a potassium iodide (KI) solution. The three-dimensional microstructures of the liquid and solid phases were determined from X-ray micro computed tomography (μ -CT) images. By means of the images the drying kinetics and slice-averaged saturation profiles of the packing initially saturated with pure water were tracked down to low saturations. Pinning of the evaporation front on the packing surface resulted in a long first drying period with constant drying rates. Earlier studies (Yiotis et al., 2003; 2004) often attributed such an observation to the continuous corner films that develop over an extended region in a drying porous medium. However, in previous study (Vorhauer et al., 2015) conducted with quasi-2D model porous media, produced using microfluidic techniques, and 2D pore network simulations it was found that liquid films do not necessarily form corner films interconnected macroscopically, they rather resemble a network of discrete capillary rings with a much more limited spatial extension. Since most of the previous works conducted on this topic have considered quasi-2D systems, there was an open question about which form of secondary capillary structures can be expected in a real 3D drying porous medium. The experiment with KI solution was

therefore planned with the primary target of elucidating secondary capillary structures in a 3D drying particle packing. The evolution of the liquid phase over time clearly showed the formation of liquid rings inside the glass bead packing moistened with KI solution.

Based on the important insights gained from this experiment, liquid rings were successfully incorporated into a 3D ring pore network model, in which throats as primary capillaries and rings as secondary capillaries approximate collectively the void space between primary particles. In each liquid cluster, liquid rings act as auxiliary hydraulic bridges through which liquid is transported from larger throats to smaller throats. Thus, they significantly extend the pathways for liquid transfer and reduce the resistance for vapor transport from the liquid-gas invasion front to the network surface. Such enhancement in intercluster connectivity led to the development of a film zone in the RPNM that kept the evaporation front pinned on the network surface for longer time. Finally, in order to highlight the role and significance of liquid rings in drying, the simulation results obtained from both PNMs were successfully compared with the X-ray measurements. On this basis, it was found that the drying time and the phase distribution over time can be predicted more realistically if secondary capillary rings are accounted for.

The RPNM was utilized in different hypothetical scenarios to observe versatility and sensitivity of the model. Three sets of ring sizes with two extreme conditions around medium condition were generated. It is found that the decrease in ring size promotes the role of secondary capillary structures which in turn increases the role of non-diffusive gas zone. The smaller ring lengthens the duration of CRP and improves liquid connection marginally. The opposing extreme scenario with increase in ring size (when the rings contains most of total liquid volume) shows dramatic impact on drying kinetics, phase distribution and transport zones. The evaporation of liquid in primary capillaries causes the liquid phase to disintegrate quickly, leading to a short duration of CRP. The role of non-diffusive gas zone shrinks because bigger rings are unable to establish saturated air

conditions in empty primary capillaries. The shrinkage of non-diffusive gas zone generates dramatic rise in dry zone and film zone. The influence of throat size distribution on the liquid connectivity and drying kinetics was investigated. The increase in standard deviation of throat radii lengthens duration of main liquid cluster and CRP increase in both models, but the extent of impact is different due to different late disintegration rate. The influence of boundary layer thickness is slightly more significant in CPNM than RPNM.

The role of discrete capillary rings in mass transfer from the surface of a slowly drying non-hygroscopic porous medium was quantified using classical pore network model and ring pore network model simulations. Results show that capillary rings support liquid transport to the medium surface by establishing saturated air conditions in drained pores even if they are not hydraulically interconnected. The results obtained from these two PNM models are compared against each other and also against that of Schlünder's model. According to the previous studies conducted using CPNMs (Moghaddam et al., 2018; Lu et al., 2021), both types of wet and dry patches at the surface contribute to the evaporation rate from the surface of the porous medium, while Schlünder's model emphasizes the contribution of wet patches and neglects the role of dry patches. The RPNM indicates a dominant role of wet patches and minor role of dry patches at the surface towards the end of constant rate period. The findings of RPNM support relatively better the simple analytical formulation of evaporation rate as a function of extent of wet surface made by Schlünder (1988, 2004).

Moreover, the impact of capillary rings on drying kinetics and phase distribution is extensive. When rings are present, nearly all liquid remains belonging to the main cluster from the beginning till the end of the constant rate period, during which liquid supply from the bottom towards the surface of the network is maintained. Therefore, the average vapor partial pressure at the surface stays near the equilibrium vapor pressure. Another major impact is an apparent decrease in the sharp drop observed in profiles of saturation near the evaporative surface (edge effect) and also removal of the initial transition period

because of the mild drop in the surface saturation and late formation of isolated elements. Moreover, it is observed that consideration of capillary rings in PNMs increases the coordination number of pores which eventually leads to a lower irreducible saturation compared to PNMs that exclude such secondary capillary elements (e.g., see, Moghaddam et al., 2017; Lu et al., 2020).

7.2 Outlook

The results obtained from this study are expected to give a better prediction of experimental observations and to improve our understanding of the relationship between liquid structures, pore-scale effects, and drying kinetics – knowledge of crucial importance. While the focus of this work was laid on the experimental observation and the discrete modeling of liquid rings, viscous effects both in the liquid films and in the bulk liquid clusters should be taken into account to enhance the predictive capacity of such three-dimensional ring PNMs. It would be interesting to also study drying kinetics, solute transport, and formation of solid deposits experimentally and numerically in the presence of secondary capillary structures. Also, an extension of the RPNM to account for internal temperature gradients could be made. Unstructured networks with realistic pore structures in the presence of secondary capillary structures shall be explored. Inclusion of mechanical effects in RPNM will enrich the model to gather spatial and temporal information on damage during drying. Moreover, pore network modeling has recently been used to build continuum models for drying porous media by estimating macroscopic parameters from pore-scale resolved data. The derivation of these continuum models neglects secondary capillary structures for drying porous media. Exploring these physical and structural aspects is left to future research.

The experimental and numerical work presented in this thesis can be extended to investigate the effect of particle roughness and shape on porous media drying. The effect of wettability (contact angle) on evaporation of porous media is also an important research direction. Different contact angles can be observed when liquids with different wetting condition come into contact with the solid surface. In this thesis hydrophilic glass

beads were used in experiment and pore network model simulation assume zero contact angle. Future experimental and numerical studies can be planned with hydrophobic particles and even a mixture of both hydrophilic and hydrophobic particles to study the extent of interruption of connectivity of liquid phase and secondary capillary structures during drying of particle aggregates.

Bibliography

Brakel, J.V.: Mass transfer in convective drying, in: A.S. Mujumdar (Ed.), *Advances in Drying*. Vol. 1, Hemisphere Publishing Inc., New York, 217-267 (1980).

Bear J., Corapcioglu M.Y.: *Advances in transport phenomena in porous media*. Martinus Nijhoff Publishers, Lancaster, 1987.

Börnhorst, M., Walzel, P., Rahimi, A., Kharaghani, A., Tsotsas, E., Nestle, N., Besser, A., Kleine Jäger, F., Metzger, T.: Influence of pore structure and impregnation-drying conditions on the solid distribution in porous support materials, *Dry. Technol.* 34 1964-1978 (2016).

Badetti, M., Fall, A., Chevoir, F., Aïmediou, P., Rodts, S., Roux, J.-N.: Rheology and microstructure of unsaturated granular materials: Experiments and simulations, *J. Rheol.* 62, 1175 -1186 (2018).

Bhaskaran, S., Pandey, D., Panda, D., Paliwal, S., Vorhauer, N., Tsostas, E., Surasani, V.K.: Study of film effects during isothermal drying of square capillary tube using lattice Boltzmann method, *Dry. Technol.* 40, 735-747 (2021).

Chauvet, F., Duru, P., Geoffroy, S., Prat, M.: Three periods of drying of a single square capillary tube. *Phys. Rev. Lett.* 103, 124502 (2009).

Chauvet, F., Duru, P., Prat, M.: Depinning of evaporating liquid films in square capillary tubes: Influence of corners roundness. *Phys. Fluids* 22, 112113 (2010).

Chen, C., Duru, P., Joseph, P., Geoffroy, S., Prat, M.: Control of evaporation by geometry in capillary structures: From confined pillar arrays in a gap radial gradient to phyllotaxy-inspired geometry. *Scient. Reports* 7, 015110 (2017).

Chen, C., Joseph, P., Geoffroy, S., Prat, M., Duru, P.: Evaporation with the formation of chains of liquid bridges. *J. Fluid Mech.* 837, 703-728 (2018).

Dullien, F.A.L., Zarcone, C., MacDonald, I.F., Collins, A., Bochar, R.D.E.: The effects of surface roughness on the capillary pressure curves and the heights of capillary rise in glass bead packs, *J. Colloid Interface Sci.* 127, 362-372 (1989).

Daian, J.F., Saliba, J.: Determining a representative random pore-network for moisture sorption and migration in cement mortar. *Int. J. Heat Mass Transf.* 34, 2081-2096 (1991).

Dillard, L.A., Blunt, M.J.: Development of a pore network simulation model to study nonaqueous phase liquid distribution. *Water Resources Res.* 36 (2), 439-454 (2000).

Derluyn, H., Moonen, P., Carmeliet, J.: Deformation and damage due to drying-induced salt crystallization in porous limestone. *J. Mech. Phys. Solids* 63, 242-255 (2014).

Donkers, P.A.J., Pel, L., Adan, O.C.G.: Dehydration/hydration of granular beds for thermal storage applications: A combined NMR and temperature study. *Int. J. Heat Mass Transf.* 105, 826-830 (2017).

Eloukabi, H., Sghaier, N., Nasrallah, S.B., Prat, M.: Experimental study of the effect of sodium chloride on drying of porous media: The crusty-patchy efflorescence transition, *Int. J. Heat Mass Transf.* 56, 80-93 (2013).

Faure, P., Coussot, P.: Drying of a model soil. *Phys. Rev. E* 82, 036303 (2010).

Geoffroy, S., Prat, M.: A review of drying theory and modelling approaches. Chapter 7, in: J. M. P. Q. Delgado (Ed.), *Drying and Wetting of Building Materials and Components, Building Pathology and Rehabilitation*, Springer, Switzerland, 4, 145-175 (2014).

Gupta, S., Huinink, H., Prat, M., Pel, L., Kopinga, K.: Paradoxical drying due to salt crystallization, *Chem. Eng. Sci.* 109, 204-211 (2014).

Haide, R., Fest-Santini, S., Santini, M.: Use of X-ray micro-computed tomography for the investigation of drying processes in porous media: A review, *Dry. Technol.* doi.10.1080/07373937.2021.1876723 (2021).

Kharaghani, A., Metzger, T., Tsotsas E.: A proposal for discrete modeling of mechanical effects during drying, combining pore networks with DEM. *AIChE J.* 57(4), 872-885 (2011).

Kharaghani, A., Metzger, T., Tsotsas E.: An irregular pore network model for convective drying and resulting damage of particle aggregates. *Chem. Eng. Sci.* 75, 267-278 (2012).

Keita, E., Faure, P., Rodts, S., Coussot, P.: MRI evidence for a receding-front effect in drying porous media. *Phys. Rev. E.* 87, 062303 (2013).

Keita, E., Kodger, T.E., Faure, P.: Water retention against drying with soft-particle suspensions in porous media. *Phys. Rev. E.* 94, 033104 (2016).

Kharaghani, A.: Drying and wetting of capillary porous materials: insights from Imaging and physics-based modeling, Habilitation thesis, Otto-von-Guericke-Universität, Magdeburg (2020).

Kharaghani, A., Mahmood, H.T., Wang, Y.J., Tsotsas, E.: Three-dimensional visualization and modelling of liquid film rings observed during drying of random particle packings. *Int. J. Heat Mass Transf.* 177, 121505 (2021).

Luikov, A.V.: *Heat and Mass Transfer in Capillary-Porous Bodies*, Oxford: Pergamon Press (1966).

Laurindo, J.B., Prat, M.: Numerical and experimental network study of evaporation in capillary porous media: Phase distributions. *Chem. Eng. Sci.* 51, 5171-5185 (1996).

Laurindo, J.B., Prat, M.: Numerical and experimental network study of evaporation in capillary porous media: Drying rates. *Chem. Eng. Sci.* 53, 2257-2269 (1998).

Le Bray, Y., Prat, M.: Three-dimensional pore network simulation of drying in capillary porous media, *Int. J. Heat Mass Transf.* 42, 4207-4224 (1999).

Lehmann, P., Assouline, S., Or, D.: Characteristic lengths affecting evaporative drying of porous media, *Phys. Rev. E - Stat. Nonlinear, Soft Matter Phys.* 77, 056309 (2008).

Lehmann, P., Or, D.: Effect of wetness patchiness on evaporation dynamics from drying porous surfaces, *Water Resour. Res.* 49, 8250-8262 (2013).

Lenormand, R., Touboul, E., Zarcone, C.: Numerical models and experiments on immiscible displacement in porous media. *J. Fluid Mech.* 189, 165-187 (1988).

Lu, X., Kharaghani, A., Tsotsas, E.: Transport parameters of macroscopic continuum model determined from discrete pore network simulations of drying porous media: Throat-node vs. throat-pore configurations. *Chem. Eng. Sci.* 223, 115723 (2020).

Lu X., Kharaghani A., Adloo H., Tsotsas E.: The Brooks and Corey capillary pressure model revisited from pore network simulations of capillarity-controlled invasion percolation process. *Processes*, 8, 1318 (2020).

Lu, X., Tsotsas, E., Kharaghani, A.: Insights into evaporation from the surface of capillary porous media gained by discrete pore network simulations. *Int. J. Heat and Mass Transf.* 168, 120877 (2021).

Lu X., Tsotsas E., Kharaghani A.: Drying of capillary porous media simulated by coupling of continuum-scale and micro-scale models, *Int. J. Multiph. Flow*, 140, 103654 (2021).

Metzger, T., Irawan, A., Tsotsas, E.: Remarks on the paper "Extension of Hoshen-Kopelman algorithm to non-lattice environments" by A. Al-Futaisi and T.W. Patzek, *Physica A* 321 (2003) 665-678, *Phys. A Stat. Mech. Its Appl.* 363, 558-560 (2006).

Metzger, T., Tsotsas, E., Prat, M.: Pore-network models: A powerful tool to study drying at the pore level and understand the influence of structure on drying kinetics. *Modern Drying Technology*, Vol. 1: Computational Tools at Different Scales, Tsotsas, E., Mujumdar, A.S., Eds. Wiley-VCH: Weinheim. 57-102 (2007a).

Metzger, T., Irawan A., Tsotsas E.: Influence of pore structure on drying kinetics: A pore network study, *AIChE J.* 53(12), 3029 -3041 (2007b).

Metzger, T., Tsotsas E.: Network models for capillary porous media: application to drying technology, *Chem. Ing. Tech.* 82(6), 869 - 879 (2010).

Moghaddam, A.A., Kharaghani, A., Tsotsas, E., Prat, M.: Kinematics in a slowly drying porous medium: reconciliation of pore network simulations and continuum modeling. *Phys. Fluids* 29, 022102 (2017).

Moghaddam, A.A., Prat, M., Tsotsas, E., Kharaghani, A.: Evaporation in capillary porous media at the perfect piston-like invasion limit: Evidence of nonlocal equilibrium effects, *Water Resour. Res.* 53, 10433-10449 (2017).

Moghaddam, A.A., Kharaghani, A., Tsotsas, E., Prat, M.: A pore network study of evaporation from the surface of a drying non-hygroscopic porous medium. *AIChE J.* 64 (4), 1435-1447 (2018).

Nowicki, S.C., Davis, H.T., Scriven, L.E.: Microscopic determination of transport parameters in drying porous media. *Dry. Technol.* 10, 926-946 (1992).

Philip, J.R., Vries, D. De.: Moisture movement in porous materials under temperature gradients. *EOS* 38, 222-232 (1957).

Prat, M.: Percolation model of drying under isothermal conditions in porous media. *Int. J. Multiph. Flow*, 19, 691-704 (1993).

Prat, M.: Recent advances in pore-scale models for drying of porous media, *Chem. Eng. J.* 86, 153-164 (2002).

Pel, L., Huinink, H., Kopinga, K.: Ion transport and crystallization in inorganic building materials as studied by nuclear magnetic resonance. *Appl. Phys. Lett.* 81, 2893 (2002).

Prat, M.: On the influence of pore shape, contact angle and film flows on drying of capillary porous media, *Int. J. Heat Mass Transf.* 50, 1455-1468 (2007).

Prat, M.: Pore network models of drying, contact angle, and film flows, *Chem. Eng. Technol.* 34, 1029-1038 (2011).

Panda, D., Supriya, B., Kharaghani, A., Tsotsas, E., Surasani, V.K.: Lattice Boltzmann simulations for micro-macro interactions during isothermal drying of bundle of capillaries, *Chem. Eng. Sci.* 220, 115634 (2020).

Pham, S.T.: DEM-based triangulation pore network model for particle aggregates: Drying and capillary forces, PhD thesis, Otto-von-Guericke-Universität, Magdeburg (2021).

Rodriguez-Navarro, C., Doehne, E.: Salt weathering: Influence of evaporation rate, supersaturation and crystallisation pattern, *Earth Surf. Process. Landf.* 24, 191-209 (1999).

Rad, M.N., Shokri, N., Sahimi, M.: Pore-scale dynamics of salt precipitation in drying porous media, *Phys. Rev. E - Stat. Nonlinear, Soft Matter Phys.* 88, 032404 (2013).

Stewart, W.E.: Heat and mass transfer in capillary-porous bodies, *AIChE J.* 13, 618-620 (1967).

Sahimi, M., Hughes, B.D., Scriven, L.E., Ted Davis, H.D: Dispersion in flow through porous media, Part 1: One-phase flow. *Chem. Eng. Sci.* 41, 2103-2122 (1986).

Schlünder, E.U.: On the mechanism of the constant drying rate period and its relevance to diffusion controlled catalytic gas phase reactions. *Chem. Eng. Sci.* 43, 2685-2688 (1988).

Schlünder, E.U.: Drying of porous material during the constant and the falling rate period: A critical review of existing hypotheses. *Dry. Technol.* 22, 1517-1532 (2004).

Segura, L.A., Toledo, P.G.: Pore-level modeling of isothermal drying of pore networks, *Chem. Eng. J.* 111, 2007-2019 (2005).

Surasani, V.K., Metzger, T., Tsotsas E.: Consideration of heat transfer in pore network modelling of convective drying. *Int. J. Heat Mass Transf.* 51, 2506-2518 (2008).

Su, B., Sanchez, C., Yang, X.Y.: Hierarchically structured porous Materials: From nanoscience to catalysis, separation, optics, energy, and life science. *JWS.* (2011).

Scheel, M., Seemann, R., Brinkmann, M., Di Michiel, M., Sheppard, A., Herminghaus, S.: Liquid distribution and cohesion in wet granular assemblies beyond the capillary bridge regime, *J. Phys. Condens. Matter* 20, 494236 (2008).

Shokri, N., Lehmann, P., Or, D.: Liquid-phase continuity and solute concentration dynamics during evaporation from porous media: Pore-scale processes near vaporization surface, *Phys. Rev. E - Stat. Nonlinear, Soft Matter Phys.* 81, 046308 (2010).

Shokri, N., Or, D.: What determines drying rates at the onset of diffusion controlled stage-2 evaporation from porous media?, *Water Resour. Res.* 47, 09513 (2011).

Sahimi, M.: Models of fractures and fractured porous media, in: *Flow and Transport in Porous Media and Fractured Rock*, Wiley-VCH, Weinheim, 213-251 (2011).

Semprebon, C., Scheel, M., Herminghaus, S., Seemann, R., Brinkmann, M.: Liquid morphologies and capillary forces between three spherical beads, *Physical Review E* 94, 012907 (2016).

Shokri-Kuehni, S.M.S., Rad, M.N., Webb, C., Shokri, N.: Impact of type of salt and ambient conditions on saline water evaporation from porous media, *Adv. Water Resour.* 105, 154-161(2017).

Talbi, M., Prat, M.: About Schlünder's model: A numerical study of evaporation from partially wet surfaces. *Dry. Technol.* 37, 513-524 (2019).

Voronoi, G.: Nouvelles applications des paramètres continus à la théorie des formes quadratiques, *Journal für die Reine und Angewandte Mathematik*. 133, 97-198 (1908).

Vorhauer, N., Wang, Y.J., Kharaghani, A., Tsotsas, E., Prat, M.: Drying with formation of capillary rings in a model porous medium. *Transport Porous Med.* 110, 197-223 (2015).

Wilkinson, D., Willemsen, J.F.: Invasion percolation: A new form of percolation theory. *J. Phys. A* 16, 3365-3376 (1983).

Whitaker S.: Coupled transport in multiphase systems: A theory of drying. *Adv. Heat Transf.* 31, 1-104 (1998).

Winterberg, M., Tsotsas, E.: Impact of tube-to-particle-diameter ratio on pressure drop in packed beds, *AIChE J* 46, 1084-1088 (2000).

Wang, Y.J., Kharaghani, A., Metzger, T., Tsotsas, E.: Pore network drying model for particle aggregates: Assessment by X-Ray microtomography, *Dry. Technol.* 30, 1800-1809 (2012a).

Wang, Y.J., Kharaghani, A., Tsotsas, E.: Pore-scale comparison of liquid distributions between pore network drying simulations and X-ray tomography. In: *Proceedings of the 18th International Drying Symposium (IDS 2012)*, Xiamen, China, 11-15 Nov. (2012b).

Wang, Y.J., Kharaghani, A., Tsotsas, E.: Pore-scale visualization and simulation of liquid films for drying particle packing, *Proceedings of Eurodrying'2013*, Paris, France, 2-4 Oct. (2013)

Wang, Y.J., Mahmood, H.T., Kharaghani, A., Tsotsas, E.: Visualization and modeling of liquid film rings observed during drying of particle packings. In: *Proceedings of the 19th International Drying Symposium (IDS 2014)*, Lyon, France, 24-27 Aug (2014).

Wu, R., Kharaghani, A., Tsotsas, E.: Capillary valve effect during slow drying of porous media, *Int. J. Heat and Mass Transf.* 94, 81-86 (2016).

Wu, R., Zhao, C.Y., Tsotsas, E., Kharaghani, A.: Convective drying in thin hydrophobic porous media, *Int. J. Heat and Mass Transf.* 112, 630-642 (2017).

Wu, R., Zhang, T., Ye, C. Zhao, C.y., Tsotsas, E., Kharaghani, A.: Pore network model of evaporation in porous media with continuous and discontinuous corner films, *Phys. Rev. Fluids* 5, 014307 (2020).

Yiotis, A.G., Stubos, A.K., Boudouvis, A.G., Yortsos, Y.C.: A 2-D pore-network model of the drying of single-component liquids in porous media. *Adv. Water Resour.* 24, 439-460 (2001).

Yiotis, A.G., Boudouvis, A.G., Stubos, A.K., Tsimpanogiannis, I.N., Yortsos, Y.C.: Effect of liquid films on the isothermal drying of porous media. *Phys. Rev. E* 68, 037303 (2003).

Yiotis, A.G., Boudouvis, A.G., Stubos, A.K., Tsimpanogiannis, I.N., Yortsos, Y.C.: Effect of liquid films on the drying of porous media. *AIChE J.* 50, 2721-2737 (2004).

Yiotis, A.G., Tsimpanogiannis, I.N., Stubos, A.K., Yortsos, Y.C.: Pore-network study of the characteristic periods in the drying of porous materials. *J. Colloid Interface Sci.* 297, 738-748 (2006).

Yiotis, A.G., Tsimpanogiannis, I.N., Stubos, A.K., Yortsos, Y.C.: Coupling between external and internal mass transfer during drying of a porous medium. *Water Resour. Res.* 43, W06403 (2007).

Yiotis, A.G., Salin, D., Yortsos, Y.C.: Drying in porous media with gravity-stabilized fronts: Experimental results. *Phys. Rev. E* 86(2), 026310 (2012).

Student work

The following MSc. thesis has been conducted within the framework of this PhD thesis:

1. Parth Patel, Parametric study of transport phenomena in drying of porous media by ring pore network model simulation, Chair of Thermal Process Engineering, Otto-von-Guericke-Universität Magdeburg, February 2021.

Publications list

Own publications and presentations related to this thesis in national and international journals and conferences are listed in the following.

Journal publications

- 1) Abdolreza Kharaghani, Hafiz Tariq Mahmood, Yujing Wang, Evangelos Tsotsas, Three-dimensional visualization and modeling of capillary liquid rings observed during drying of dense particle packings. *International Journal of Heat and Mass Transfer*, 177, 121505 (2021).
- 2) Hafiz Tariq Mahmood, Evangelos Tsotsas, Abdolreza Kharaghani, The role of discrete capillary rings in mass transfer from the surface of a drying capillary porous medium. *Transport in Porous Media*, 140, 351-369 (2021).

Peer-reviewed Proceedings

- 1) Hafiz Tariq Mahmood, Xiang Lu, Evangelos Tsotsas, Abdolreza Kharaghani, The role of discrete capillary rings in mass transfer from the surface of a capillary porous medium during drying, 7th European Drying Conference, July 10-12, 2019, Politecnico di Torino, Italy.
- 2) Hafiz Tariq Mahmood, Evangelos Tsotsas, Abdolreza Kharaghani, 3D pore network simulations of mass transfer from the surface of drying porous media, 22nd International Drying Symposium, June 26-29, 2022, Worcester, Massachusetts, USA, DOI: <http://dx.doi.org/10.4995/ids2018.2018.7388>.

Poster presentation

- 1) Hafiz Tariq Mahmood, Evangelos Tsotsas, Abdolreza Kharaghani, The impact of capillary rings on mass transfer from the surface of drying porous media investigated by 3D pore network models, Jahrestreffen der ProcessNet-Fachgruppen Hochdruckverfahrenstechnik und Trocknungstechnik zusammen mit dem Jahrestreffen der ProcessNet- Fachgruppe Phytoextrakte, March 15-16, 2021, Germany (Online Event).

Oral presentation

- 1) Hafiz Tariq Mahmood, Evangelos Tsotsas, Abdolreza Kharaghani, The role of liquid films in drying capillary porous media investigated by 3 D pore network models, European Federation of Chemical Engineering Drying research: focus on freeze-drying, lyophilization, spray-drying and product quality, May 17-21, 2021 (Webinar).